

AD-A049 766

PENNSYLVANIA STATE UNIV UNIVERSITY PARK APPLIED RESE--ETC F/6 20/4
SCALING OF CAVITATION DAMAGE.(U)

FEB 77 D R STINEBRING

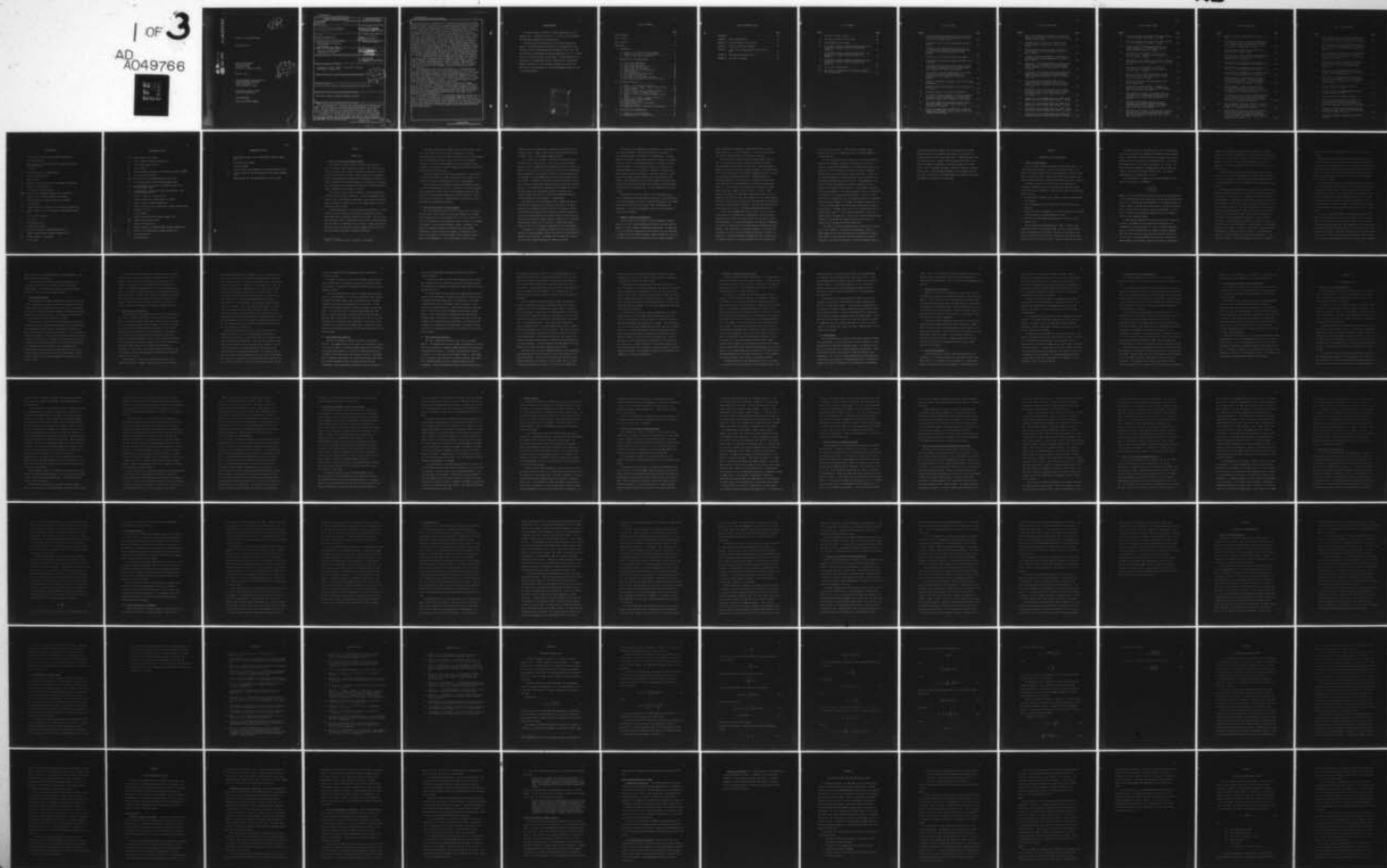
N00017-73-C-1418

UNCLASSIFIED

TM-76-51

NL

1 OF 3
AD
A049766



AD NO. 12
DDC FILE COPY

AD A 049766

SCALING OF CAVITATION DAMAGE

Stinebring, D. R.

Technical Memorandum
File No. TM 76-51
17 February 1977
Contract No. N00017-73-C-1418

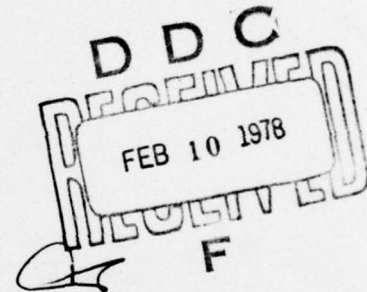
Copy No. 6

The Pennsylvania State University
APPLIED RESEARCH LABORATORY
Post Office Box 30
State College, PA 16801

Approved for Public Release
Unlimited Distribution

NAVY DEPARTMENT

NAVAL SEA SYSTEMS COMMAND



UNCLASSIFIED

SECURITY CLASSIFICATION OF THIS PAGE (When Data Entered)

REPORT DOCUMENTATION PAGE		READ INSTRUCTIONS BEFORE COMPLETING FORM
1. REPORT NUMBER (14) TM-76-51	2. GOVT ACCESSION NO.	3. RECIPIENT'S CATALOG NUMBER
4. TITLE (and Subtitle) (6) Scaling of Cavitation Damage	5. TYPE OF REPORT & PERIOD COVERED (9) Technical Memo	
7. AUTHOR(s) (10) David R. Stinebring	8. CONTRACT OR GRANT NUMBER(s) (15) N00017-73-C-1418	
9. PERFORMING ORGANIZATION NAME AND ADDRESS PA State Univ ✓ Applied Research Laboratory P.O. Box 30 State College, PA 16801	10. PROGRAM ELEMENT, PROJECT, TASK AREA & WORK UNIT NUMBERS	
11. CONTROLLING OFFICE NAME AND ADDRESS Naval Sea Systems Command Washington, DC 20362	12. REPORT DATE (11) 17 Feb 1977	
14. MONITORING AGENCY NAME & ADDRESS (if different from Controlling Office)	13. NUMBER OF PAGES (12) 180 P.	
	15. SECURITY CLASS. (of this report) UNCLASSIFIED	
15a. DECLASSIFICATION/DOWNGRADING SCHEDULE		
16. DISTRIBUTION STATEMENT (of this Report) Approved for public release. Distribution unlimited. Per NAVSEA - 24 March 1976		
17. DISTRIBUTION STATEMENT (of the abstract entered in Block 20, if different from Report)		
18. SUPPLEMENTARY NOTES Master of Science Thesis in Aerospace Engineering, August 1976.		
19. KEY WORDS (Continue on reverse side if necessary and identify by block number) cavitation, erosion, cavitation damage, corrosion		
20. ABSTRACT (Continue on reverse side if necessary and identify by block number) This investigation has focused on the initial stages of cavitation erosion using a ductile material in a flowing system employing water as the working fluid. The test models were 0.635 cm diameter zero-caliber ogives made of pure annealed aluminum. The aluminum was selected as a material which would be suitable for recording the intensity of cavitation bubble collapse. The damage in the initial stages was in the form of small indentations in the model surface. The greatest damage was within an area corresponding to the cavity closure point on the model. The pits were round depressions		

DDC
RECEIVED
FEB 10 1978
F

DD FORM 1 JAN 73 1473 EDITION OF 1 NOV 65 IS OBSOLETE

UNCLASSIFIED

SECURITY CLASSIFICATION OF THIS PAGE (When Data Entered)

391 007

50B

UNCLASSIFIED

SECURITY CLASSIFICATION OF THIS PAGE (When Data Entered)

usually under 0.1 mm in diameter with the majority less than 0.05 mm across. During the formation of these pits, it appears that no material was removed from the surface. Using the pure annealed aluminum test probe, a sufficient damage sample could be generated in a relatively short period of time.

It was observed that the velocity had a marked effect upon the rate of damage production. For a range of velocities from 14.9 to 59.3 m/sec, the damage and pitting rates increased by approximately the sixth power of velocity. This result is in agreement with the observations of R. T. Knapp which were first reported in 1955. The velocity also affected the sizes of the individual damage pits. The average volume of the pits increased by the fifth power of velocity. Since the volume of each pit is a measure of the energy required to form the pit, the average collapse energy absorbed increases by the fifth power of velocity. A relationship between the pit volume and the absorbed collapse energy was obtained by performing a dynamic hardness test on the model material. If the pitting rate increases by the sixth power of velocity, and the average collapse energy absorbed per pit increases by the fifth power, then the rate of total damage energy absorbed by the model increases by the eleventh power. A plot of the distribution of absorbed collapse energies was also generated for three flow conditions.

It was observed that the cavity length and air content also affected the damage rates. There was almost no damage to the models for very short cavity lengths. The damage rate increased with cavity length, reached a peak, and then slowly decreased for longer cavities. This tendency has been observed by other investigators. For a doubling of the air content from 10 to 20 ppm, the rate of damage production was reduced by nearly fifty percent.

From high-speed movies of the cavity behavior, it was observed that the cavity regularly breaks off from the model surface. This is due to a reentrant jet moving through the cavity and striking the cavity leading edge. On many of the models, pitting was observed near the leading edge. It is felt that this could be a result of the reentrant jet behavior. When the jet strikes the cavity wall, it creates a short-term pressure rise, causing local cavitation bubbles to collapse. If the collapsing bubbles are near the model surface, damage to the model could occur.

The effect of cavitation upon the rate of corrosion of aluminum was not fully explored. General observations showed a strong relationship between the cavitation and corrosion, with cavitation tending to increase the corrosion rate. For observations of the corrosion damage and cavitation pitting, the scanning electron microscope proved to be a most useful tool. Clear views of the damage were obtained with the large depth of field possible at high magnifications.

In general, the results of this investigation compared favorably with the results of other investigations. The sixth power damage rate law and the actual damage rates involved showed good agreement with three other investigations. The interesting feature of this comparison is the fact that even though the size and shape of the models used in each of the four investigations were significantly different, the observed damage rates were approximately equal at the same velocity.

UNCLASSIFIED

SECURITY CLASSIFICATION OF THIS PAGE (When Data Entered)

ACKNOWLEDGMENTS

The author wishes to express his deepest appreciation to his advisors, Drs. J. William Holl and R. E. A. Arndt, for their guidance and counseling throughout this investigation.

The investigation was conducted at the Garfield Thomas Water Tunnel of the Applied Research Laboratory at The Pennsylvania State University under the sponsorship of E/F Research Project 6114. The author wishes to acknowledge the helpful suggestions of Dr. M. T. Pigott who was the technical monitor of this grant. Further appreciation is expressed to Dr. Eugene White and Mr. Phillip Swab of the Materials Research Laboratory, to the entire Water Tunnel Staff, and to the many others who contributed their time and knowledge during the course of this investigation.

ACCESSION for	
NTIS	White Section <input checked="" type="checkbox"/>
DDC	Buff Section <input type="checkbox"/>
UNANNOUNCED	<input type="checkbox"/>
JUSTIFICATION	
BY	
DISTRIBUTION/AVAILABILITY CODES	
Dist.	SPECIAL
A	

TABLE OF CONTENTS

	<u>Page</u>
Acknowledgments	ii
List of Tables	v
List of Figures	vi
Nomenclature	xi
I. INTRODUCTION	1
1.1 Nature of the Cavitation Damage Problem	1
1.2 Objectives and Scope of the Investigation	2
1.3 Summary of Previous Investigations	4
II. DESCRIPTION OF THE INVESTIGATION	8
2.1 Plan of the Investigation	8
2.2 Water Tunnel Facilities	12
2.3 Model Design and Construction	13
2.4 Water Tunnel Test Procedures	15
2.5 Damage Analysis with the Microscope	18
2.6 Photomicrography	19
2.7 The Scanning Electron Microscope	20
2.8 Pit Volume Determinations	20
2.9 Determination of the Dynamic Hardness	22
2.10 High Speed Photography of Cavity Oscillations	23
III. DISCUSSION OF RESULTS	24
3.1 Phase I - 30.5 cm Water Tunnel Tests	24
3.2 Classification of Damage - Phase II and III Tests	28
3.3 Dynamic Hardness	30
3.4 Effect of Cavity Length on Damage Production	31
3.5 Effect of Velocity on Damage Production	33
3.6 Effect of Velocity on Cavitation Bubble Collapse Energy	34
3.7 Effect of Air Content on Damage Production	36
3.8 Observations of Cavity Dynamics	38
3.9 Leading Edge Pitting	40
3.10 General Observations of the Damage	40
3.11 Corrosion Effects	43
3.12 Comparison of Results with Other Investigations	47
IV. CONCLUSIONS AND RECOMMENDATIONS	51
4.1 Summary of this Investigation	51
4.2 Recommendations for Further Study	53

TABLE OF CONTENTS (CONT.)

	<u>Page</u>
REFERENCES	55
APPENDIX A: Dynamic Hardness Test	58
APPENDIX B: The Scanning Electron Microscope	65
APPENDIX C: Proposed Mechanisms of Damage	68
APPENDIX D: Calculation of Damage Rate for High Velocity Tests	75
APPENDIX E: High Speed Photographic System	79
APPENDIX F: Corrosion of Aluminum	83

LIST OF TABLES

<u>Table</u>		<u>Page</u>
I	Test Data for Phase I Tests	85
II	Test Data for Phase II and III Tests	86
III	Dynamic Hardness Test Results	88
IV	Pit Diameters, Depths, Diameter-to-Depth Ratios, and Volumes for a Velocity of 30.1 m/sec and $L/D=3$ (Model 38)	90
V	Pit Diameters, Depths, Diameter-to-Depth Ratios, and Volumes for a Velocity of 38 m/sec and $L/D=3$ (Model 37)	92
VI	Pit Diameters, Depths, Diameter-to-Depth Ratios, and Volumes for a Velocity of 49.3 m/sec and $L/D=3$ (Model 41)	94
VII	Cavity Cycle Frequency Data	96
VIII	Test Data for Investigations of Cavitation Damage in the Incubation Zone	97

LIST OF FIGURES

<u>Figure</u>		<u>Page</u>
1	Cavitation Number Versus Dimensionless Cavity Length for a 0.635 cm Diameter Zero-Caliber Ogive in a 3.8 cm Test Section (Weir, 1975)	100
2	Photograph of the 3.8 cm Ultra-High-Speed Cavitation Tunnel	101
3	Photograph of the Plexiglass Test Section for the 3.8 cm Cavitation Tunnel with the Photographic Test Box Used for High Speed Photography of Cavity Dynamics	102
4	Description of the Cavitation Damage Test Models	103
5	Photograph of the Cavitation Damage Test Models Prior to Testing	104
6	Description of the Area of Damage Analysis for Phase I Test Models (Damage Analysis for a Dimensionless Cavity Length of 2.0 Used as an Example)	105
7	Description of the Area of Damage Analysis for Phase II and III Test Models (Damage Analysis for a Dimensionless Cavity Length of 2.0 Used as an Example)	106
8	Schematic Arrangement of Apparatus Used for Pit Volume Measurements	107
9	Definition Sketch and Equations for the Calculation of Pit Volumes	108
10	Schematic Diagram of the Dynamic Hardness Test	109
11	Photograph of Indenter Rebound for a Dynamic Hardness Test (0.2 m Initial Drop Height, 1 mm Divisions on Right Side of Rule, Zero of Scale at 30 cm of Rule)	110
12	Plot of the Damage Rate Distribution Along a Phase I Test Model (Model 1, $V_{\infty}=21.3$ m/sec, $L/D=2$, and 30-Minute Test Duration)	111
13	Plot of the Damage Rate Distribution in the Maximum Damage Zone Along Model 1 ($V_{\infty}=21.3$ m/sec, $L/D=2$, and 30-Minute Test Duration)	112

LIST OF FIGURES (CONT.)

<u>Figure</u>		<u>Page</u>
14	Plot of the Damage Rate Distribution in the Maximum Damage Zone Along Model 5 ($V_{\infty}=21.3$ m/sec, $L/D=2$, and 15-Minute Test Duration)	113
15	Photomicrograph of a Large Pit in Which Material Has Been Removed from the Surface (Phase I Test Model)	114
16	Photomicrographs Showing the Effect of Velocity on the Deformation of the Leading Edge Contour for Phase I Models	115
17	Schematic Diagram of the Method for Calculation of the Extent of the Maximum Damage Zone for Phase II and III Models	116
18	Damage Rate in the Maximum Damage Zone (DRMD) Versus Dimensionless Cavity Length and Cavitation Number (Phase III Models, $V_{\infty}=38$ m/sec, and an Air Content of 10 ppm)	117
19	Pitting Rate in the Maximum Damage Zone (PRMD) Versus Dimensionless Cavity Length and Cavitation Number (Phase III Models, $V_{\infty}=38$ m/sec, and an Air Content of 10 ppm)	118
20	Total Pitting Rate on the Model (TPR) Versus Dimensionless Cavity Length and Cavitation Number (Phase III Models, $V_{\infty}=38$ m/sec, and an Air Content of 10 ppm)	119
21	Photograph of Cavity Collapse Away from the Model Surface for a Short Cavity Length (0.635 cm Diameter Zero-Caliber Ogive, 3 μ sec Flash Duration, and $V_{\infty}\approx 23$ m/sec)	120
22	Damage Rate in the Maximum Damage Zone (DRMD) Versus Velocity for Phase III Models (Air Content - 10 ppm) . .	121
23	Damage Rate in the Maximum Damage Zone (DRMD) Versus Velocity for Phase II Models (Air Content - 20 ppm) . .	122
24	Pitting Rate in the Maximum Damage Zone (PRMD) Versus Velocity for Phase III Models (Air Content - 10 ppm) . .	123
25	Pitting Rate in the Maximum Damage Zone (PRMD) Versus Velocity for Phase II Models (Air Content - 20 ppm) . .	124

LIST OF FIGURES (CONT.)

<u>Figure</u>		<u>Page</u>
26	Total Pitting Rate on the Model (TPR) Versus Velocity for Phase III Models (Air Content - 10 ppm)	125
27	Total Pitting Rate on the Model (TPR) Versus Velocity for Phase II Models (Air Content - 20 ppm)	126
28	Average Pit Volume (Average Energy Per Pit re A Dynamic Hardness of 0.5 J/mm^3) Versus Velocity (L/D=3 and an Air Content of 10 ppm)	127
29	Distribution of Pit Volumes for a Velocity of 30.1 m/sec and a Dimensionless Cavity Length of 3.0 (Air Content - 10 ppm)	128
30	Distribution of Pit Volumes for a Velocity of 38 m/sec and a Dimensionless Cavity Length of 3.0 (Air Content - 10 ppm)	129
31	Distribution of Pit Volumes for a Velocity of 49.3 m/sec and a Dimensionless Cavity Length of 3.0 (Air Content - 10 ppm)	130
32	Energy Probability Density Distribution for Test Velocities of 30.1, 38.0, and 49.3 m/sec (L/D=3 and an Air Content of 10 ppm)	131
33	Effect of Air Content on the Damage Rate in the Maximum Damage Zone	132
34	Photograph of a Developed Cavity in Water as it Appears to the Eye (0.635 cm Diameter Zero-Caliber Ogive, $V_\infty=19.5 \text{ m/sec}$, and L/D=5)	133
35	High Speed Movie Sequence of a Complete Cycle of a Developed Cavity - 5000 Frames Per Second (0.635 cm Diameter Zero-Caliber Ogive, $V_\infty=25 \text{ m/sec}$, and L/D=2.5)	134
36	High Speed Movie Segments Showing the Vortex Filaments Connecting the Sections of the Cavity After Breakoff (0.635 cm Diameter Zero-Caliber Ogive, $V_\infty=25 \text{ m/sec}$, and L/D=2.5)	135
37	High Speed Movie Sequence of the Reentrant Jet Moving Through the Cavity and Striking the Cavity Leading Edge (0.635 cm Diameter Zero-Caliber Ogive, $V_\infty=15 \text{ m/sec}$, and L/D=4)	136

LIST OF FIGURES (CONT.)

<u>Figure</u>		<u>Page</u>
38	Cavity Cycle Strouhal Number Versus Cavitation Number	137
39	Photograph of the Area of Cavitation Damage Attack on a Test Model (0.635 cm Diameter Zero-Caliber Ogive, Model 46, $V_{\infty}=50$ m/sec, $L/D=4$, Air Content - 8.5 ppm, and a 53-Second Test Duration)	138
40	Photomicrographs of Model Surfaces Before and After Cavitation Damage Testing	139
41	Photomicrograph of the Approximate Pitting Density that Provides a Sufficient Sample for Analysis Without the Pits Overlapping	140
42	Distribution of Pit Diameters for a Velocity of 30.1 m/sec and a Dimensionless Cavity Length of 3.0	141
43	Distribution of Pit Diameters for a Velocity of 38 m/sec and a Dimensionless Cavity Length of 3.0	142
44	Distribution of Pit Diameters for a Velocity of 49.3 m/sec and a Dimensionless Cavity Length of 3.0	143
45	SEM Micrograph of a Deep Indentation Caused by Cavitation and the Machine Tool Marks Showing No Material Removal from the Surface (Model 46, $V_{\infty}=50$ m/sec, $L/D=4$, Air Content - 8.5 ppm)	144
46	SEM Micrographs of a Deep Cavitation Pit and Possible Strain Cracking at the Bottom of the Pit (Model 43, $V_{\infty}=43.4$ m/sec, $L/D=4$, Air Content - 9.84 ppm, and a 1.5-Minute Test Duration)	145
47	Photograph of an Overall View of Spotting Corrosion of a Test Model (0.635 cm Diameter Zero-Caliber Ogive, Model 20, $V_{\infty}=23$ m/sec, $L/D=3$, Air Content - 20 ppm, and a 60-Minute Test Duration)	146
48	Photomicrograph of Spotting Corrosion of a Test Model (Model 20, $V_{\infty}=23$ m/sec, $L/D=3$, Air Content - 20 ppm, and a 60-Minute Test Duration)	147
49	SEM Micrograph of Spotting Corrosion Showing the Deep Irregular Shaped Pit and the Corrosion Products Cemented to the Model Surface (Model 20, $V_{\infty}=23$ m/sec, $L/D=3$, Air Content - 20 ppm, and a 60-Minute Test Duration)	148

LIST OF FIGURES (CONT.)

<u>Figure</u>		<u>Page</u>
50	Photomicrograph of Corrosion Pits Illuminated with Polarized Light (Model 45, $V_{\infty}=30.5$ m/sec, $L/D=4$, Air Content 8.4 ppm, and a 20-Minute Test Duration) . .	149
51	SEM Micrograph of the Corrosion Attack Along the Cubic Structure of Aluminum (Model 37, $V_{\infty}=38$ m/sec, $L/D=3$, Air Content - 9.5 ppm, and a 6-Minute Test Duration)	150
52	SEM Micrographs of a Large Corrosion Pit and Detail of the Layer Deposited About the Pit (Model 34, $V_{\infty}=23$ m/sec, $L/D=2$, Air Content - 7.63 ppm, and a 30-Minute Test Duration)	151
53	SEM Micrograph of Corrosion Damage at the Cavity Reference Mark (Model 46, $V_{\infty}=50$ m/sec, $L/D=4$, Air Content - 8.5 ppm, and a 53-Second Test Duration)	152
54	Damage Rate in the Maximum Damage Zone Versus Velocity for Investigations of Cavitation Damage in Which There is No Weight Loss	153
55	Damage Rate in the Maximum Damage Zone Versus Velocity for Investigations of Cavitation Damage in Which There is No Weight Loss - Corrected for Air Content	154
56	Rate of "Volume Loss" Per Unit Area Versus Velocity (Sato et al., 1973)	155
57	Schematic Diagram of Imaging Mechanisms of the Scanning Electron Microscope	156
58	Proposed Mechanical Mechanisms of Damage	157
59	Tunnel Velocity as a Function of Time for the Velocity Transition Period - with Sample Calculations for the Correction of the Pitting Density for High Velocity Tests (59.3 m/sec Test) . . .	158
60	Photograph of High Speed Photographic Apparatus - Redlake Hycam Camera and EG & G High Speed Strobe Unit (Circular Reflector Shown)	159
61	Schematic Arrangement of High Speed Photographic Apparatus	160

NOMENCLATURE

a	radius of a pit formed during a dynamic hardness test
A	camera lens aperture
c	constant used in the calculation of the guide factor for the high speed camera
C	a constant
CPS	strobe lamp output in candela-seconds
d	depth of a cavitation pit
D	model diameter
D_H	diameter of the pit formed during the dynamic hardness test
D_P	diameter of cavitation pit
D_S	strobe lamp to subject distance
DRMD	damage rate in the maximum damage zone (pits/cm ² /sec)
E_1	energy of fall of dynamic hardness test indenter
E_2	energy of rebound of dynamic hardness test indenter
E_E	elastic energy
E_I	Young's Modulus of the indenter for the dynamic hardness test
E_M	Young's Modulus of the test material for the dynamic hardness test
f	cavity cycling frequency
F	total force
F_I	instantaneous force
g	gravitational constant
h_1	indenter drop height in dynamic hardness test
h_2	indenter rebound height in dynamic hardness test
H_D	dynamic hardness - (Joules/mm ³)
L	cavity length

NOMENCLATURE (CONT.)

L/D	dimensionless cavity length
m	mass of indenter in dynamic hardness test
M	strobe light reflector factor
P _C	cavity pressure
P _D	dynamic hardness expressed as a mean dynamic pressure, (kg/mm ²)
P _∞	free stream static pressure
PRMD	pitting rate in the maximum damage zone (pits/sec)
P _T	total pitting density (from estimated damage rates)
P _{TR}	pitting density for the velocity transition period (from estimated damage rates)
P _{SS}	pitting density for the steady state velocity period (from estimated damage rates)
r	radius of curvature of cavitation pit
r _b	radial distance from a bubble center of collapse
r ₁	indenter radius in dynamic hardness test
r ₂	radius of curvature of pit formed after a dynamic hardness test
s	speed (ASA) of film
S	Strouhal number
t	time of collision during a dynamic hardness test
TPR	total pitting rate (pits/sec)
V	volume of cavitation pit
V _A	apparent volume of pit formed during a dynamic hardness test
V _P	volume of pit formed during a dynamic hardness test
V _∞	free stream velocity
z	vertical distance

NOMENCLATURE (CONT.)

α	instantaneous radius of pit formed during a dynamic hardness test
ρ_L	mass density of a liquid
σ	cavitation number
σ_I	Poisson's ratio of the indenter for the dynamic hardness test
σ_M	Poisson's ratio for the test material for the dynamic hardness test
ϕ	lighting angle for the determination of the pit volumes

CHAPTER I

INTRODUCTION

1.1 Nature of the Cavitation Damage Problem

The destructive action caused by cavitation has long been a practical problem. This problem first became of major concern at the turn of the century with efforts to improve the performance of marine propellers and hydraulic turbines. Severe erosion of the propellers on the liners Lusitania and Mauretania (1)* prompted the creation of a special commission by the British Admiralty to investigate the problem. It was determined that the damage was the result of repeated "hydraulic blows" accompanying the collapse of cavities.

Since the turn of the century, studies of cavitation damage have not been confined to ship's propellers. Ship hull appendages, diesel cylinder liners, pump impellers, hydrofoils, valves and even the sluice gates on hydroelectric power dams are a few examples where cavitation erosion has been a problem.

Accurate prediction of cavitation damage is very difficult. After nearly 100 years of research in cavitation, the problem of scaling model damage data to prototype conditions is unsolved. It is not that there has been a lack of study in this area, for the literature dealing with this subject is voluminous to say the least. Rather, the lack of success is due to the fact that cavitation damage involves both fluid and solid mechanics and thus is inherently difficult.

* Numbers in parenthesis refer to documents in references.

The attack caused by the collapse of one cavitation bubble occurs over a very small area (on the order of hundredths of a square millimeter) and in a very short time interval (measured in microseconds). Both the hydrodynamic aspects of the cavity flow and the material response to the impact loading caused by the cavity collapse must be considered. The problem is further complicated by possible interactions between cavitation and corrosion.

Cavitation damage is influenced by many variables. Flow velocity, cavitation index, model size, model shape, and the air content of the liquid all may affect the damage production to varying degrees.

This investigation was intended to study the hydrodynamic aspects of cavitation damage and the effect of alteration of the flow parameters upon the damage to a model. Many cavitation damage studies have been conducted in nonflow systems employing a vibratory apparatus. However, this study was conducted in a flowing system in order to more closely approximate real engineering situations.

1.2 Objectives and Scope of the Investigation

This investigation has focused on the initial stages of cavitation erosion using a ductile material, namely pure aluminum, in a flowing system employing water as the working fluid. It is not a study of the erosion of aluminum, but the aluminum was used as a device for recording the intensity of each cavitation bubble collapse. The damage to the surface of a ductile material is initially in the form of small indentations in which no material is removed. The name most often given to this regime of cavitation damage is the "incubation zone" as named by Thiruvengadam (2). It has been shown (3) that, in the

incubation zone, each indentation is produced by the collapse of one cavitation bubble. There is then a one-to-one correspondence between the bubble collapse and the damage thereby produced.

If the duration of exposure to cavitation is increased past the incubation zone, weight loss will occur. In most previous investigations, cavitation damage has been assessed by the rate of weight loss. However, in the weight loss zone, there is no one-to-one correspondence between damage and a single bubble collapse as in the incubation zone. In the weight loss zone, damage can be caused by hydrodynamic blows of many bubbles. Furthermore, the problem is further complicated in this zone by possible interactions between cavitation erosion and corrosion. Because of the aforementioned complexities of the weight loss zone, it was decided that this investigation should be conducted in the incubation zone where there is a one-to-one correspondence between cavitation damage and the collapse of a single bubble.

The major goal of the investigation was to observe the effect of velocity, cavity length, and air content on the rate of cavitation damage in the incubation zone with velocity as the primary variable. It has been shown by Knapp (3) that the rate of cavitation damage in the form of small indentations in a model's surface increases with the sixth power of velocity. Knapp's study was conducted over a relatively narrow velocity range (~18 to 30.5 m/sec). A much larger range of velocities (14.9 to 59.3 m/sec) was employed for this investigation.

The number of pits produced on a model's surface can be used as a measure of cavitation damage. However, the size of the individual pits should also be considered. By knowing both the number and volume of the pits a more complete assessment of damage is possible.

The volume of each indentation in the surface is proportional to the cavitation bubble collapse energy absorbed by the model. By recording both numbers and volumes of the indentations, a relative measure of the total collapse energy absorbed is known. The change in the rate of total collapse energy absorbed per second with velocity was investigated. It was necessary to relate the volume of each cavitation damage pit to the energy of formation. A hardness test which measures the surface hardness of the model material at a high strain rate, termed a dynamic hardness test, was devised for this purpose. The determination of the surface hardness at a high strain rate would more closely approximate the conditions encountered during the production of a cavitation pit. A static hardness test could not do this.

The model utilized in the course of this investigation was a 0.635 cm diameter zero-caliber ogive with the area of the model subject to cavitation damage constructed of annealed 1100 aluminum. The damage was assessed with the use of an optical and a scanning electron microscope. A high speed photographic study was also undertaken to observe cavity dynamics.

1.3 Summary of Previous Investigations

A classic paper on the subject of cavitation damage is that by Knapp (3) in 1955. Knapp investigated the cavity flow and cavitation damage on a 5.08 cm diameter hemispherical-nosed body. The damage was in the form of small indentations in the surface of the test body made of commercially pure annealed aluminum. Knapp reasoned that, since the test body is very soft, even bubbles with fairly limited "collapse

energy" would deform the surface. Knapp noted that for a constant cavity length, i.e., cavitation number (σ), the rate of pit formation per unit area increased with the sixth power of velocity.

From his study of developed cavitites, Knapp observed that the wall of the cavity was actually comprised of numerous traveling cavitation bubbles swept along the cavity wall. Knapp attributed the damage to the collapse of these traveling cavities. More recent studies (4,5) of the pitting rate on an annealed aluminum body tend to confirm the sixth power variation with velocity. Preliminary tests of cavitation damage due to the flow over a 0.635 cm high step mismatch were conducted at the Garfield Thomas Water Tunnel by Hackworth and Arndt (4). They found that the pitting rate very closely followed Knapp's data over a range of velocity 16.8 to 21.3 m/sec. Tests conducted in Japan at the Department of Naval Architecture of Tokyo University by R. Sato, H. Kato, and S. Tamiya (5) over a wider range of velocities, namely, 30 to 70 m/sec, also indicated that the pitting rate varied with the sixth power of velocity. The test body utilized in the tests of Sato et al. was a 1 cm diameter hemispherical-nosed body.

In all of the aforementioned studies (3,4,5), not only was the velocity power law confirmed, but the magnitude of the pitting rate remained nearly constant at a given velocity over variation in model size and geometry. For these investigations, the measure of damage was in the form of indentations of the surface where no material has been removed. Other investigations have been conducted in the weight loss zone where the rate of cavitation damage was measured by the rate of weight loss. Kerr and Rosenberg (6) measured the rate of weight loss of radioactive paint in a turbine and showed that it increased with

the fifth power of velocity. Thiruvengadam (7) showed a sixth power law for the rate of weight lost due to cavitation damage on a rotating hydrofoil.

Not all investigations in the weight loss zone have obtained the same velocity power law. Rasmussen (8) measured the erosion of a circular cylinder placed downstream of a two-dimensional venturi. He found that the rate of damage increased with velocity, attained a maximum value and then decreased for higher velocities. In the case of cavitation damage in a rotating disk apparatus, he reported that the damage increased linearly with velocity. Thiruvengadam (9), also using a rotating disk apparatus, observed an increase and then a decrease in the damage rate with velocity. One possible explanation for these discrepancies is that the investigators failed to conduct the investigations at a constant cavitation number. Shal'nev (10) has shown that, at constant velocity, the damage rate varies in a nonlinear way with cavitation number. The damage rate reaches a peak value at a given cavitation number and then decreases with further lowering of this parameter. Secondly, for the case of the rotating disk, the flow around such an object is highly complex and uncertain. This could possibly affect the damage rate. Also, since these investigations were conducted in the weight loss regime, there is the possibility of weight loss by cavitation-corrosion interactions.

The subject of cavitation damage scaling constitutes only a small part of the literature. Theoretical and experimental studies of bubble dynamics aid in the determination of the mechanism of damage. Many studies have been devoted to the classification of materials according to the relative resistance to cavitation damage and most of

these studies have been conducted with the magnetostrictive device. Although this device only vaguely approximates the conditions in a flowing system, its low cost and rapid rates of damage have made it the most widely used tool. However, there have been some studies of the relative resistance of materials to cavitation damage in a flowing system. See, for example, the studies conducted by Mousson (11) with a venturi device. With the enormous amount of time and money spent in the study of all phases of cavitation damage, the problem of predicting the damage to a prototype is yet unsolved.

CHAPTER II

DESCRIPTION OF THE INVESTIGATION

2.1 Plan of the Investigation

The water tunnel testing was divided into three main phases. The initial phase was conducted in the 30.5 cm cavitation tunnel, while phases two and three were in the 3.8 ultra-high-speed cavitation tunnel. Both facilities are a part of the Garfield Thomas Water Tunnel of the Applied Research Laboratory complex at The Pennsylvania State University.

The Phase I tests in the 30.5 cm tunnel were conducted as a preliminary investigation prior to testing in the high speed tunnel. A few of the areas of interest in conducting this phase of investigation were as follows:

1. How long should a model be run to obtain a sufficient damage sample for analysis?
2. Does the duration of the test affect the rate at which pits are produced?
3. Could the results be reproduced, i.e., given the same flow conditions and test duration, would the damage be the same?
4. What form would the damage be in (large pits, small pits, deep, shallow, etc.)?

The main phases of the investigation, Phases II and III, were conducted in the 3.8 cm cavitation tunnel. All the scaling relationships were developed in this tunnel. The Phase II tests were run at high air contents while Phase III was conducted at lower gas contents. High speed movies of the cavity behavior were also shot in this tunnel.

The models utilized in the investigation were 0.635 cm diameter zero-caliber ogives with an annealed 1100 aluminum cavitation damage probe. A wide range of velocities and cavity lengths were tested to observe the effect upon the rate of damage production. The velocity was varied from 14.9 to 59.3 m/sec in intervals of 7.6 m/sec. The cavity length was expressed in nondimensional form by dividing the length of the cavity by the model diameter (L/D). The range of dimensionless cavity lengths was 1.0 to 6.0.

This corresponds to a change in the cavitation number (σ) from 0.625 to 0.316, where σ is defined as

$$\sigma = \frac{P_{\infty} - P_C}{1/2 \rho_L V_{\infty}^2} \quad (1)$$

where P_{∞} is the free stream static pressure, P_C is the cavity pressure, ρ_L is the mass density of the liquid, and V_{∞} is the free stream velocity. A plot of σ vs L/D obtained from Reference 12 is presented in Figure 1. The air content of the water was varied from 10 to 20 parts per million (ppm) on a molar basis to test its effect upon the damage. For each test, a new model was machined and annealed to retain a permanent record of the accumulated damage.

An important requirement had to be met in order that the analysis be valid. The damage rate for a given flow condition had to be independent of the test duration. At first, this would seem logical since, if the flow conditions did not change, it would be expected that there would be twice as many pits for a two-hour test as for a one-hour test. This would probably not be the case though if the number density of pits became so great as to overlap. Annealed pure

aluminum is a material susceptible to work hardening. If a bubble collapses and produces an indentation, the surface is deformed and work hardened. If another bubble collapses in the same area with the same energy, it will "see" a greater surface hardness due to the work hardening. The resulting deformation will then be less for the same impact energy.

Care was taken by a suitable choice of test duration to insure that the pits were in sufficient density for ease of analysis, but not so close as to overlap. A special test was conducted during Phase I to determine whether, in fact, the damage rate was independent of test duration.

The damage was analyzed with an optical microscope, measuring the number and diameter distribution of the pits. As mentioned previously, the volume of a cavitation pit is a measure of the bubble collapse energy absorbed. A technique for measuring the volumes of the pits was also developed. The pits were assumed to be spherical segments to aid in the volume computation. From the volume of each pit, an estimation of the total energy required to form it could be made. The material property of the aluminum that would give the closest measurement of this energy for a given indentation volume is a surface hardness measurement. Most hardness tests though are conducted at nearly a zero strain rate, but in the formation of a cavitation pit, the strain rates involved are very high. To account for this fact, a surface hardness measurement at a high strain rate is required. To approximate this condition, a dynamic hardness test was devised (Appendix A). From these measurements of the dynamic hardness of the 1100-0 aluminum, an

approximate measure of the energy required to form a given pit was obtained.

Knowing the rate of pit production, the average pit volume for a given flow condition and the dynamic hardness of the model material, a scaling relationship between the velocity and cavitation bubble collapse energy absorbed was developed. This was probably the most important phase of the investigation, since it involved a scaling of the total damage (and damage potential energy) on a one-to-one correspondence with the bubble collapse.

Since the material utilized as the damage probe was so very soft, even a cavitation bubble with relatively low collapse energy will cause an indentation in the surface. The observation of a wide range of energies is then possible. The collapse energy distribution for the same flow conditions will remain unchanged irrespective of the test body material; only the response of various test materials to the applied hydrodynamic forces will change. This itself is most helpful in an understanding of the processes involved in the study of cavitation damage.

An optical microscope provides a sufficient magnification and depth of field for general analysis of the damage, but for a clearer view of the individual pits, another type of instrument is required. The scanning electron microscope (SEM), Appendix B, provides both high magnification capabilities with large depth of field not possible with normal optical methods. Individual pits were observed and photographed with the use of a SEM for a better view of the damage. Observations of the pits could provide some indication as to the mechanism of formation.

Even at this time, the actual mechanism of cavitation damage is not known for certain (Appendix C).

A further study was conducted involving the dynamics of the developed cavity on the test body with the use of high speed cinematography. This was done to possibly correlate the observed mechanics of the cavity and the damage produced.

2.2 Water Tunnel Facilities

Two continuous circuit water tunnels were utilized in the course of this investigation. The Phase I tests were conducted in a medium velocity tunnel at velocities up to 21.3 m/sec in a 30.5 cm circular test section. Extensive degassing equipment is available which allows variation of the total gas content. A more detailed description of this facility may be found in References 13 and 14.

The primary test facility for this investigation was the ultra-high-speed cavitation tunnel which was designed and constructed under NASA sponsorship, shown in Figure 2 and described in Reference 15. This facility which has a test section diameter of 3.8 cm is capable of speeds on the order of 92 m/sec while maintaining a stagnation pressure of over 8.3×10^6 pascals. The tunnel is constructed almost entirely of stainless steel with the exception of the bronze centrifugal pump and a plexiglass test section used for all photographic work. Pressurizing of the tunnel system is accomplished with the use of a nitrogen pressurized accumulator tank and a triplex pump. A vacuum system for deaeration of the tunnel water was constructed for the Phase III tests.

Two test sections were employed in the investigation in the high velocity tunnel. The first was a Type 416 stainless steel test section capable of high pressures and was used for all damage tests. The second was a plexiglass test section which as stated previously was used for all high speed photographic work. Since the plexiglass test section is cylindrical, there was difficulty in photographing the model due to distortion. To alleviate this problem, a plexiglass photographic box, Figure 3, with parallel windows was constructed around the test section. The box was filled with water, which has nearly the same index of refraction as plexiglass, to eliminate the image distortion.

2.3 Model Design and Construction

The model geometry used throughout the course of this investigation was a 0.635 cm diameter zero-caliber ogive, a blunt body with sharp edges. The cavitation damage probe (area of model in which the damage is to be measured) was made of 1100-F aluminum. This type of aluminum is 99% pure with the remaining percentage composed of iron, silicon and copper with trace amounts of zinc and manganese. The number 1100 is the alloy distinction (99% pure) and the letter following the number is the temper designation. For this case, F means as fabricated or no heat treatment in the stock material. All the test probes were fabricated from the same stock to eliminate any possibility of variations in alloy content. Three model designs were employed in the test programs. Sketches and photographs of these models are shown in Figures 4a, 4b, 4c and 5.

The nine models for the 30.5 cm tunnel tests, Phase I, were constructed entirely of aluminum, Figure 4a, with the surface finish

machined an RMS average surface roughness of 3 μm . Three models were left with the machine tool marks and the remaining models were given various degrees of polish. It was not known what type of surface finish would be most conducive to observation of the damage pits. Since the aluminum utilized in this investigation was so soft, there was some difficulty in obtaining a good polish by conventional means. Good results were obtained with the following procedure. The models were first rubbed with a soft chamois impregnated with jewelers brown tripoli which is a silica compound. This provided a fine satin-like finish on the models. Some of the models were polished to the satin-like finish whereas the other models had a finer finish. The finer finish was obtained by rubbing the model with a chamois, this time impregnated with jewelers red rouge which is a powdered hematite. After the desired degree of polish was reached, the models were annealed at 354 °C for one-half hour until the models had reached a 1100-0 temper which is referred to as "dead" soft.

After the initial phase of testing, it was observed that the leading edge contour of the all aluminum models was deformed at velocities above 19.8 m/sec. Since this alters the flow field and may have an effect upon the damage rate, a new model was designed for the Phase II and III tests in the 3.8 cm water tunnel, Figure 4b. A Type 316 stainless steel tip was fabricated which could screw into the forward portion of the aluminum damage probe. The stainless steel is much more durable than the aluminum and would not deform at the highest test velocities. The portion of the tip exposed to the cavitation was made as small as possible, 1.27 mm, so that the maximum area over which

the cavity extended would be aluminum and thereby susceptible to cavitation erosion.

All models for Phases II and III were polished, since the Phase I tests indicated that pit observation was easier on polished surfaces. The procedures for polishing and annealing the models were the same as employed in Phase I.

One further modification was made in the model design during the course of the investigation. At very high velocities, above 45 m/sec, the models would bend slightly about the thinnest part of the model (threaded section) due to the dynamic force of the water. It was feared that at higher velocities, a model could break off at the weak point. For these velocities, a shortened aluminum model was made, Figure 4c, which would reduce the moment about the junction point. A stainless steel tip was used as in the other tests, and a 3.3 cm long stainless steel afterbody was also constructed. The function of the afterbody was to ensure that the leading edge of the model for these tests was at the same axial position in the tunnel test section as the previous models.

2.4 Water Tunnel Test Procedures

The Phase I testing was conducted in the 30.5 cm cavitation facility. The maximum velocity of the tunnel is approximately 25 m/sec and it was not known if a sufficient damage sample could be obtained in a reasonable test duration. A run time of 30 minutes was chosen for a velocity of 21.3 m/sec and a cavity length of $L/D=2.0$. This proved to be a reasonable test duration for the given conditions since there was a sufficient number of pits for analysis without the pits overlapping. Seven other models were tested in this series with the

the cavity extended would be aluminum and thereby susceptible to cavitation erosion.

All models for Phases II and III were polished, since the Phase I tests indicated that pit observation was easier on polished surfaces. The procedures for polishing and annealing the models were the same as employed in Phase I.

One further modification was made in the model design during the course of the investigation. At very high velocities, above 45 m/sec, the models would bend slightly about the thinnest part of the model (threaded section) due to the dynamic force of the water. It was feared that at higher velocities, a model could break off at the weak point. For these velocities, a shortened aluminum model was made, Figure 4c, which would reduce the moment about the junction point. A stainless steel tip was used as in the other tests, and a 3.3 cm long stainless steel afterbody was also constructed. The function of the afterbody was to ensure that the leading edge of the model for these tests was at the same axial position in the tunnel test section as the previous models.

2.4 Water Tunnel Test Procedures

The Phase I testing was conducted in the 30.5 cm cavitation facility. The maximum velocity of the tunnel is approximately 25 m/sec and it was not known if a sufficient damage sample could be obtained in a reasonable test duration. A run time of 30 minutes was chosen for a velocity of 21.3 m/sec and a cavity length of $L/D=2.0$. This proved to be a reasonable test duration for the given conditions since there was a sufficient number of pits for analysis without the pits overlapping. Seven other models were tested in this series with the

flow conditions specified in Table I. Air content readings were not taken at this time but the air content was estimated to be quite low. The source of water for this facility is a reservoir shared with the 1.22 m water tunnel, with the inlet pipe drawing from the bottom of the reservoir. During these tests, there was a study being conducted in the 1.22 m tunnel at low air contents. It is probable that the reservoir water and, hence, the water for Phase I tests was partially deaerated.

The test parameters for Phase II and III tests are presented in Table II. There were two separate testing procedures for the tests conducted in the ultra-high-speed water tunnel. Phase II procedures were for the high air content tests (~20 ppm) and Phase III procedures for the low air contents (~10 ppm). For the Phase II tests, the tunnel pressure was raised to the point where the desired cavity length would occur at the required velocity. These values were obtained from previous calibration runs. The tunnel inverter was placed on standby and the potentiometer set for the test velocity. The inverter was then put on the line which automatically raised the velocity in the tunnel to the desired level. As the velocity neared the test velocity, the cavity on the model would grow until it reached the predetermined value at stable conditions. A stopwatch used for the measurement of the test duration was started after stable conditions were reached.

During each test, the tunnel stagnation pressure, water temperature, and the pressure in the test section at a point just upstream of the model were measured. The test section velocity was obtained from the measured temperature and pressures. For the longer tests, two values of the water temperature were taken. At the end of the desired run

time for each test, the tunnel drive system was quickly shut down. During each test, the cavity length was held constant by observing a reference mark scribed on the model surface.

The procedures for conducting Phase III tests were similar to those for Phase II. One exception being that, in Phase III, the tunnel water was deaerated for approximately 2 hours until the air content level was near 10 ppm. During the shorter tests, at higher velocities, the air content was measured at the end of the test. For longer runs, the air content was measured at the beginning and end of the test and an average value was recorded. All air content measurements were made with a Van Slyke apparatus.

For Phase III, the velocity range was extended up to 59.3 m/sec. During a portion of the transient startup period during which the velocity was increasing to the test velocity, cavitation occurred on the model resulting in some accumulation of damage. The actual damage rate at any instant would depend upon the velocity and cavity length at that time. For cases where damage accumulated during the transition period could be significant, an adjustment in the measured pitting density was made for the calculation of the damage rate. This was necessary for tests at the high velocities where the test durations were very short. At these conditions, the accumulated damage during the transient period could constitute a sizable percentage of the total damage to the model. The procedure for making this adjustment for the damage rate is explained in Appendix D.

2.5 Analysis of Damage with the Microscope

The main instrument utilized in the analysis of the damage was an American Optical Microstar series light microscope. A Bausch and Lomb illuminator provided a bright collimated light source for viewing the shallow cavitation pits. The illuminator was placed at a very low lighting angle for best contour distinction.

The analysis of the damage for the Phase I models differed slightly from that of Phases II and III. The damage to the initial test models, i.e., those employed in Phase I was measured along a narrow strip parallel to the model's axis of symmetry from the leading edge to a point where the damage approached zero, Figure 6. This strip was divided into equal reference areas of 0.1016 mm by 1.016 mm. This reference area was chosen since it corresponded to the markings on the reticle scale used in the microscope at the viewing magnification, 150 X. The number of pits in each reference area along the surface was recorded. Since these areas were quite small, axial strips at three different circumferential locations were chosen for analysis to provide a better sampling. Thus, at each axial station along the model, there would be a data point indicating the number of pits in the sample area. The pit distribution along the model could be converted into a damage rate distribution by calculating the number of pits per square centimeter at any point and dividing by the total test duration. The average damage rate for any area on the model, such as the maximum damage zone, could then be calculated. In this analysis, pit diameters greater than or equal to 0.01 mm were recorded.

The damage analysis for the investigation in the 3.8 cm tunnel, i.e., Phases II and III, was similar to that employed in Phase I with

some modifications. After the Phase I tests, it was determined that pit counting at 100 X provided a better view than at 150 X. At the greater magnification, the depth of field is smaller and the pits are slightly blurred. Since these indentations are very shallow with indistinct boundaries, the blurred image makes observation more difficult and could increase the possibility of overlooking some of the smaller pits.

The reference area for each sampling in Phases II and III was increased to 0.508 mm by 1.016 mm with each station taken along the model in 0.508 mm steps, Figure 7. This was done for simplification of analysis by providing a larger reference area and would have little effect upon the results. It was also determined that the analysis of one strip along the model contained a sufficient damage sample. Since the models for the Phase II and III tests had the stainless steel tip, the damage analysis of the model would begin at a point 1.27 mm downstream of the leading edge. Again, pits down to approximately 0.01 mm diameter were counted.

2.6 Photomicrography

For a permanent record, sections of the models showing the damage were photographed. For an overall view of the total damage to a model, photographs were taken with a Nikkormat camera. An extension bellows with a 55 mm lens was used to obtain the desired magnification. Kodak High Speed Ektachrome, Plus-X and Tri-X films were used for these photographs. For a record at higher magnifications, photographs were taken through the microscope. An Edmund Scientific No. 41,100 and "T" adapters were used for connection of the microscope to the Nikkormat

camera. Also, a 4 x 5 Polaroid Pack camera designed for use with the American Optical microscope was used. Most photomicrography was accomplished at magnifications of 100 X to 150 X for best definition of the pits.

2.7 Scanning Electron Microscope

During the course of the investigation, a much clearer view of individual pits than could be obtained with ordinary optical means was desired. A most useful tool for the observation of the pits was the scanning electron microscope (SEM). The SEM provides a closeup view of the damage due to high magnifications together with depths of field up to 300 times that of optical methods. The relatively small amount of specimen preparation added to its versatility. A description of the SEM's operation is given in Appendix C.

There were two SEM's employed for this study, both of which were manufactured by the Japanese Electron Optical Laboratories (JEOL). A JSM-50A was used for most of the photographic work at magnifications between 100 X and 3000 X. This unit has two axis control with rotation and specimen stage tilt controls. Both secondary electron and backscatter modes were utilized. SEM Model Number JSM-1 was used primarily for qualitative compositional analysis with an energy dispersive X-ray detector.

2.8 Pit Volume Determination

As stated previously, one aim of this investigation was the development of a scaling relationship for the bubble collapse energy with velocity. To accomplish this, the volumes of a representative number of cavitation pits had to be measured. The determination of

the pit volumes at first proved to present a problem. The vast majority of the indentations were on the order of 0.05 mm in diameter with some as small as 0.01 mm. In addition, the pits tended to be very shallow. Measuring the pit depths from parallax measurements of photographs taken with the SEM proved difficult because the pits had such an indistinct boundary and reference points for the parallax measurements were difficult to observe.

It was noticed in the counting of the damage pits through the microscope that the lighting angle for viewing was critical. If the angle was too high, there was no shadowing and the pits were not visible. This effect was used in the calculation of the volumes of the indentations.

As an approximation, the damage pits were assumed to be spherical segments. A collimated light beam illuminated the pit as shown in Figure 8. The angle at which the light strikes the surface was adjustable. When the light beam is tangent to the side of the pit at the rim, there will be no shadow.

The individual pit was viewed with the microscope at 100 X. The angle of the light beam was raised until there is no shadow within the pit. By knowing this lighting angle, the pit diameter and the approximation to a spherical segment the pit volume can be calculated, as shown in Figure 9. A large number of pits were randomly chosen and the volumes measured using this procedure. An average pit volume for a given model was then obtained. Pit volume measurements were made for those models tested at a dimensionless cavity length of 3.0 at velocities of 30.1, 38.0 and 49.3 m/sec.

2.9 Determination of the Dynamic Hardness

The dynamic hardness test was used to obtain a relationship between the volume of a cavitation pit and the energy required to form it.

The apparatus constructed for the dynamic hardness test was fairly simple as illustrated in Figure 10. An electromagnet held the indenter, which was a hardened steel ball, a specified distance above the annealed aluminum sample on which the test was to be performed. When the current to the electromagnet was shut off, the indenter would fall and a strobe light flashing at the rate of 60 flashes per second illuminated the ball throughout its trajectory.

A camera shutter was opened when the ball started to fall. The trajectory was then recorded at intervals due to the strobe flash. The ball, after striking the sample, rebounded from the surface. A graduated rule next to the indenter trajectory was also recorded in the multiple exposure. The camera shutter was closed after the motion had stopped. The maximum point at which the images of the ball overlapped after impact is the rebound height as illustrated in Figure 11. Care was taken to adjust the camera field of view so that only the rebound from the surface would be recorded. This eliminated many confusing images of the ball's initial fall before striking the surface.

After each drop test, the diameter of the pit in the sample surface was measured to the nearest 0.005 mm with a microscope. By knowing the drop height, rebound height, ball mass, ball diameter, and the diameter of the pit formed by the ball, the energy per unit pit volume was calculated. This energy per unit volume is the dynamic hardness. Further explanation of the procedure for the calculation of the dynamic

hardness is given in Appendix A. Descriptions of similar devices for calculating the dynamic hardness can be found in Reference 16.

2.10 High Speed Photography of Cavity Oscillations

Past studies have shown that cavity motion is very unsteady for developed cavities. Thus, it was decided that a high speed study of cavity behavior could enhance the understanding of the cavitation erosion mechanism.

There were two basic setups used in the high speed photographic study. The first technique utilized transmitted lighting or backlighting where the camera and light source were on the opposite side of the object to be photographed. The second technique employed reflected lighting in which the camera and light are on the same side of the object. Each system had its advantages and disadvantages. Transmitted lighting makes the most efficient use of the available light but much of the flow detail is lost. On the other hand, reflected lighting shows more of the detail but requires considerable more light than backlighting.

Where general observations of the cavity fluctuations were needed, backlighting was used with a moderate speed film and the cylindrical strobe reflector. For a more detailed view of the flow, reflected lighting with high speed film and the parabolic strobe reflector was used. In all cases, a framing rate of 5000 pictures per second proved adequate for observation of the processes involved. See Appendix E for further detail concerning these apparatus and procedures.

CHAPTER III

DISCUSSION OF RESULTS

3.1 Phase I - 30.5 cm Water Tunnel Tests

As stated previously, Phase I was conducted as preliminary tests prior to the main phases of testing. The general areas of interest were test duration, test procedures, appearance of the cavitation damage, and reproducibility of results.

In Figure 12, it can be seen that for Model 1, the damage starts from zero at the leading edge, reaches a small peak at about 2.5 mm downstream, decreases to nearly zero and reaches a larger peak 11.7 mm from the leading edge. The larger peak corresponds to the point of cavity closure on the model, i.e., $L/D \approx 2$ for this model. Beyond this point, there is almost no damage.

Pitting was observed on all models except for those with the very short cavities, namely, Models 2 and 7. All models which experienced damage had two peaks in the damage distribution, namely, one near the leading edge and one corresponding to the point of cavity closure. For the lower velocities, the observed pitting was very low. It was also determined that on a polished surface, the indentations caused by the cavitation are much more distinct than for the surface that was not polished.

For one model, the pit distribution along the model was plotted and the damage rate computed. The average damage rate for Model 1 from the leading edge to a point on the body where the damage decreases to nearly zero was found to be $2.67 \text{ pits/cm}^2/\text{sec}$. When considering only

the area in which the damage is a maximum (8.64 mm from the leading edge to the cavity length reference mark), the average damage rate is 5.29 pits/cm²/sec.

It was found that, at 21.3 m/sec and L/D of 2.0, significant damage was observed after only 15 minutes of testing with a 30-minute run providing a good damage sample. With longer test durations, namely, 1 hour, the pits became so closely packed that overlapping commenced. A distribution of 4000 pits/cm² provided a sufficient number of pits for ease of analysis but not so many as to overlap. Knapp (3) stated that in his investigation of damage in the incubation zone, the rate of which pits were produced was a constant for given flow conditions. To verify this statement, two tests were conducted at a constant velocity and cavity length, but for different test durations. The accumulation of damage on the models in the maximum damage zone is shown in Figures 13 and 14. It is seen that the average damage rate in terms of pits per square centimeter per second of test duration, for these cases is nearly the same. For Model 1 at a velocity of 21.3 m/sec, a dimensionless cavity length of 2.0, and a test duration of one-half hour, the rate in the maximum damage zone was 5.29 pits/cm²/sec. For Model 5 with the same flow conditions but a shorter test duration, the rate was 5.22 pits/cm²/sec.

When the damage to Model 1 was compared to that of Model 3 for the same flow conditions and test duration, it was observed that the number of pits on the two were approximately equal. This showed that test results could be duplicated.

The indentations caused by the cavitation had a wide range of sizes. The largest were 0.15 mm in diameter, the smallest about 0.01 mm

across, with the majority of the pits being less than 0.025 mm in diameter. There was no material removed from the surface during the formation of these pits since the machine tool marks from machining the models were visible over the surface of the indentations. If any material had been removed, there would be a break in the tool marks on the body.

In some instances, a very few large pits where material was removed from the surface were observed. The appearance of these pits was totally different from that of the indentation type pits and, consequently, were not counted in the computation of the damage rate. These pits caused by material removal were many times larger than the indentation pits and had a very irregular shape as shown by the photograph in Figure 15. An interesting fact is that none of these pits were located in the area of maximum damage. Around the edges of the pits, the metal was discolored, having the appearance of corrosion products. If the material removal were due to a cavitation damage fatigue failure, the pits should be located in the zone of maximum damage, but this was not the case. Thus, this suggests that this type of damage was not due to fatigue failure caused by many collapsing bubbles. [Further investigation of this type of damage was conducted during the Phase II and III studies.]

Another unusual effect observed during Phase I was the indentation type pitting near the leading edge of the models. According to classical theories of cavitation damage, there should be no damage in this area. It was felt that the unsteady nature of the cavity behavior could have a bearing on the problem. It was for this reason that the high speed photographic study of cavity dynamics was conducted.

Knapp in his report on cavitation damage made no mention of pitting on the forward portion of the model. The most likely explanation for this fact is as follows. Knapp used a test model having a stainless steel hemispherical nose. From sketches of the model geometry shown on page 325 of Knapp, Daily and Hammitt (17), it is seen that the stainless steel portion extends into the zone of cavitation. From plots of the pitting rate along the model, it is seen that the first data point occurs approximately 5 mm downstream of the leading edge of the cavity. If the face the stainless steel section did extend into the area where leading edge damage could occur, there would be no damage since stainless steel is far more resistant to cavitation damage than 1100-0 aluminum.

In the course of examining the models, it was noticed that for all models tested at 21.1 m/sec the leading edge contour had been deformed, but for the lower velocities, the model contour was not influenced by testing. These two conditions are shown in Figure 16. The deformation of the leading edge appeared to be a rim about the circumference of the model. It was felt that this deformation was not due to the dynamic action of the water alone since the total pressure on the model face was 2.3×10^5 pascals at 21.3 m/sec. This is far below the yield strength of 1100-0 aluminum. An examination of the front face of a model indicated the presence of many grooves extending radially outward from the center. Since the grooves were long and irregular in shape, it was felt that they were due to the abrasive action of impurities in the tunnel water striking the front face. This could be the reason for the deformation of the leading edge. The abrasive action could push the metal radially outward creating a lip around the circumference of

the models. To prevent leading edge deformations, a stainless steel tip was designed for the Phase II and III tests.

3.2 Classification of Damage - Phase II and III Tests

Since the distribution of pits on the model is not uniform, it was necessary to decide which pits were to be used in the computation of the damage rates. As stated in the results of Phase I, the damage rate was minimal at the front of the model with a small peak near the leading edge and steeply increases at a point just forward of the cavity closure point. It is obvious that the area in which the maximum damage occurs would provide the best measure of the intensity of the attack. In Phase I tests, the models for which a damage rate was computed were run at a dimensionless cavity length of 2.0. The maximum damage zone was defined as a point 8.64 mm from the leading edge to the cavity length reference mark (these reference marks were lines scribed about model used for setting the desired cavity length during a test). This area included most of the pits in the sample. For further tests, namely, Phases II and III, at other velocities and cavity lengths, the size of the maximum damage zone may vary. To account for this, a better definition of the maximum damage zone which would include most of the pits for all velocities and cavity lengths was required for these tests.

For the Phase II and III tests, the maximum damage zone was defined as follows. The three highest values obtained from counts in the individual reference areas on a model were averaged. The maximum damage zone extends outwards from either side of the peak values in the damage distribution to a point where the pitting has decreased to a

value of one-quarter of the average of the maxima. This area included most of the pits on each model for all test conditions. The reason an average of three maximum values was chosen was to eliminate the effect of a possible unusually high value in one particular reference area. Figure 17 indicates the calculation of the maximum damage zone for one model.

The damage rate was then computed for the maximum damage zone by calculating the average number of pits per square centimeter in this area and dividing by the total test duration. This damage rate in the maximum damage (DRMD) is one measure of the damage intensity. (A more complete measure of the damage intensity would include the average pit size.) The data could also be presented as a pitting rate where the number of pits per second are presented. This pitting rate can take two forms, namely, the pitting rate in the maximum damage zone (PRMD) or the total pitting rate (TPR) on the model. The PRMD is the number of cavitation damage pits formed per second in the area of maximum damage on the model. Likewise, the TPR is the number of pits formed per second on the entire model surface. Both the PRMD and the TPR are useful in an assessment of the damage.

For an indication of cavitation damage sustained by a model, not only the number of pits but the spatial concentration of pits also must be considered. Thus, all three of the aforementioned methods of the data presentation are necessary. The TPR gives a general measure of the total number of pits that can be expected on a model for a given test duration. When this value is compared to the PRMD, the percentage of pits in the maximum damage zone is known. The DRMD then indicates the pitting intensity in this area.

3.3 Dynamic Hardness

As mentioned previously, the dynamic hardness test was conducted to relate the volume of a cavitation pit to the energy required to form it. The results of the dynamic hardness test are shown in Table III. For the entire range of tests, the scatter in the data was quite small. The range of drop heights was from 20 to 100 cm for the 0.125 gm ball and from 20 to 30 cm for the 0.625 gm ball. The average dynamic hardness from all the tests was 0.50 Joules/mm^3 . It was this value of the dynamic hardness of the 1100-0 aluminum that was used in the energy scaling relationship.

As can be seen in the table, the dynamic hardness can also be expressed as a mean dynamic pressure. Most static hardness measurements are presented in the literature in the form of a pressure. The value for the mean dynamic pressure was obtained from the dynamic hardness measurement by multiplying by 1000 mm/m and dividing by the gravitational acceleration constant, 9.8 m/sec^2 . The average dynamic hardness expressed as a mean dynamic pressure is 50.9 kg/mm^2 . This compares to a value of 23 kg/mm^2 for 1100-0 aluminum in the standard Brinell hardness test (18), or in other words, the dynamic hardness is 2.2 times the static hardness.

The object of the dynamic hardness test was to provide a value of the energy required to form a pit of known volume in the surface of the test material at a high strain rate. The time of formation of a typical cavitation pit has been estimated to be on the order of a few micro-seconds (19). It was desired to conduct the dynamic hardness test so that the time of formation of a typical cavitation pit and pit formed during the hardness test would be of the same order of magnitude. An

approximate relationship for the time of pit formation during the dynamic hardness test was given in Appendix A. Using this relationship, a value of 7.9 μ seconds was obtained for the average time of pit formation during the dynamic hardness test. This value was obtained for the 0.125 gm ball.

Thus, it is seen that the estimated time for the pit formation in the dynamic hardness test and the estimated time to form a cavitation pit are of the same order of magnitude.

3.4 Effect of Cavity Length on Damage Production

During Phase III, a study of the effect of cavity length on the damage rate was conducted. The tests were conducted over a wide range of cavity lengths at a velocity of approximately 38 m/sec and an air content of 10 ppm. Seven cavity lengths corresponding to dimensionless cavity lengths of 1.0, 1.5, 1.75, 2.0, 3.0, 4.0 and 6.0 were tested. The results are shown in Figures 18 to 20 with the DRMD, PRMD and TPR plotted as a function of dimensionless cavity length and σ .

The production of damage is very low for the shorter cavity lengths, increases to a peak, and then drops off for the longest cavity tested.

The peak in the curves occurs at a $L/D=3.0$ for both PRMD and TPR, but at an L/D of 1.75 for the DRMD. This is because, for the shorter cavity, the area of the maximum damage zone, over which the damage rate was computed, is fairly small, giving a higher pitting rate per unit area. This is because the fluctuation in the cavity length is low for the shorter cavities. For the lower values of σ (longer cavities) during the damage tests, the fluctuations of the cavity length about

the mean point were greater than for the higher values of σ . The cavity length fluctuation became most pronounced for a dimensionless cavity length of 2.0 and above. This may have been due to slight fluctuations in the cavitation tunnel pressure. A plot of σ versus dimensionless cavity length is given in Figure 1. From this plot, it can be seen that for a given pressure fluctuation in the tunnel, the fluctuation in the cavity length will be more pronounced for the lower values of σ . Thus, for the longer cavity lengths the zone of maximum damage would tend to be larger due to changes in the cavity length.

At a dimensionless cavity length of unity, there is almost no damage to the surface. This concurs with results obtained for this cavity length at other velocities. In fact, no damage was recorded for $L/D=1.0$ at the high air contents and very little for the low air content tests. The flow over a zero-caliber ogive is a separated flow. For very short cavities, the cavitation bubbles grow and collapse in the free stream away from the model as shown by the photograph in Figure 21. At longer cavity lengths, the downstream portion of the cavity is attached to the model. This allows the bubbles to collapse close to the surface and increase the damage capability. For other model contours, this low rate of damage for the shorter cavity lengths may not be true. Knapp (3) in fact showed that for a dimensionless cavity length of 1.0 on a hemispherical-nosed body, a substantial amount of damage occurs. The flow about a hemisphere is essentially unseparated and thus the small traveling cavities are close enough to the model surface to cause damage even at the shorter cavity lengths.

For the velocity of 38 m/sec, a large number of cavity lengths were tested to observe any change in the damage rate. If these data are

compared to the data at other velocities, there may appear to be some discrepancy. At other velocities, the peaks in the damage and pitting rates occur at different cavity lengths. For some cases, the maximum occurs at a dimensionless cavity length of 4.0 while others occur at a dimensionless cavity length of 2.0 or 3.0. It is felt that this could be due to experimental error. Variations in the surface hardness of each model, errors in pit counting, air content effects, and other experimental errors could affect the results. From the tests conducted at 38 m/sec, the results show that for the dimensionless cavity lengths of 2.0, 3.0 and 4.0, the curve of the damage and pitting rates is fairly flat in this region. A small experimental error could shift the position of the peak in the curve.

3.5 Effect of Velocity on Damage Production

The main emphasis of this study was the investigation of Knapp's sixth power law. The data was plotted on log-log paper. If a power law holds the data should plot as a straight line with the slope being the exponent of velocity. As can be seen in Figures 22 and 23, the data for the DRMD scales by approximately the sixth power of velocity for the two air contents tested. Figures 24 through 27 show the same results when the PRMD and TPR are considered. The exponents vary from 5.4 to 6.5. It is interesting to note that the slopes of the graphs for the higher air content are greater than their counterparts for the lower air content. In the former case, the average slope of the graphs was 6.1. At the lower air content, the average slope was 5.4. As seen in the graphs, the data for dimensionless cavity lengths of 2.0, 3.0 and 4.0 are plotted on the same graph. It was shown previously that

for such cavity lengths, the damage rate does not change appreciably. Plotting all three cavity lengths provided a larger sample for plotting the curves.

For the highest velocity tests, a correction in the measured pitting density was made (see Appendix D). This was necessary since the amount of damage sustained during the velocity transition period was a significant percentage of the total damage. For test conditions of 49.3 m/sec-L/D of 3.0, 50 m/sec-L/D of 4.0, and 59.3 m/sec-L/D of 3.0, corrections were made in the pitting density. For the model run at 59.3 m/sec, the number of pits created during the velocity transition period constituted 35.4% of the total. This percentage of pits was subtracted from the total number of pits for the calculation of the damage and pitting rates at stable test conditions.

3.6 Effect of Velocity on Cavitation Bubble Collapse Energy

The velocity not only had a marked effect on the rate of pit production but also on the average volume of the pits formed. Tables IV to VI show a random sampling of pits for three models at velocities of 30.1, 38.0 and 49.3 m/sec for a dimensionless cavity length of 3.0. The average volume of a pit on a model increases greatly for an increase in velocity. As stated previously, the volume of a pit is a measure of the energy required to form it. A plot of average pit volume (and average collapse energy absorbed) as a function of velocity is presented in Figure 28, plotted on log-log paper. The energy values given correspond to a dynamic hardness of 0.5 Joules/mm^3 as measured from the dynamic hardness test for 1100-0 aluminum. The figure shows that the average pit volumes, or average collapse energy absorbed per pit,

scale to the fifth power of velocity. Since the pitting rate increases by the sixth power of velocity, and the average collapse energy absorbed by the fifth, the total cavitation bubble collapse energy absorbed per second increases to the eleventh power.

It must be mentioned that the pit volumes are not truly a measure of the bubble collapse energy. They are a measure of the bubble collapse energy absorbed by the model in the form of damage; the difference being the elastic energy in the formation of a cavitation pit. When a bubble collapses, it initially deforms the surface. There is some elastic recovery leaving the cavitation pit with a somewhat smaller volume. The ratio of the total energy to the elastic is important. The elastic energy must be a small percentage of the total collapse energy. If this is true, then the resulting deformation, the plastic energy, provides an accurate measure of the total collapse energy. This is the case for annealed aluminum. It is shown in Table III that the rebound height of the indenter in the dynamic hardness test is a small percentage of the drop height. In other words, the elastic energy is much lower than the total energy, usually less than 15% of the total. As the lower limit in pit size is reached, the elastic energy will constitute a larger percentage of the total. This would affect an assessment of the bubble collapse energy. Even with this statement, the average volume per pit still increases very rapidly with velocity indicating a corresponding increase in bubble collapse energy.

Plots of the pit volume distributions of the random sampling for the three velocities are presented in Figures 29 through 31. Since the pit volume is a measure of the collapse energy absorbed, a plot of

the volume distribution for a given flow condition is also a plot of the distribution of absorbed bubble collapse energy. Figure 32 is a very rough plot of the envelopes of the pit volume distribution graphs, accounting for the total number of pits in each sample. The plot was generated as follows. The abscissa was divided into equal absorbed bubble collapse energy levels of 2.5×10^{-6} Joules or a change in pit volume of $5 \times 10^{-6} \text{ mm}^3$ between each level. The relationship between the pit volume and collapse energy absorbed corresponds to 0.5 Joules/mm^3 , which was the result from the dynamic hardness test. The percentage of collapse energies absorbed within each level was then plotted. This was done for the three velocities tested. Even with such a small statistical sample, the relative partition of the absorbed bubble collapse energy is seen for each velocity. For the lowest velocity, there are large numbers of bubbles collapsing with relatively little damage to the boundary. As the velocity increases, there is a greater percentage of pits formed by a much higher collapse energy.

3.7 Effect of Air Content on Damage Production

From a study of the literature, it appears that the air content was not a major variable in most investigations. During this investigation, a significant effect of air content on the damage rate has been observed with a comparison of the data from Phases II and III. The effect of air content can best be seen in Figure 33. The upper curve is the DRMD as a function of velocity for an air content of approximately 10 ppm while the lower curve corresponds to data at 20 ppm. For a doubling of the air content, the damage rate is cut in half. One model, Model 52, was tested at a lower air content, namely, 7.1

ppm, to observe if the damage rate would further increase. The model was tested at a velocity of approximately 37 m/sec and a dimensionless cavity length of 3.0. The DRMD was 17.96 pits per cm^2 per second for an air content of 7.1 ppm. The DRMD was 11.21 pits per cm^2 per second for a model run at 9.5 ppm at approximately the same velocity and cavity length (Model 37). The damage rate does further increase for a decrease in air content. Model 19 was run at approximately these same conditions but at an air content of 18.5 ppm. The DRMD for this case was 6.90 pits per cm^2 per second. An air content of 18.5 ppm is 2.6 times that for 7.1 ppm. The damage rate for the lower air content was 2.6 times higher than for the higher air content. From this evidence, it would seem that a hyperbolic relationship exists between the damage rate and air content. This change in damage production due to variations in air content could be one source of scatter of data in the literature. Although no quantitative data were obtained due to the time element involved, the pits at the lower air content appeared to be slightly larger than their counterparts at the higher air contents.

If the damage rates for the Phase I models in the 30.5 cm tunnel are compared to the same flow conditions in the 3.8 cm tunnel, the damage rate is much higher for the former case. As stated previously, the air content was not measured for the preliminary tests, although it was estimated to be quite low. This could be the reason for the discrepancy. A rough approximation of the air content for the Phase I tests can be made. It is assumed that the hyperbolic relationship between the damage and air content holds. For Model 1 in the Phase I tests run at 21 m/sec and a dimensionless cavity length of 2.0 a DRMD

of 5.29 pits per cm^2 per second was recorded. A model from the Phase III tests with similar test parameters was chosen for comparison, namely, Model 34 tested at 23.2 m/sec and a dimensionless cavity length of 2.0. The DRMD for this case was 1.38 pits per cm^2 per second at an air content of 7.5 ppm. The damage rate for the Phase I model was 3.7 times higher than for a model run at similar test conditions at an air content of 7.5 ppm. Assuming the hyperbolic relationship between damage rate and air content, the Phase I model would have required an air content of the surrounding water to be 2.0 ppm. This value is just below the capabilities of the test facility utilized in Phase I. It is unlikely that the air content of the test facility could have been this low during the tests. The difference in the nuclei distributions between the facilities utilized for each of these tests could possibly account for some of the discrepancy.

3.8 Observations of Cavity Dynamics

The discovery of the damage near the leading edge of the Phase I models prompted an investigation into the possible cause. This study involved photographing the cavity behavior with a high speed motion picture camera. The developed cavity on a zero-caliber ogive is shown in Figure 34 as it appears to the naked eye. If the motion is stopped with a sufficiently short duration flash such as from a strobe light, the behavior appears as in Figure 35. This is a complete cycle of the cavity for a velocity of approximately 25 m/sec and a dimensionless cavity length of 2.5. The framing rate was approximately 5000 pictures per second or a 0.0002 second time lapse between frames. The cycle begins with a relatively long period during which the cavity remains

"steady". The cavity then breaks off at the leading edge and rolls back over the model usually in two separate segments. Small vortices usually connect the fragments as they travel downstream, Figure 36. The cavity breaks off due to a reentrant jet striking the cavity leading edge. This reentrant jet can be seen in Figure 37 moving through the cavity, striking the leading edge and causing the breakoff. A possible reason why the cavity usually divides into a number of pieces after breakoff is that the reentrant jet was thick enough to touch the cavity wall at a number of places. Also, surface tension effects may account for this.

From the movie segments, it was observed that the frequency of the cavity cycle was stable for any given flow condition. For the long cavity lengths ($L/D \geq 4.9$) and the shorter ones as well ($L/D \leq 1$), there was no cycling of the cavity. Inspection of the films for these cases shows that the reentrant jet for the long cavities loses its momentum before reaching the leading edge. For the short cavities, there is no reentrant jet and no well defined cavity. The data for the frequency characteristics of the cavity cycling for the cavities between dimensionless cavity lengths of 1.9 and 5.1 is presented in Table VII. Generally, as the cavity gets shorter, the frequency of cycling increases. Also, the frequency increases with velocity. Figure 38 shows a plot of Strouhal number, S , as a function of the cavitation index, σ . The Strouhal number is defined as

$$S = \frac{fD}{V_{\infty}} \quad , \quad (2)$$

where f is the frequency of pulsation, D is the model diameter, and

V_{∞} is the free stream velocity. On the whole, the Stouhal number increases with the cavitation index.

3.9 Leading Edge Pitting

The pitting of the model near the leading edge was first observed on the Phase I models. The leading edge contour was also deformed for some models during these tests; it was not known if this could be the cause of the pitting in this area. For the Phase II and III tests, the models had a stainless steel tip to prevent the contour deformation. The tip was made thick enough in the direction of flow for structural rigidity but thin enough that if pitting was possible near the leading edge, it should be visible on the aluminum.

This leading edge pitting was indeed observed on models in the 3.8 cm tunnel but only for some models tested at the lower air contents. Accurate measurements of the leading edge pitting could not be made since there was no damage in the area covered by the stainless steel tip. This may also explain why the pitting was not observed on all models at the lower air content.

It was seen previously from the high speed movie segments that a reentrant jet strikes the leading edge of the cavity during the cycling. The force of this jet striking the cavity wall could cause a substantial short term pressure rise. This pressure rise in turn could cause the collapse of any tiny cavitation bubbles near the leading edge and produce damage.

3.10 General Observations of the Damage

General observations of cavitation damage can provide insight into the processes involved in the cavitation damage. Figures 39 to 41

present views of cavitation damage to the models. Figure 39 shows how the damage appears to the naked eye with no magnification. The concentration of the pitting around the cavity length reference mark can be seen. The appearance of model surfaces before and after testing is seen in a magnified view of Figure 40. The approximate density of pits that provides a sufficient sample for analysis without overlapping is shown in Figure 41.

Pit diameters, depths, volumes and diameter-to-depth ratios are presented in Tables IV to VI for random samplings of pits. Measurements were taken for velocities of 30.1, 38 and 49.3 m/sec at a L/D of 3.0 and an air content of approximately 10 ppm. The minimum, maximum and average values are given for each sampling. The data show that the average pit diameter and depth increases with velocity but the average diameter-to-depth ratio is nearly the same for the models at 38 and 49.3 m/sec. Plots of the distribution of pit diameters for the three velocities are presented in Figures 42 to 44. These graphs were obtained from a much larger sampling than given in Tables IV to VI. (The data in Tables IV to VI was used mainly for the computation of the pit volumes.)

It was stated previously in the results of the Phase I tests that there was no material removal in the creation of the cavitation indentations. This statement was made after observation of the pits with an optical microscope. It was observed that there were no breaks in the tool marks running through the pits. After the Phase II and III tests, some models were viewed with the SEM. Figure 45 taken of the SEM screen shows clearly and at high magnification that there is indeed no material removal even from this relatively deep pit.

There was one interesting case of a very deep pit shown in Figure 46. At the very high magnification, it appears that the aluminum has been so strained that the surface at the bottom of the pit is starting to crack. This is an extreme case for the models studied and only one pit of this type was found. If another cavitation bubble were to collapse in the same spot, there could possibly be some material removed from the surface.

It was hoped that detailed observations of the damage would provide some indication as to the mechanism of damage. If the primary damage mechanism was caused by a final toroidal collapse, then there should be annular indentation in the surface. This was not observed. Also, there were no observations of pits distributed in a ringed pattern which could be characteristic of a final toroidal collapse mode. This does not rule out this mode totally; it would be difficult to observe any isolated pitting in a ringed pattern due to the relatively high density of pitting on the models. It could not definitely be stated whether the spherical collapse or jet mode was responsible for the damage. For some cases, the diameter-to-depth ratio of the pits was so small that a spherical collapse was unlikely. For these cases, the center of collapse would have to be so close to the surface that spherical symmetry would not be maintained. For other cases where the pits were very shallow (large diameter-to-depth ratio), the center of pressure for a spherical collapse would be farther from the surface. In these cases, the spherical collapse may be the cause of damage.

3.11 Corrosion Effects

When Phase II of the investigation was conducted in November 1974, an interesting characteristic of the model surfaces was observed. Phase II, as mentioned previously, was conducted at an air content of approximately 20 ppm. It was observed that, in addition to the normal indentations caused by the cavitation bubble collapse, there was sometimes a spotting of the model surface as shown in Figure 47. These spots had the look of corrosion products. At a magnification of about 100 X, Figure 48, it was observed that the spots were elongated in the direction of flow and seemed to start at a point at the upstream end becoming wider at the downstream end. Analysis with the SEM was conducted to determine the exact nature of the effect. SEM micrographs of individual spots are shown in Figure 49. The head of the spot is a small, irregular and deep crevice in the surface. This pit in which material had been removed was not visible with the optical microscope. The higher magnification micrographs taken with the SEM show that the tail is composed of small particles affixed to the surface downstream of the pit. The most likely explanation of this phenomenon is that it was a pitting type of corrosion with the corrosion products deposited downstream. The fact that the spotting is aligned with the flow is certain evidence that the pits were created during the cavitation test runs.

The important question to ask is what effect the cavitation itself had on the corrosion of the model. It was felt that the collapse of the cavitation bubbles near the surface could disrupt the protective oxide film and stimulate a pitting corrosion. (See Appendix F for more information on the corrosion of aluminum.) If this were true,

then it follows that little or no spotting should be observed when the pitting rate is low. It has been stated previously that, for a dimensionless cavity length of unity, the cavitation damage rate is very low. It was decided that the low damage rate was due to cavitation bubbles collapsing in the free stream away from the model surface. For this condition, then, the amount of spotting should be low. This was indeed the case. It was observed that very little spotting corrosion occurred for the tests conducted at the shortest cavity lengths, namely, dimensionless cavity lengths of one. For the longer cavity lengths, various amounts of spotting were recorded. This tends to confirm the fact that the collapse of cavitation bubbles near the surface of the model stimulates pitting corrosion. There is no quantitative data available on the effect of test duration and velocity on this corrosion. From general observations of the models, it appears that both an increase in test duration and velocity tend to increase the corrosion rate.

An interesting observation was made when the models were viewed under polarized light. Some of the corrosion pits had strong coloring rings about them, Figure 50. The colors observed were blues and brownish-oranges ringing the outer portion of the pit and tail section. The corrosion pits that had this coloring under polarized light were not usually as elongated as the other spotting. It was also observed that these colored pits were in far greater abundance at higher velocities. In some instances, pits were observed in which there was no elongation in the direction of flow. The pits were surrounded by concentric coloring rings. It was not known if these pits could have been formed during a period just before or after a test when there was stagnant water over the model. This could account for the fact that there was no elongation in the direction of flow. It was still

observed that for the higher velocity tests, there was a higher number of these pits.

The Phase III tests conducted at the lower air content were run in early 1975. Again, in addition to the indentation pits where no material was removed, there were corrosion associated pits. For the Phase III models, there was some spotting as observed for the Phase II models, but not as abundant. Instead, there were roughly ten very large material removal pits on each model. These pits were on the order of 0.2 mm in diameter, much larger than the spotting pits. SEM micrographs of the pits showed an attack along the cubic structure of the aluminum, Figure 51, and a thin deposit layer around the pits, Figure 52. This deposit layer was far different from the deposit tail of the spotting corrosion. The spotting deposit was in the form of small granules affixed to the surface downstream of the pit. These very large material removal pits had a thin even layer of deposits. In most cases, the layer was deposited in a circular pattern about the pit. The cracking of the layer showed a shrinkage after formation. There were some instances where the thin layer-type deposit was aligned with the flow. This was usually the case where the attack was along the cavity length reference mark and the layer deposited downstream as shown in Figure 53. A qualitative elemental analysis was conducted with a SEM which showed the layer composed of an aluminum compound. This would tend to confirm that a corrosion mechanism was responsible for the attack.

It was felt that the pits in which the layer was in a circular deposit pattern may not be due to cavitation-corrosion interaction. The procedure for conducting the Phase III tests involved deaerating

the water in the tunnel for about two hours. During this time, the model was in the tunnel and submerged. It was felt this pitting with the circular deposit was caused by simple pitting corrosion of the model during this time. The pits where the corrosion products are aligned with the flow were still most likely due to cavitation-corrosion interactions.

The question still arises as to why there was a smaller amount of the spotting-type corrosion for the models run at the lower air contents. Also, why were there pits at the cavity length reference mark with corrosion products deposited in a thin layer downstream. The rate of indentation type pitting was greater for the lower air content so the cavity collapse was more intense. This would tend to disrupt the protective oxide layer to a greater extent and thereby cause more corrosion. One explanation of the lower amounts of spotting could be the longer test durations for the high air content tests at given flow conditions. It is possible that even the less energetic bubble collapses are strong enough to disrupt the oxide film and any more collapse energy does not add to the effect.

Another reason for the change in the amount of spotting could be a difference in the water composition or pH between tests. The high air content tests were conducted in November 1974 while the lower air contents were tested in February 1975. The water supply taken from the tap at different times of the year may have a slightly different composition of dissolved constituents and pH. A small test was conducted in August 1975 to observe a change in the pH reading of the tap water used for the water used for the water tunnel facility. The maximum variation in pH was from 7.672 to 7.87 for water from the tap.

Deaeration of the water to about 5 ppm tends to increase the pH by only 0.05. An increase in the pH value on one hand would tend to increase the corrosion, while a decrease in the oxygen level would tend to decrease the tendency toward corrosion.

Pits that exhibited the color zones under polarized light were also observed for the Phase III tests. The very large pits with the deposit layer had this effect. It was generally observed that the more intense the attack in the pit, the higher the tendency toward observation of the color zones. The mechanism for this color generation is not known.

3.12 Comparison of Results with Other Investigations

One of the major problems in the study of cavitation damage in the weight loss zone is the lack of agreement between investigators. An example of this can be seen from the results of an ASTM round robin test with vibratory test facilities (20). Using similar test devices, eleven laboratories measured the accumulated damage to three materials. In some cases, there was a wide spread in the data. For this reason, a comparison was made between investigations of damage in the incubation zone using aluminum as a test body.

The model configurations and test data are shown in Table VIII for four different investigations. Data from Knapp (3), Hackworth and Arndt (4), Sato et al. (5), and this investigation are presented. All investigations measured the damage rate, in the form of pits per second per unit area, on a pure annealed aluminum model. Sato used Type A. A. 1080, Alcoa BC 1 S aluminum, 99.8% pure, while the others used 1100 aluminum, 99% pure. Knapp employed a 5.08 cm diameter hemispherical-nosed body while Sato's test body had a 1 cm hemispherical nose.

Hackworth and Arndt measured the damage downstream of a 0.635 cm high step mismatch and this investigation, a 0.635 cm diameter zero-caliber ogive. A range of cavity lengths and air contents were also contained in the data.

A plot of the damage rate as a function of velocity is presented in Figure 54 for all investigations. Good agreement in the data can be seen for the investigations. It was decided to correct all data to one air content. This was done using the hyperbolic relationship found from the tests conducted during this investigation. The results are shown in Figure 55. For such a wide variation of model size and geometry, the data corrected only for air content shows remarkable agreement. From this comparison, it would seem that the variation of the velocity overrides the differences with flow configurations and σ .

It was stated previously that there was a peak in the curve of damage and pitting rates as a function of the relative cavity length. This has also been observed by Shal'nev (10) using a circular cylinder normal to the direction of the flow in a two-dimensional venturi.

Pitting near the leading edge of a model as described in this study has been observed by other investigators. Rasmussen (21) noted damage near the leading edge of a developed cavity on a blunt body. He postulated that this was caused by the rupture force required to separate liquid from solid in this area, based on the theoretical tensile strength of water. Sato et al. (5) also observed this pitting near the leading edge of a cavity on a hemispherical-nosed body. They attributed the pitting to be caused by the collision of small metal particles in the test water. As stated previously, results of this investigation tend to show the damage is caused by the pressure rise

due to the reentrant jet striking the leading edge of the cavity. This pressure rise would tend to collapse any small cavitation bubbles in the area and cause pitting. If the damage were due to the collision of metal particles with the surface, the pits would be irregular in shape and elongated in the direction of the flow. This was not the case for this investigation. The pits were smooth round indentations, similar to the pits in the maximum damage zone. The rupture mechanism proposed by Rasmussen appears to be questionable since it has been shown (22) that the actual tensile strength of water is far below the theoretical value.

With reference to the cavity cyclic behavior, it was stated that the Strouhal number based on model diameter increases with cavitation index. The data of Knapp in Reference 17 and page 166 was plotted in similar fashion as shown in Figure 38. The similarity of results is apparent.

In reports of previous investigations in the incubation zone, there was no mention of corrosion of the models. This could be due to many reasons. The alloy content of the test materials for the other tests could have an effect upon the corrosion resistance. The most likely explanation is the differences in the water used in each facility. As stated in Appendix E, chloride ions and bicarbonate must be present, along with copper and oxygen for pitting to occur. The pH of the water in each test could also affect the corrosion resistance.

It was reported in this investigation that the average size of the cavitation pits increased to the fifth power of velocity and the total collapse energy absorbed per second to the eleventh. Sato et al. (5) also measured some pit volumes for their study, although the method for

determining the pit volumes and the overall pit volume scaling relationship is open to question. Their findings showed that the total rate of "volume loss", as it was termed by the investigators, was an exponential function of velocity. The data show a decrease in the rate of total volume loss for a change in velocity from 30 to 40 m/sec and then a rapid increase to the maximum test velocity of 70 m/sec. The decrease in the data may be due to experimental error in the method of volume measurement. Their data is shown in Figure 56 plotted on log-log graph paper. If the data point for a test velocity of 30 m/sec is discounted, the rate of volume loss shows an increase by approximately the tenth power of velocity. This is in reasonable agreement with findings of this investigation. Sato et al. also developed a relationship between the free stream velocity and the pressure field around a bubble. Their solution was based on that by Trilling (23) and found that the maximum pressure on the bubble wall varies with the eleventh power of velocity.

CHAPTER 4

CONCLUSIONS AND RECOMMENDATIONS

4.1 Summary of This Investigation

The damage in its initial stages was in the form of small indentations in the surface. The pits were round depressions usually under 0.1 mm in diameter with the majority less than 0.05 mm across. During the formation of these pits, it appears that no material was removed from the surface. For the incubation zone, the rate of damage accumulation is a constant for a given flow condition. Using an annealed 1100 aluminum test probe, a sufficient damage sample could be obtained in a relatively short period of time.

It was observed that the velocity has a marked effect upon the rate of damage production. For a velocity range from 14.9 to 59.3 m/sec, the damage and pitting rates increased by approximately the sixth power of velocity. The velocity also affected the sizes of the individual damage pits. The average volume of the pits increased by the fifth power of velocity. The volume of each pit is a measure of the energy required to form it so the average collapse energy absorbed increases to the fifth power of velocity. A relationship between the pit volume and the absorbed collapse energy was obtained by performing a dynamic hardness test on the model material. Since the pitting rate increases by the sixth power of velocity and the average collapse energy absorbed per pit increases by the fifth power, the total collapse energy absorbed by the model per second increases by the eleventh power. The pit volume is a measure of the bubble collapse energy

absorbed; therefore, a plot of the volume distribution for a given flow condition is also a plot of the bubble collapse energy distribution. Such a plot was generated to show the partition of collapse energies for three flow conditions.

It was observed that the air content and dimensionless cavity length also affected the damage. For a doubling of the air content from 10 to 20 ppm, the rate of damage production was cut nearly in half. There was almost no damage to the models for a very short cavity length. As the length increased, so did the damage. The damage reached a peak and then slowly dropped off for longer cavities.

From high speed movies of the cavity behavior, it was seen that the cavity regularly breaks off from the model surface. This is due to a reentrant jet moving through the cavity and striking the leading edge of the cavity. On many of the models, pitting was observed near the leading edge. It is felt that this could be a result of the reentrant jet behavior. When the jet strikes the cavity wall, it creates a short term pressure rise, causing any small cavitation bubbles in that area to collapse. If the collapsing bubbles are near the model surface, damage to the model could occur.

The effect of cavitation upon the rate of corrosion of aluminum was not fully explored. General observations showed a strong relationship between the cavitation and corrosion, with cavitation tending to increase the corrosion rate. For observation of the corrosion damage and cavitation pitting, the scanning electron microscope proved to be a most useful tool. Clear views of the damage were obtained at high magnifications and depths of field.

In general, good correlation of data was found when a comparison was made with the results of other investigations. The sixth power damage rate law and the actual damage rates involved showed good agreement with three other investigations. The interesting feature of this comparison is the fact that even though the size and shape of the models used in each of the four investigations were significantly different, the recorded damage rates were approximately the same on an equal velocity basis.

4.2 Recommendations for Further Study

It is felt that a study of cavitation in its initial stages can provide much useful information. More investigation is needed in many areas. Tests with varying model sizes and geometries should be run to be certain of any scaling relationships. A most important study would be to develop possible relationships between damage in the incubation zone and in the weight loss regime. Care would have to be taken to avoid cavitation-corrosion interactions. A useful investigation could be a study where, at one set of flow conditions, models were run for successively longer periods of time. The transition from incubation-to-weight loss can then be observed. Observation of the damage with the SEM could then provide information as to the steps involved for weight loss due to cavitation.

The concept of the bubble collapse energy distribution should be more fully explored. This could be a most useful tool in the study of cavitation damage leading to the eventual prediction of damage sustained by a prototype in the field. Bubble energy distributions for a wide range of test conditions could be generated. For set flow

conditions, these energy distributions would not change regardless of the test material utilized; only the material response would change. A study of the response of materials to impact loading, such as that encountered in the cavitation damage process, is necessary. The problem then is separated into the hydrodynamic aspects and the mechanical response of materials. It is felt that such a step-by-step approach to the cavitation damage problem could lead to the prediction of damage to a prototype.

REFERENCES

1. Silberrad, D., "Propeller Erosion," Engineering, p. 33, January 12, 1912.
2. Thiruvengadam, A., "A Comparative Evaluation of Cavitation Damage Test Devices," Hydronautics, Incorporated, Technical Report 233-2, 1964.
3. Knapp, R. T., "Recent Investigations of Cavitation and Cavitation Damage," Trans. ASME. 77, pp. 1045-1054, 1955.
4. Hackworth, J. V. and Arndt, R. E. A., "Preliminary Investigations of the Scale Effects of Cavitation Erosion in a Flowing Media," 1974 Cavitation and Polyphase Flow Forum, ASME.
5. Sato, R., Kato, H. and Tamiya, S., "Study on Cavitation Erosion," J. Soc. Nav. Archit. Japan, pp. 43-63, November 1973 (in Japanese).
6. Kerr, S. L. and Rosenberg, K., "An Index of Cavitation Erosion by Means of Radioisotopes," Trans. ASME, Vol. 80, No. 6, pp. 1308-1311, August 1958.
7. Thiruvengadam, A., "Scaling Laws for Cavitation Erosion," Hydronautics, Incorporated, Technical Report 233-15, p. 8, December 1971.
8. Rasmussen, R. E. H., "Some Experiments on Cavitation Erosion in Water Mixed with Air," Cavitation in Hydrodynamics, (Proc. Nat'l Phys. Lab. Symp.), Paper No. 20, H. M. Stationery Office, London, 1956.
9. Thiruvengadam, A., "Handbook of Cavitation Erosion," Hydronautics, Incorporated, Technical Report 7301-1, p. 98, January 1974.
10. Thiruvengadam, A., "Handbook of Cavitation Erosion," Hydronautics, Incorporated, Technical Report 7301-1, p. 99, January 1974.
11. Mousson, J. M., "Pitting Resistance of Metals Under Cavitation Conditions," Trans. ASME, 59, pp. 399-408, 1937.
12. Weir, D. S., "An Experimental and Theoretical Investigation of Thermodynamic Effects on Developed Cavitation," The Pennsylvania State University, ARL TM-34, February 21, 1975.
13. Holl, J. W., "Cavitation Research Facilities at the Ordnance Research Laboratory of The Pennsylvania State University," presented at the Symposium on Cavitation Research Facilities and Techniques, Fluids Engineering Conference, ASME, Philadelphia, Pennsylvania, May 18-20, 1964.

REFERENCES (CONT.)

14. Lehman, A. F., "The Garfield Thomas Water Tunnel," Ordnance Research Laboratory, The Pennsylvania State University, Serial No. NOrd 16597-56, September 30, 1959.
15. Weir, D. S., Billet, M. L. and Holl, J. W., "The 1.5 Inch Ultra-High-Speed Cavitation Tunnel at the Applied Research Laboratory of The Pennsylvania State University," ARL TM 75-188, July 10, 1975.
16. Tabor, D., The Hardness of Metals, pp. 115-140, Oxford, 1951.
17. Knapp, R. T., Daily, J. W. and Hammitt, F. G., Cavitation, McGraw-Hill, p. 325, 1970.
18. Aluminum, Vol. 1, prepared by Aluminum Company of America, Edited by R. Van Horn, Metals Park, Ohio, American Society for Metals, p. 312, 1967.
19. Eisenberg, P., "Cavitation," International Science and Technology, pp. 72-84, February 1963.
20. Hammitt, F. G., Chao, C., Kling, C. L., Mitchell, T. M., and Rogers, D. O., "ASTM Round Robin Test with Vibratory Cavitation and Liquid Impact Facilities of 6061-T6511 Aluminum Alloy, 316 Stainless Steel, and Commercially Pure Nickel," Materials Research and Standards, Vol. 10, No. 10, pp. 16-23, October 1970.
21. "Handbook of Cavitation Damage," Hydronautics, Incorporated, Technical Report 233-8, p. 26, March 1965.
22. Knapp, R. T., Daily, J. W. and Hammitt, F. G., Cavitation, McGraw-Hill, p. 52, 1970.
23. Trilling, L., "The Collapse and Rebound of a Gas Bubble," J. Appl. Phys., 23, pp. 14-17, 1952.
24. Rayleigh, Lord, "On the Pressure Developed in a Liquid During the Collapse of a Spherical Cavity," Philosophical Magazine, Series 4, Vol. 34, pp. 94-98, 1917.
25. Hickling, R. and Plesset, M. S., "Collapse and Rebound of a Spherical Bubble in Water," The Physics of Fluids, Vol. 7, No. 1, pp. 7-14, January 1964.
26. Plesset, M. S. and Mitchell, T. P., "On Stability of the Spherical Shape of a Vapor Cavity in a Liquid," Quarterly J. Appl. Math., Vol. XIII, No. 4, p. 419, January 1956.

REFERENCES (CONT.)

27. Rattray, M., "Perturbation Effects in Bubble Dynamics," Ph. D. Thesis, California Institute of Technology, June 1951.
28. Kornfeld, M. and Suvorov, L., "On the Destructive Action of Cavitation," J. Appl. Phys., Vol. 15, pp. 495-506, June 1944.
29. Naudé, C. F. and Ellis, A. T., "On the Mechanism of Cavitation Damage by Nonhemispherical Cavities Collapsing in Contact with a Solid Boundary," Trans. ASME, Vol. D83, J. Basic Eng., p. 648, 1961.
30. Benjamin, T. B. and Ellis, A. T., "The Collapse of Cavitation Bubbles and the Pressures Thereby Produced Against Solid Boundaries," Phil. Trans. Royal Soc. London, A, Vol. 260, pp. 221-240, 1966.
31. Shutler, N. D. and Mesler, R. B., "A Photographic Study of the Dynamics and Damage Capabilities of Bubbles Collapsing Near Solid Boundaries," J. Basic Eng., Paper No. 64-WA/FE-13, 1964.
32. Ellis, A. T., "On Jets and Shockwaves from Cavitation," 6th Naval Hydrodynamics Symposium, Washington, DC, September 1966.
33. Taylor, G. I. and Quinney, H., "The Latent Energy Remaining in a Metal After Cold Working," Proc. Royal Soc. London, Series A, Vol. 143, 1933-34.
34. Thiruvengadam, A., "Handbook of Cavitation Erosion," Hydronautics, Incorporated, Technical Report 7301-1, p. 145, January 1974.
35. Thiruvengadam, A., "Handbook of Cavitation Erosion," Hydronautics, Incorporated, Technical Report 7301-1, p. 147, January 1974.
36. Thiruvengadam, A., "Handbook of Cavitation Erosion," Hydronautics, Incorporated, Technical Report 7301-1, p. 148, January 1974.

APPENDIX A

THE DYNAMIC HARDNESS TEST^{*}

The dynamic hardness is a measure of the energy required to generate a pit of a known volume at a high strain rate. In a dynamic hardness test, a hardened steel ball is dropped onto the test surface and the height of the rebound is measured. By knowing the change in energy between the drop height, and rebound height, and the volume of the pit thus formed the energy per unit volume of material displaced is calculated.

The dynamic hardness can also be thought of as a mean dynamic pressure resisting the deformation. As a first approximation, it is assumed that this pressure is a constant throughout the duration of the impact.

By definition:

$$P_D = H_D = \frac{E_1 - E_2}{V_p}, \quad (3)$$

where E_1 and E_2 are the drop energy and rebound energy, respectively, V_p is the volume of the indentation, and P_D or H_D are the measure of the dynamic hardness, P_D given in units of pressure and H_D in units of energy per unit volume.

The indenter, a hardened steel ball, has a mass, m , a radius of curvature, r_1 , and falls from a height, h_1 , onto the test body. After

^{*}This appendix is based on the information presented in Reference 16.

the ball strikes the body, it rebounds to a height, h_2 , and leaves an indentation of diameter $D_H = 2a$ in the surface, Figure 10.

Assume the energy of the rebound is equal to the energy involved in the release of the elastic stresses in the indentation, the radius of curvature of the pit, r_2 , will not be the same as the indenter, but will be somewhat greater. The relationship between r_1 and r_2 is to be determined.

Assume that the indenter were again placed in contact with the pit; the sides of the pit would not touch the side of the ball. If a suitable load, F , were applied to the ball, the ball would be in contact with the surface over a diameter $D_H = 2a$ which is given by Hertz's equation:

$$D_H = 2a = \left[6 \frac{F r_1 r_2}{r_1 + r_2} f(E) \right]^{1/3}, \quad (4)$$

where

$$f(E) = \frac{(1 - \sigma_I^2)}{E_I} + \frac{(1 - \sigma_M^2)}{E_M},$$

σ_I and σ_M are Poisson's ratio for the indenter and the material respectively, and E_I and E_M are the Young's moduli.

The force on the ball is initially zero and rises to the value, F , when the ball has full contact with the indentation as given by Equation (4). At any intermediate point in the deformation, the area of contact between the indenter and the sample has a diameter 2α , where $\alpha < a$, and the force on the indenter is given by:

$$F_I = F \frac{\alpha^3}{a^3} \quad . \quad (5)$$

The distance, z , the center of the indenter sinks below the initial point is given by:

$$z = \frac{3 F_I}{4\alpha} f(E) \quad . \quad (6)$$

Substituting Equation (5) into Equation (6) yields

$$z = \frac{3 F \alpha^2}{4a^3} f(E) \quad . \quad (7)$$

The total elastic energy is then given by the integral of

$$F_I dz = F_I \frac{3}{2} \frac{F\alpha}{a^3} f(E) d\alpha \quad . \quad (8)$$

After substitution for F_I ,

$$E_E = \int F_I dz = \int_0^a \frac{3}{2} \frac{F^2}{a^6} \alpha^4 f(E) d\alpha \quad (9)$$

$$= \frac{3}{10} \frac{F^2}{a} f(E) \quad , \quad (10)$$

where E_E is the total elastic energy.

The total elastic energy is equated to the energy of the indenter rebound

$$E_2 = E_E \quad (11)$$

or

$$mgh_2 = 3/10 \frac{F^2}{a} f(E) \quad . \quad (12)$$

As a first approximation, the volume of the permanent indentation, V_p , is given by

$$V_p = \frac{\pi a^4}{4r_2} \quad .$$

By definition,

$$E_1 - E_2 = mg [h_1 - h_2] \quad (13)$$

and

$$E_1 - E_2 = P_D \frac{\pi a^4}{4r_2} \quad . \quad (14)$$

Express the radius of curvature of the indentation, r_2 , in terms of r_1 , the indenter radius, by the use of Hertz's Equation, Equation (4),

$$\frac{1}{r_2} = \frac{1}{r_1} - \frac{3}{4} \frac{F}{a^3} f(E) \quad . \quad (15)$$

Hence,

$$E_1 - E_2 = P_D \left[\frac{\pi a^4}{4r_1} \right] - P_D \left(\frac{\pi a^4}{4} \right) \left[\frac{3}{4} \frac{F}{a^3} f(E) \right] \quad , \quad (16)$$

but by definition, at the end of the indentation,

$$F = P_D \pi a^2$$

since

$$F = \int_0^a P_D 2\pi x dx = P_D \pi a^2 \quad ,$$

so that

$$E_1 - E_2 = P_D \frac{\pi a^4}{4r_1} - \frac{3}{16} \frac{F^2}{a} f(E) \quad . \quad (17)$$

Compare the second term of Equation (17) to the total elastic energy, Equation (10),

$$\frac{3}{16} \frac{F^2}{a} f(E) = \frac{5}{8} E_E \quad . \quad (18)$$

Therefore,

$$E_1 - E_2 = P_D \frac{\pi a^4}{4r_1} - \frac{5}{8} E_2 \quad (19)$$

since,

$$E_E = E_2 \quad .$$

The dynamic hardness is then

$$H_D = P_D = \frac{mg(h_1 - 3/8 h_2)}{V_a}, \quad (20)$$

where

$$V_a = \frac{\pi a^4}{4r_1}$$

is the apparent volume of the indentation as if the pit had the same radius of curvature as the indenter.

The approximate time of formation of the pit created during the dynamic hardness test can be found from the following relations. Assume the indenter is undeformed during the collision, the impact is predominantly plastic, and that the dynamic hardness is an average constant throughout the collision.

Consider an indenter of radius, r_1 , and mass, m . At any instance during the collision, the indenter has penetrated a distance, z , with the indentation having a radius, a , where to a first approximation $2r_1z = a^2$. The force on the sphere at this time is $P_D \pi a^2$ or $P_D 2\pi r_1 z$, where P_D is the mean dynamic pressure.

The equation of motion is:

$$P_D 2\pi r_1 z = -m \frac{d^2 z}{dt^2} \quad (21)$$

or

$$\frac{d^2 z}{dt^2} + \frac{2\pi r_1 P_D}{m} z = 0 \quad (22)$$

The solution has the form

$$z = C \sin \sqrt{\frac{2\pi r_1 P_D}{m}} t \quad . \quad (23)$$

The end of pit formation occurs when $dz/dt = 0$ or when

$$t = \frac{\pi}{2} \sqrt{\frac{m}{2 P_D r_1}} \quad . \quad (24)$$

APPENDIX B

THE SCANNING ELECTRON MICROSCOPE

In the scanning electron microscope (SEM), a finely focused beam of high energy electrons (5 kev - 30 kev) is scanned across the surface of the sample in the form of a small rectangular raster. The high energy incident beam dislodges low energy electrons (1-50 ev) from the sample surface. The emitted low energy or secondary electrons are collected and accelerated by a high voltage grid to excite a scintillation detector. A photomultiplier tube then produces an electrical signal which is amplified and displayed on a cathode ray tube (CRT) as a spot.

The primary electron beam is scanned over the raster area in synchronization with the cathode ray tube beam. Hence, each point along the raster corresponds to an equivalent point on the CRT. The intensity of each point is modulated in proportion to the signal from the detector. It is the rapid display of the many points that together create the total image, much the same as on a television screen.

The display of the information can take various forms. The most widely used is the fast scan in which long glow phosphors on the CRT screen retain the entire image. For photographing the image, a slower scanning rate is used with a short glow phosphor CRT. The slow scan gives the detector a longer time to obtain a signal at each point and therefore increases the signal-to-noise ratio. The short glow phosphor increases the resolution of the image for photographic purposes. There are usually between 500 and 1000 lines per scan to present the final

image. The signal from the detector can also be fed directly into a computer or stored on tape for further analysis.

The magnification of the system at any time is equal to the ratio of the size of display to the distance scanned on the surface. The spatial resolution of the SEM is limited by many factors. When the incident electron beam strikes the sample, it may penetrate to a depth of several microns. After penetration, the beam also spreads out into a teardrop shape, Figure 57. The secondary electrons which are generated within 10 to 50 Å of the surface will escape and be collected. Even though the diameter of the incident beam may be as small as 5 Å at the surface, the spreading out after penetration decreases the resolution.

As the primary electron beam impinges on the surface, not all the electrons are absorbed, a small percentage have elastic collisions with the atoms of the sample and escape from the surface. These are high energy electrons that travel in straight lines and are termed backscatter electrons. The secondary electrons have to be drawn to the detector with the high voltage bias due to their low energy. If the bias on the detector is removed, the secondaries will not have the energy to reach the scintillator. The backscatter electrons with their higher energy can trigger a signal and be recorded.

The backscatter electrons are a most useful imaging mechanism. Since they travel in straight lines, they form very distinct shadow zones if an object on the surface blocks their path to the detector. The backscatter mode of operation is analogous to illumination of an object with a collimated light beam causing distinct shadow regions. The secondary electron image may be thought of as diffuse illumination where the contrast is not as great. The backscatter imaging is most

useful in observing structures with only slight topographical variation. Only a small percent of the backscatter electrons are collected, so the signal-to-noise ratio is much lower than in the secondary electron mode. This problem may be partially reduced if the area of observation is tilted towards the detector giving a higher sample rate. Also, the resolution for backscatter is decreased due to the larger volume of influence after striking the sample surface, Figure 57.

With suitable modification of the electronics, the SEM is capable of performing a chemical analysis of a sample. When the primary electron beam strikes the surface at a point, X-rays characteristic of its elemental nature in the region of penetration are emitted. The energy of an emitted X-ray photon is converted into an electronic pulse in a lithium drifted silicon crystal detector. The pulse is proportional to the energy of an incident X-ray. This type of detector is termed an energy dispersive (ED) detector. The pulse is amplified and fed into a multichannel analyzer where it is stored according to its energy in the proper channel. The resulting energy spectrum is usually displayed on a CRT. The energy spectrum is compared to reference X-ray tables to determine the elemental composition of the material.

A limitation of the energy dispersive detector is the low resolution (~150 to 200 ev). The limit of detection is due to the energy of the X-ray; too low an energy is not detected. The lowest atomic number that can be detected is 11 (sodium). The spatial resolution of the X-ray generation is also fairly poor since the region of influence is quite large, Figure 57.

APPENDIX C

PROPOSED MECHANISMS OF DAMAGE

While cavitation damage has been a problem of major concern, the actual mechanism of the damage has been difficult to determine. Most investigators feel that the damage is mainly the result of a mechanical process with additional effects due to interrelation between the mechanical and corrosive aspects of the problem. Even if the damage is considered to be caused by purely mechanical means, there are still a number of mechanical mechanisms that are possible. The following is a summary of both the mechanical and other mechanisms that have been proposed to explain cavitation damage.

Mechanical Attack

Spherical Collapse - Figure 58-1. One of the first works dealing with the mechanism of the damage produced by cavitation was due to Rayleigh (24). He considered the collapse of an empty void in water and the pressures produced in the surrounding fluid. His findings showed that for this particular case, high pressures are developed in the surrounding fluid as the size of the collapsing cavity approaches zero.

In a later study, Hickling and Plesset (25) considered the collapse and rebound of a bubble containing some noncondensable gas. They postulated that the shock wave produced by the collapse and rebound was sufficient to possibly damage a nearby boundary. Since the attenuation of the wave goes like $1/r_b$, where r_b is the radial distance from a bubble center of collapse, the bubble must be fairly close to

the boundary for the damage to occur. It has been shown though that a spherical bubble is inherently unstable during collapse (26) and, in the vicinity of a wall, the surface of the bubble away from the wall indents and moves towards the wall (27). The full force of the collapse would not be obtained due to the nonsymmetrical collapse.

Nonsymmetrical Collapse - Figure 58-2. Kornfeld and Suvorov (28) postulated that the velocity of this indentation of the nonsymmetrically collapsing cavity could be great enough to damage the boundary. The first major work that showed conclusively that symmetry was not maintained near a boundary was that by Naudé and Ellis (29). Both experimental and theoretical results were obtained which showed that the indentation or jet did in fact strike the boundary. The impact of the jet was "observed" indirectly through the use of a photoelastic boundary to indicate the applied stresses. Their theoretical analysis employed a perturbation technique of an initially non-hemispherical, axially symmetric bubble in contact with the wall. High speed motion pictures of individual collapsing cavities show good agreement between the theoretical and experimental.

The single cavities were produced by the generation of a spark discharge in water. A cavity would grow to a point where equilibrium is reached. The collapse of the cavity is then studied photographically. By altering the distance of the discharge from the wall, the initial perturbations from the hemispherical shape of a cavity in contact with the boundary can be changed.

The boundary was made of a photoelastic material, CR-39, so the applied stresses could be observed. The jet itself was not visible but

estimations of the jet velocity ranged from 91 to 1021 m/sec for various bubbles. These values are considered high enough to damage even the most durable materials. In a later paper, Benjamin and Ellis (30) experimentally produced large vaporous cavities under a reduced pressure. The jet was observed in this case with its velocity being approximately 35 m/sec. If scaled to atmospheric pressure, the speed would be on the order of 180 m/sec. It must be emphasized that if the bubble is too far from the boundary, either the perturbation to the bubble is very small or the jet is arrested by the fluid between the cavity and the wall or both. This would decrease the damage capability substantially.

Final Toroidal Collapse - Figure 58-3. After the Naudé and Ellis paper, there was little doubt that the nonsymmetrical collapse of a cavitation bubble had the potential for creating damage. It was mentioned that no quantitative information was obtained with relation to the jet impact pressure. In a later paper, Shutler and Mesler (31) dispute the claim that the jet has much potential for damage. Since there was experimental evidence of damage as the result of the nonsymmetrical collapse, they reasoned that the final collapse of the torus form could produce a pressure pulse upon rebound capable of damaging the boundary.

After the jet has either struck the other side of the cavity or the boundary, the collapse of the cavity is not finalized, but the cavity motion continues to a point where the minimum volume is reached. Most authors do not consider the collapse past the time when the jet strikes the boundary. At this point of minimum volume, the cavity is in the

form of a torus. The cavity will then rebound due to noncondensable gas in the cavity and send out a pressure wave.

To substantiate their reasoning, it was shown experimentally that in some instances, the pressure wave emanating from the toroidal collapse and subsequent rebound may be more destructive than the initial jet impingement. Tests were conducted using a spark generating bubble apparatus similar to that used by Naudé and Ellis for obtaining single cavities.

Bubbles with various perturbations were observed photographically during collapse and rebound. The actual shape of the cavities conformed to the theories for nonsymmetrical collapse. Remarkable photographs of the collapse were taken showing the jet moving through the bubble. The experimentation was carried a step further by photographing the collapse of the torus and the subsequent rebound of the cavity.

It was observed that the damage to the boundary did not occur along the axis of symmetry of the bubble, but along a ring about the axis. The damage was in the form of an annular indentation in the case of indium as the test material. When aluminum was used (a slightly harder material), a ring of small pits was observed.

An explanation for these findings was that, if the jet mechanism was predominant, a pit would be formed along the axis of symmetry. Just the opposite was observed though, with the damage occurring away from the axis of symmetry. This was felt to be due to the final collapse of the torus after the jet had already hit the surface. The collapse and subsequent rebound sent out a pressure wave of high enough intensity to damage the surface.

In the paper by Benjamin and Ellis (30), this theory is discounted.

They state,

In particular, it seems that the bubbles observed were in a general way less vigorous than those in the previous experiments, probably because the sparks producing them were made by discharging a condenser at considerably lower voltage and so had longer duration for the same total expenditure of energy.

Therefore, the bubbles were not representative of natural cavitation bubbles. On the other hand, Shutler and Mesler present their viewpoint on the subject of the jet potential for damage.

We have seen here that the rebound bubble can account for the size of the pit relative to the minimum base diameter of the bubble. Neither the jet nor the indented top was visible in the pictures of Naudé, so the estimated jet velocities may certainly be open to question, especially in the light of the inconsistent correlation of velocity and damage severity. The pressure pulse measured at minimum volume was apparently assumed to be in the form of a pancake rather than a torus.

Mechanical Mechanism of Damage: Closure

It has been observed that cavitation damage is a very selective process (3) with very few of the bubbles in a cavitating system causing damage. All three of the aforementioned theories of damage mechanism will only apply if the cavity collapse is within a narrow region with respect to the boundary. Only a small percentage of the cavities in the flow then are within this narrow region. Thus, all of these theories may have some merit. The mechanism most widely accepted as the main contributor to damage is that of the jet formation. It should be emphasized that there is the possibility that, in some instances, the spherical or toriodal collapse modes may also be a significant factor in cavitation damage. It has been suggested that both collapse

modes can have a bearing on the fatigue failure of certain materials (32).

Other Proposed Mechanisms of Damage

Thermogalvanic Postulates. It has been postulated that electro-chemical attacks associated with high temperatures may be responsible for some cavitation erosion. The high temperatures may be generated in either of two ways. First, by the compression of noncondensable gas during the collapse of a cavity, or second, by the high rates of stressing of the boundary associated with the collapse of a bubble near the surface. Of these two, the latter is most widely accepted due to heat transfer problems to the boundary because of the high heat capacity of water in the first case. Taylor and Quinney (33) also have stated that 85% or more of the work during the deformation of a solid by the slip process is converted into heat.

This local heating creates a temperature gradient and causes a current flow in a conducting medium due to the thermoelectric effect. Electrolytic corrosion may then occur. Krenn, Foltyn and Mechleba (34) all have proposed that this mechanism may be present in some cavitating systems.

Stress-Induced Galvanic Effects. Along the same line as the thermogalvanic postulate is the possibility of stress-induced galvanic effects. The localized deformation of a crystalline material increases the emf. of the deformed crystals by altering their internal energy. These localized high stress points become points of increased attack by corrosive elements. This mechanism has been put forward by Petracchi (35).

Protective Film Rupture. An oxide film forms on many materials as a protection against corrosion. A rupture of this film causes a localized corrosion attack at the point of rupture. It has been suggested by Ffield, Mosher and O'Neil (36) that the collapse of cavitation bubbles adjacent to a surface can rupture this film and cause the increased corrosion.

APPENDIX D

CALCULATION OF DAMAGE RATE FOR HIGH VELOCITY TESTS

As mentioned previously, an adjustment in the recorded pitting density (pits/cm²) was made for the high velocity tests. This was necessary because the accumulated damage during the velocity transition period when the velocity was increasing could constitute a significant percentage of the total damage. There was cavitation on the models during the latter portion of the velocity transition period before stable conditions were reached. The time for which a test model sustained damage during the transition period was on the order of a few seconds. For tests conducted at velocities greater than 44 m/sec, the steady state test duration was less than one minute. The minimum steady state test duration was 5.0 seconds at the maximum test velocity namely 59.3 m/sec. Therefore, the accumulation of damage during the transition period could make up a significant percentage of the total damage for these tests.

The procedure for correcting the pitting density consisted of the following four steps:

1. The tunnel velocity was plotted as a function of time for the velocity transition period.
2. Estimations of the damage rates for the given transient velocities from Step 1 were made.
3. The percentage of pits formed during the transition period was then calculated.

4. The percentage of pits formed during the transition period was then subtracted from the measured pitting density for a test model. This gave the corrected pitting density for those pits formed during steady state conditions.

Details concerning these four basic steps are given in the following sections.

Step 1

A movie was taken of a stopwatch and the digital voltmeter display of the tunnel pressures for the two highest velocity ranges. One movie was taken for a test velocity of approximately 50 m/sec and the second at 59 m/sec. From each movie, a plot was obtained of tunnel velocity during the transition period as a function of time. This was obtained from the film of the tunnel pressure readings shown on the voltmeter display. The plot for a test velocity of 59 m/sec is shown in Figure 59 together with sample calculations for the damage rate correction.

Step 2

For each velocity in the transition period, there is a corresponding damage rate. The damage rate also depends upon the length of the cavity. During the velocity transition period, the tunnel pressure was held constant. As the velocity increased, a cavity grew on the model until the desired cavity length was reached at stable conditions. As shown previously in this investigation, the damage rate decreases substantially for cavities shorter than a dimensionless cavity length (L/D) of 2.0. The time increment from the point where L/D was 2.0 until stable conditions were reached was recorded. This is the time during the transition period in which a significant amount of cavitation pitting occurred.

The velocity transition period was divided into one-second time intervals. An estimated damage rate for each time interval was calculated from the velocity at the midpoint of each interval. The rate was assumed constant for each time interval. The rates were obtained by extending the damage rate versus velocity curve obtained in the course of the investigation. The time in which there is significant damage is the number of one-second intervals in the velocity transition period when $L/D \geq 2.0$

Step 3

The percentage of pits formed during the transition period was determined in this step. The number of pits per unit area in each time interval is the damage rate multiplied by the time interval, i.e., one second. The pitting density during the transition period is the sum for all intervals. The pitting density for the steady state is the estimated steady state damage rate multiplied by the test duration. The total pitting density (P_T) would be the sum of the pitting density in the transition period (P_{TR}) and the pitting density in the steady state period (P_{SS}). The fraction of the total pits formed during the transition period is $\frac{P_{TR}}{P_T}$. It must be mentioned again that these pitting densities were obtained from estimated damage rates. The use of these estimated values in correcting the pitting density for a test model is as follows.

Step 4

The ratio $\frac{P_{TR}}{P_T}$ can be applied in the calculation of the damage rate for a test model. The ratio is multiplied by the recorded pitting density of a model. This gives the number of pits per unit area formed during the transition period. This number is subtracted from

the recorded pitting density. The result is the pitting density formed during the steady state period for the test model. This density is divided by the steady state test duration to determine the damage rate. A similar procedure is followed for computing the corrected pitting rate in the maximum damage zone (PRMD) and the total pitting rate (TPR).

As stated previously, the estimated damage rates were obtained from an extension of the damage rate versus velocity plot. If the sixth power damage rate law did not hold for the high velocities, these estimated damage rates would be in error. It was found that the corrected damage rate was close to the estimated value. This shows that the power law does hold for these higher velocities and that the assumptions were correct.

APPENDIX E

THE HIGH SPEED PHOTOGRAPHIC SYSTEM

For the investigation of the cavity dynamics, a Redlake Hycam camera was used together with an EG and G Type 501 high speed stroboscope, Figure 60. The Redlake Hycam camera is a 16 mm high speed rotating prism camera capable of 11,000 full or 44,000 quarter frames per second. The EG and G strobe unit produces high intensity flashes at rates up to 6000 per second with a minimum flash duration of 1.2 microseconds. The light output is a function of the strobe capacitor setting. The guide factor for the FX-2 and FX-3 bulbs used in this investigation is given by the following relationship:

$$D_S A = \sqrt{\text{CPS } M \text{ s/c}} \quad , \quad (25)$$

where

D_S - the lamp-subject distance

A - the camera lens aperture

CPS - lamp output in candela - seconds

M - reflector factor

s - ASA of film

c - a constant (15 to 25 if D is in feet)

To increase the efficiency of the lighting for any particular setup, two lamps and reflectors are provided, a cylindrical reflector

used with the FX-3 bulb and a parabolic reflector used with the FX-2. The cylindrical reflector has a reflector factor M of 1.5 while the reflector factor for the parabolic varies from 32 for wide angle use to 75 for narrow lighting angles.

There were two basic configurations utilized for this study, backlighting and reflected lighting, Figure 61. With backlighting, the cylindrical reflector was used. Although it has a very low reflector factor, which means it does not make most efficient use of the light, its long narrow shape conformed to that of the cavitation model and provided an even illumination of the surface. Reflected lighting was used for detailed close-ups of the cavity. The parabolic reflector was used and adjusted for a narrow lighting angle to provide sufficient illumination.

In cavity dynamics where it is desired to measure the frequency of pulsation, extreme detail of the flow was not required. The field of view in this case was approximately 8 cm. A 28 mm Pentax lens with a 2 mm extension tube provided the desired magnification while still maintaining a relatively short light to camera distance (approximately 0.5 m). Since the Hycam has a C mount thread for the lens, a Pentax to C mount adapter was used. A backlighting technique was used and with a strobe capacitor setting of 0.02 μ F, the lens aperture was set between f 5.8 and 8 (with 400 ASA film).

Under normal operation, considerable film is wasted during the period of acceleration to constant film speed. To minimize this problem the camera operation and the strobe were synchronized so that only the last 18.3 m of a 38.1 m roll would be exposed. The camera was brought up to 5000 frames per second and the light flashed for

AD-A049 766

PENNSYLVANIA STATE UNIV UNIVERSITY PARK APPLIED RESE--ETC F/6 20/4
SCALING OF CAVITATION DAMAGE.(U)

FEB 77 D R STINEBRING

N00017-73-C-1418

UNCLASSIFIED

TM-76-51

NL

2 OF 3

AD
A049766



0.42 seconds. This would expose only the last half of the roll of film. The film was then rethreaded front to back through the camera and another sequence photographed. In this case, the other half of the film was then exposed. Thus, nearly the entire length of film was utilized, decreasing the film requirements by a factor of two.

In some sequences, it was desired to have a larger magnification for a closer look at the cycling process. A 50 mm Pentax lens with a 5 mm extension provided the added magnification while keeping the proper light-to-camera distance (0.5 m). The field of view in these sequences was about 4 cm. Backlighting was used with the same capacitor setting, f stop, and camera-light run times as for the previous sequences.

In four runs, reflected lighting was used with an even greater magnification than the previous runs. A 55 mm Nikon lens with a Nikon to Pentax adapter, a Pentax to C mount adapter and a 3 mm extension ring was used in this case. The maximum field of view was about 2 cm. The light-to-subject distance along with the camera-to-subject distance was about 0.25 m. The parabolic reflector adjusted for a narrow lighting angle was used for these sequences. The camera aperture was set at f 8 to provide a suitable depth of field and sufficient exposure was attained by the use of 3200 ASA film and a strobe capacitor setting of 0.02 μ F.

Two types of film were used in the high speed photographic study. The first was Kodak 2479 RAR film with an ASA of 400. This is a medium-fine grain film with high speed and was used for all backlighting shots. For reflected lighting, Kodak 2484 Pan Film Estar AH Base with

an ASA of 3200 (when developed in Kodak D-19 developed at 35° C for 1 minute) was used.

The film was processed at the Garfield Thomas Water Tunnel with a Fairchild Minirapid 16 mm film processor. Although the quality of development was not as good as could be expected if processed commercially, the convenience more than compensated for this. A sequence could be shot, developed, and any changes made in the photographic setup in less than one hour.

A process for developing the two types of film in the Fairchild processor was conceived. Kodak D-19 developer at approximately 35° C with a developing speed of about 0.3 m/sec in the processor produced the best results. Kodak's Rapid Fixer and Hypo Cleaning Agent were used in the next two baths, respectively, with a one-minute water wash before drying. The 2484 film had a tendency to fog during the development. After development, the film was viewed and analyzed with the help of a Vanguard Motion Analyzer with a 16 mm head.

APPENDIX F

CORROSION OF ALUMINUM

Pure aluminum is quite corrosion resistant due to a thin but strong oxide layer. When corrosion does occur, it is usually in the form of a pitting of the surface. The pitting corrosion occurs when there is a local breakdown of the protective oxide film, with the attack proceeding locally and at accelerated rates.

According to the oxide film theory, the corrosion of aluminum occurs as follows. Chloride ions penetrate the oxide film through local defects causing a breakdown of passivity. Small anodic regions are formed surrounded by large areas of more passive metal creating a galvanic cell. Oxygen is reduced in these passive areas while the products of corrosion, usually hydroxides, are formed at the anode with a passage of current between the two areas. These corrosion products are then usually precipitated out of solution and deposited on the surface. Pit growth continues at accelerated rates at the anodic region while the surrounding area is protected by cathodic protection. The more dense crystallographic planes are more resistant to the corrosion. This results in a pattern of corrosion which makes visual the cubic structure of the aluminum. For corrosion to occur, copper, chloride ions, oxygen and calcium bicarbonate must all be present in various amounts.

The rate of attack can be affected by many means. The relative areas of the anodic and cathodic regions can affect the corrosion. If the area of the cathode is very large, oxygen reduction will be greater, causing a greater current flow and increased attack at the anode.

Contact of the aluminum with a more noble metal can also increase the attack.

The breakdown of the oxide film can be caused by many factors. One of these is the purity of the aluminum. Resistance is reduced when aluminum is in combination with more electropositive metals such as iron and copper (this is the case for 1100 aluminum). These metals disrupt the oxide layer and cause increased attack in the surrounding areas. The pH of the surrounding fluid also affects the corrosion rate. The oxide film of aluminum is usually stable in the range of a pH from 4.5 to 8.5. Outside of this range, the film can be destroyed and attack can proceed easily. The oxide layer may also be disrupted by mechanical means such as cavitation bubble collapse. Cavitation can also initiate corrosion in another way. After a cavitation bubble causes an indentation in the surface, the metal in that area is stressed. These stressed areas are anodic to the surrounding area stimulating attack. Although there is thought to be a strong interaction between the corrosion of some metals and cavitation, the exact mechanism of the attack is not known for certain.

TABLE I
TEST DATA FOR PHASE I MODELS

Model	Velocity (m/sec)	L/D	Test Duration (min)	Damage Rate Max. Damage Zone (pits/cm ² /sec)	Overall Damage Rate on Model (pits/cm ² /sec)
1	21.3	2.0	30	5.29	2.67
2	21.3	1.2	60		
3	21.3	2.0	30		
4	21.3	2.0	60		
5	21.3	2.0	15	5.22	
6	18.3	2.0	30		
7	19.8	1.0	45		
8	18.3	2.6	30		

TABLE II

TEST DATA FOR PHASE II AND III TESTS

Model Number	Velocity (m/sec)	L/D	Pitting Density In The Maximum Damage Zone (pits/cm ²)	Damage Rate In The Maximum Damage Zone DRMD (pits/cm ² /sec)	Pitting Rate Maximum Damage Zone PRMD (pits/sec)	Total Pitting Rate TPR (pits/sec)	Air Content (ppm)	Test Duration (minutes)	Test Phase
10	38.22	1	----	----	----	----	16.5	10	II
11	23.26	1	----	----	----	----	----	45	II
12	43.59	1	----	----	----	----	16.7	3	II
13	30.87	1	----	----	----	----	19.3	20	II
15	30.60	2	3294	2.74	4.17	5.16	19.9	20	II
16	38.31	2	6066	5.05	6.66	7.29	17.3	20	II
17	42.82	2	2973	16.43	21.81	22.03	20.0	3	II
18	30.02	3	2497	2.77	5.07	6.24	19.0	15	II
19	38.19	3	4140	6.90	13.29	14.53	18.5	10	II
20	22.95	3	1102	0.31	0.41	0.54	20.3	60	II
21	42.64	3	2518	20.93	27.69	31.57	19.7	2	II
22	30.11	4	2546	2.83	6.03	6.62	18.0	15	II
25	42.89	4	2206	18.38	33.58	37.95	16.7	2	II
26	23.29	2	1273	0.42	0.29	0.73	20.6	50	II
27	37.37	1.75	7033	11.72	11.88	13.45	10.3	10	III
29	37.22	1.50	4368	4.85	5.40	5.71	7.7	15	III
30	37.37	1	409	0.27	0.26	0.26	7.9	25	III
31	29.87	1	1453	0.97	0.98	1.31	7.5	25	III
32	23.16	2	1439	0.80	1.71	2.31	10.7	30	III

TABLE II (CONT.)

Model Number	Velocity (m/sec)	L/D	Pitting Density In The Maximum Damage Zone (pits/cm ²)	Damage Rate In The Maximum Damage Zone DRMD (pits/cm ² /sec)	Pitting Rate In The Maximum Damage Zone PRMD (pits/sec)	Total Pitting Rate TPR (pits/sec)	Air Content (ppm)	Test Duration (minutes)	Test Phase
33	23.16	2	4027	2.23	4.30	6.13	8.1	30	III
34	23.20	2	2478	1.38	3.36	4.79	7.6	30	III
35	37.12	2	3396	10.57	18.22	23.56	11.7	5.5	III
37	37.98	3	4033	11.21	30.53	37.11	9.5	6	III
38	30.11	3	2712	2.98	12.21	14.98	9.9	9	III
39	43.65	3	2832	31.47	82.86	120.60	13.4	1.5	III
41	49.26	3	3881	126.00	218.60	280.40	8.3	0.47	III
42	38.22	4	6353	10.59	25.92	30.75	9.9	10	III
43	43.43	4	4035	44.80	154.70	185.40	9.8	1.5	III
44	29.84	3	4712	4.62	11.68	13.94	11.2	17	III
45	30.51	4	4267	3.56	12.61	14.38	8.4	20	III
46	49.98	4	4753	83.90	255.20	309.60	8.5	0.88	III
51	14.87	2	1903	0.15	0.35	0.39	6.7	210	III
52	36.82	3	5390	17.96	40.05	48.17	7.1	5	III
55	22.52	3	3996	1.90	3.08	3.87	7.6	35	III
57	36.45	6	4263	4.74	19.20	20.01	8.0	15	III
82	51.33	2	3746	124.80	151.80	189.00	9.1	0.5	III
83	59.28	3	2105	272.00	606.30	769.00	11.5	0.08	III

TABLE III

DYNAMIC HARDNESS TEST RESULTS

Indenter Drop Height h_1 (m)	Rebound Height h_2 (m)	Pit Diameter D_H (mm)	Apparent Pit Volume, $V_A, \times 10^{-3}$ (mm^3)	Dynamic Hardness, $H_D, \left(\frac{\text{m}^2 \text{kg}}{\text{sec}^2}\right)$ $\text{mm}^3, \text{J/mm}^3$	Mean Dynamic Pressure, P_D , (kg/mm^2)	Approximate Time of Pit Formation, t, $\times 10^{-6}(\text{sec})$
0.200	0.0335	0.355	0.490	0.469	47.8	8.1
0.200	0.0340	0.355	0.490	0.468	47.8	8.1
0.200	0.0350	0.360	0.518	0.442	45.1	8.4
0.200	0.0325	0.355	0.490	0.470	47.1	8.1
0.300	0.0435	0.390	0.714	0.487	49.7	8.0
0.300	0.0440	0.395	0.715	0.462	47.2	8.2
0.300	0.0415	0.390	0.714	0.488	49.8	8.0
0.300	0.0360	0.390	0.714	0.492	50.2	7.9
0.300	0.0440	0.380	0.643	0.540	55.1	7.6
0.300	0.0430	0.390	0.714	0.487	49.7	8.0
0.300	0.0410	0.395	0.751	0.464	47.4	8.2
0.300	0.0445	0.390	0.714	0.486	49.6	8.0
0.300	0.0420	0.390	0.714	0.488	49.8	8.0
0.300	0.0460	0.385	0.678	0.511	52.1	7.8
0.300	0.0460	0.390	0.714	0.485	49.9	8.0
0.400	0.0440	0.420	0.960	0.489	49.9	7.9
0.400	0.0480	0.410	0.872	0.537	54.8	7.6
0.500	0.0510	0.435	1.105	0.533	54.4	7.6
1.000	0.1150	0.520	2.257	0.519	53.0	7.7
1.000	0.1100	0.520	2.257	0.520	53.1	7.7
1.000	0.1170	0.520	2.257	0.519	52.9	7.7

Ball Diameter - 3.180 mm
Ball Mass - 0.125 gm

TABLE III (CONT.)

Indenter Drop Height h_1 (m)	Rebound Height h_2 (m)	Pit Diameter D_H (mm)	Apparent Pit Volume, $V_A, \times 10^{-3}$ (mm^3)	Dynamic Hardness, $H_D, \left(\frac{\text{m}^2 \text{kg}}{\text{sec}^2}\right)$ $\text{mm}^3, \text{J/mm}^3$	Mean Dynamic Pressure, $P_D,$ (kg/mm^2)	Approximate Time of Pit Formation, t, $\times 10^{-6}$ (sec)
Ball Diameter - 5.332 mm	0.300	0.660	3.494	0.500	51.1	7.9
Ball Mass - 0.625	0.300	0.660	3.494	0.501	51.1	7.9
	0.200	0.026	2.084	0.559	57.1	7.4
	0.200	0.022	2.084	0.564	57.5	7.4

Average $H_D = 0.499$ (0.5) J/mm^3

Average Time of Pit Formation = 7.9×10^{-6} sec

TABLE IV

PIT DIAMETERS, DEPTHS, DIAMETER-TO-DEPTH RATIOS, AND
 VOLUMES FOR A VELOCITY OF 30.1 m/sec AND L/D=3
 (MODEL 38)

Diameter (mm)	Depth $\times 10^{-3}$ (mm)	Diameter/Depth	Volume $\times 10^{-6}$ (mm ³)	Lighting* Angle (radians)
0.08	2.8	28.9	7.0	0.14
0.03	1.8	17.0	0.6	0.23
0.02	0.85	23.4	0.1	0.17
0.06	2.0	29.6	2.9	0.13
0.025	1.4	17.8	0.3	0.22
0.02	1.3	15.6	0.2	0.25
0.02	1.3	15.6	0.2	0.25
0.03	1.3	23.1	0.5	0.17
0.05	2.5	20.3	2.4	0.20
0.03	1.2	25.1	0.4	0.16
0.05	2.6	19.3	2.6	0.21
0.03	1.7	17.3	0.6	0.23
0.02	1.8	11.1	0.3	0.35
0.02	1.8	10.9	0.3	0.36
0.04	2.9	13.8	1.8	0.29
0.09	6.3	14.3	20.2	0.28
0.03	2.0	15.2	0.7	0.26
0.03	2.0	15.2	0.7	0.26
0.08	3.3	24.3	8.3	0.16
0.03	1.3	23.4	0.5	0.18
0.02	1.0	19.9	0.2	0.20
0.04	2.7	15.1	1.7	0.26
0.03	2.1	14.3	0.7	0.28
0.03	1.4	21.5	0.5	0.19
0.08	3.0	27.1	7.4	0.15
0.09	3.3	27.1	10.6	0.15
0.02	1.3	15.4	0.2	0.26
0.02	1.4	13.9	0.2	0.29
0.04	2.0	19.7	1.3	0.20
0.035	2.7	12.8	1.3	0.31
0.02	1.3	15.8	0.2	0.25
0.02	1.2	16.9	0.2	0.24
0.11	5.9	18.7	28.0	0.21
0.04	2.4	16.6	1.5	0.24
0.04	1.5	27.0	0.9	0.15
0.03	1.3	23.2	0.5	0.17

*The lighting angle was used in the calculation of the pit volumes
 (Section 2.8).

TABLE IV (CONT.)

Diameter (mm)	Depth $\times 10^{-3}$ (mm)	Diameter/Depth	Volume $\times 10^{-6}$ (mm ³)	Lighting* Angle (radians)
0.02	1.2	16.4	0.2	0.24
0.05	2.3	21.5	2.3	0.19
0.08	6.6	12.1	16.8	0.33
0.03	1.6	18.4	0.6	0.22
0.06	2.3	25.8	3.3	0.15
0.05	2.4	21.1	2.3	0.19
0.04	2.1	19.0	1.3	0.21
0.025	1.9	13.4	0.5	0.30
0.04	1.9	21.5	1.2	0.19
0.03	1.5	20.0	0.5	0.20
0.06	2.3	25.8	3.3	0.15
0.03	1.8	16.8	0.6	0.24
0.07	2.8	24.7	5.5	0.16
0.02	1.0	19.7	0.2	0.20
0.06	4.0	15.1	5.6	0.26
0.05	3.6	13.7	3.6	0.29
0.04	1.8	22.3	1.1	0.18
0.03	1.2	24.7	0.4	0.16
0.05	2.8	17.6	2.8	0.23
0.02	1.0	20.0	0.2	0.20
0.06	4.5	13.4	6.4	0.30
0.03	1.4	20.7	0.5	0.19
0.04	2.6	15.1	1.7	0.26

Average Diameter - 0.04 mm, Maximum Diameter - 0.11 mm,
Minimum Diameter - 0.01 mm

Average Depth - 2.2×10^{-3} mm, Maximum Depth - 6.6×10^{-3} mm,
Minimum Depth - 8.5×10^{-4} mm

Average Diameter/Depth - 19.0, Maximum Diameter/Depth - 29.6,
Minimum Diameter/Depth - 10.9

Average Volume - 2.8×10^{-6} mm³, Maximum Volume - 2.8×10^{-5} mm³,
Minimum Volume - 1.3×10^{-7} mm³

*The lighting angle was used in the calculation of the pit volumes
(Section 2.8).

TABLE V

PIT DIAMETERS, DEPTHS, DIAMETER-TO-DEPTH RATIOS, AND
 VOLUMES FOR A VELOCITY OF 38 m/sec AND L/D=3
 (MODEL 37)

Diameter (mm)	Depth $\times 10^{-3}$ (mm)	Diameter/Depth	Volume $\times 10^{-6}$ (mm ³)	Lighting Angle (radians)
0.05	7.1	7.0	7.2	0.55
0.07	5.3	13.3	10.2	0.30
0.05	3.3	15.0	3.3	0.27
0.07	8.3	8.5	16.2	0.46
0.06	5.6	10.8	8.0	0.37
0.03	1.7	17.7	0.6	0.22
0.05	6.5	7.7	6.5	0.51
0.04	2.7	14.6	1.7	0.27
0.03	4.9	6.1	1.8	0.63
0.05	2.4	20.5	2.4	0.19
0.03	4.7	6.4	1.7	0.60
0.02	3.0	6.7	0.5	0.58
0.04	6.7	6.0	4.3	0.64
0.07	6.5	10.8	12.7	0.37
0.04	3.4	11.8	2.1	0.33
0.05	6.9	7.3	6.9	0.53
0.03	1.7	17.6	0.6	0.23
0.04	3.3	12.1	2.1	0.33
0.10	9.3	10.8	36.7	0.37
0.02	2.7	7.4	0.4	0.53
0.05	5.1	9.8	5.1	0.40
0.06	8.0	7.5	11.6	0.52
0.02	1.7	12.0	0.3	0.33
0.13	8.7	14.9	58.3	0.27
0.10	10.3	9.7	41.1	0.41
0.07	8.7	8.0	17.2	0.49
0.05	4.1	12.2	4.1	0.33
0.02	1.2	17.0	0.2	0.23
0.04	4.7	8.5	3.0	0.46
0.03	4.7	6.4	1.7	0.60
0.09	11.2	8.0	36.4	0.49
0.07	7.8	9.0	15.3	0.44
0.03	1.8	16.4	0.7	0.24
0.06	7.2	8.3	10.4	0.47

TABLE V (CONT.)

Diameter (mm)	Depth $\times 10^{-3}$ (mm)	Diameter/Depth	Volume $\times 10^{-6}$ (mm ³)	Lighting Angle (radians)
0.05	8.0	6.3	8.1	0.62
0.02	1.2	16.1	0.2	0.25
0.04	5.4	7.4	3.5	0.53

Average Diameter - 0.05 mm, Maximum Diameter - 0.13 mm,
Minimum Diameter - 0.02 mm

Average Depth - 5.3×10^{-3} mm, Maximum Depth - 1.1×10^{-2} mm,
Minimum Diameter - 1.2×10^{-3}

Average Diameter/Depth - 10.7, Maximum Diameter/Depth - 20.4,
Minimum Diameter/Depth - 6.0

Average Volume - 9.3×10^{-6} mm³, Maximum Volume - 5.8×10^{-5} mm³,
Minimum Volume - 2.0×10^{-7} mm³

TABLE VI

PIT DIAMETERS, DEPTHS, DIAMETER-TO-DEPTH RATIOS, AND
 VOLUMES FOR A VELOCITY OF 49.3 m/sec AND L/D=3
 (MODEL 41)

Diameter (mm)	Depth $\times 10^{-3}$ (mm)	Diameter/Depth	Volume $\times 10^{-6}$ (mm ³)	Lighting Angle (radians)
0.10	14.3	7.0	57.7	0.56
0.10	5.7	17.6	22.3	0.23
0.08	7.5	10.6	19.1	0.37
0.05	2.8	17.7	2.8	0.22
0.05	5.4	9.2	5.4	0.43
0.05	4.8	10.5	4.7	0.38
0.08	6.1	13.1	15.5	0.30
0.10	13.6	7.4	54.6	0.53
0.05	4.6	10.8	4.6	0.37
0.05	5.5	9.1	5.5	0.43
0.02	1.7	12.1	0.3	0.33
0.07	3.7	19.0	7.1	0.21
0.07	4.6	15.4	8.8	0.26
0.07	6.3	11.1	12.2	0.36
0.13	18.2	7.1	124.0	0.55
0.22	28.5	7.7	554.0	0.51
0.04	3.2	12.5	2.0	0.32
0.08	9.0	8.9	23.0	0.44
0.12	13.5	8.9	77.5	0.44
0.05	6.6	7.5	6.7	0.52
0.05	2.2	22.4	2.2	0.18
0.05	4.2	11.9	4.2	0.33
0.07	4.9	14.3	9.5	0.28
0.12	8.5	14.1	48.4	0.28
0.05	3.5	14.5	3.4	0.27
0.04	3.5	11.5	2.2	0.34
0.07	5.9	12.0	11.4	0.33
0.06	6.0	10.1	8.5	0.39
0.11	17.7	6.2	86.6	0.62
0.08	12.8	6.2	33.3	0.62
0.05	2.7	18.7	2.6	0.21
0.06	3.2	18.7	4.6	0.21
0.04	2.5	16.0	1.6	0.25
0.06	6.2	9.7	8.9	0.41
0.05	4.6	11.0	4.5	0.36

TABLE VI (CONT.)

Diameter (mm)	Depth $\times 10^{-3}$ (mm)	Diameter/Depth	Volume $\times 10^{-6}$ (mm ³)	Lighting Angle (radians)
0.09	11.4	7.9	36.9	0.49
0.15	12.4	12.1	110.4	0.33
0.06	5.6	10.6	8.1	0.37

Average Diameter - 0.07 mm, Maximum Diameter - 0.22 mm,
Minimum Diameter - 0.02 mm

Average Depth - 7.4×10^{-3} mm, Maximum Depth - 2.8×10^{-2} ,
Minimum Depth - 1.7×10^{-3}

Average Diameter/Depth - 11.9, Maximum Diameter/Depth - 22.4,
Minimum Diameter/Depth - 6.2

Average Volume - 3.7×10^{-5} mm³, Maximum Volume - 5.5×10^{-4} mm³,
Minimum Volume - 2.6×10^{-7} mm³

TABLE VII
CAVITY CYCLE FREQUENCY DATA

Film Number	Velocity (m/sec)	L/D	Time Of Cycle $\times 10^{-3}(\text{sec})$	Cycle Frequency	Strouhal Number $S = \frac{fD}{V_{\infty}}$	σ
13 p	23.0	3.6	5.82	171.9	0.0478	0.384
13 p	23.0	5.1	-----	-----	-----	0.337
14 p	23.0	4.9	-----	-----	-----	0.342
14 p	23.0	3.6	5.15	194.3	0.0536	0.386
15 p	18.8	4.0	8.49	117.8	0.0397	0.370
15 p	30.5	4.8	6.54	152.9	0.0318	0.345
16 p	23.0	1.9	2.25	444.2	0.1224	0.490
16 p	23.0	4.6	8.39	119.2	0.0328	0.349
17 p	23.0	2.0	2.31	433.3	0.1194	0.481
17 p	15.1	4.1	10.40	96.9	0.0407	0.365
18 p	30.5	3.8	4.88	205.0	0.0427	0.376
18 p	15.1	3.8	8.20	122.1	0.0513	0.377

TABLE VIII

TEST DATA FOR INVESTIGATIONS OF
CAVITATION DAMAGE IN THE INCUBATION ZONE

	Velocity (m/sec)	Damage Rate (pits/cm ² /sec)	Air Content (ppm)	Damage Rate Corrected To* An Air Content Of 8.9 ppm
Knapp (1955)	18.0	----	----	----
	19.2	0.62	----	0.62
5.08 cm Diameter	21.6	1.86	----	1.86
Hemispherical-Nosed Body	23.6	2.10	----	2.10
	27.4	8.20	----	8.20
L/D = 1	30.5	9.30	----	9.30
Hackworth and Arndt (1974)	16.8	0.33	8.0	0.30
	18.3	0.47	8.0	0.42
0.635 High Step-Mismatch	21.3	1.15	8.0	1.03
$\sigma = 0.32$ (L/D ≈ 8)				
Sato et al. (1973)	30.0	10.5	8.9	10.5
	40.0	80	8.9	80
1 cm Diameter	50.0	105	8.9	105
	60.0	650	8.9	650
Hemispherical-Nosed Body	70.0	1000	8.9	1000
L/D = 1				

* The correction utilizes the inverse relationship between the damage rate and air content found from this investigation. The air content of 8.9 ppm corresponds to a value of 0.6 of the saturation value at a temperature of 21 °C (14.8 ppm); this is the air content of the Sato et al. investigation.

TABLE VIII (CONT.)

	Velocity (m/sec)	Damage Rate (pits/cm ² /sec)	Air Content (ppm)	Damage Rate Corrected To An Air Content Of 8.9 ppm*
Stinebring (1976)	23.0	0.31	20.3	0.71
	23.3	0.42	20.6	0.98
0.635 cm Diameter	30.0	2.77	19.0	5.90
	30.1	2.83	18.0	5.70
Zero-Caliber Ogive	30.6	2.74	19.9	6.13
	38.2	6.90	18.5	14.34
	38.3	5.05	17.3	9.80
L/D = 2 to 4	42.6	20.93	19.7	46.33
	42.8	16.43	20.0	36.85
	42.9	18.38	16.7	34.50
	14.9	0.15	6.7	0.11
	22.5	1.90	7.6	1.63
	23.2	0.80	10.7	0.96
	23.2	1.38	7.6	1.18
	23.2	2.23	8.1	2.02
	29.8	4.62	11.2	5.80
	30.1	2.98	9.9	3.29
	30.5	3.56	8.4	3.36
	37.1	10.57	11.7	13.90
	38.0	11.21	9.5	11.95

* The correction utilizes the inverse relationship between the damage rate and air content found from this investigation. The air content of 8.9 ppm corresponds to a value of 0.6 of the saturation value at a temperature of 21 °C (14.8 ppm); this is the air content of the Sato et al. investigation.

TABLE VIII (CONT.)

Stinebring (1976) (cont.)	Velocity (m/sec)	Damage Rate (pits/cm ² /sec)	Air Content (ppm)	Damage Rate Corrected To An Air Content Of 8.9 ppm*
	38.2	10.59	9.9	11.70
	43.4	44.80	9.8	49.30
	43.7	31.47	13.4	47.43
	49.3	126.00	8.3	117.50
	50.0	83.90	8.5	80.10
	51.3	124.80	9.1	127.60
	59.3	272.00	11.5	351.50

*The correction utilizes the inverse relationship between the damage rate and air content found from this investigation. The air content of 8.9 ppm corresponds to a value of 0.6 of the saturation value at a temperature of 21 °C (14.8 ppm); this is the air content of the Sato et al. investigation.

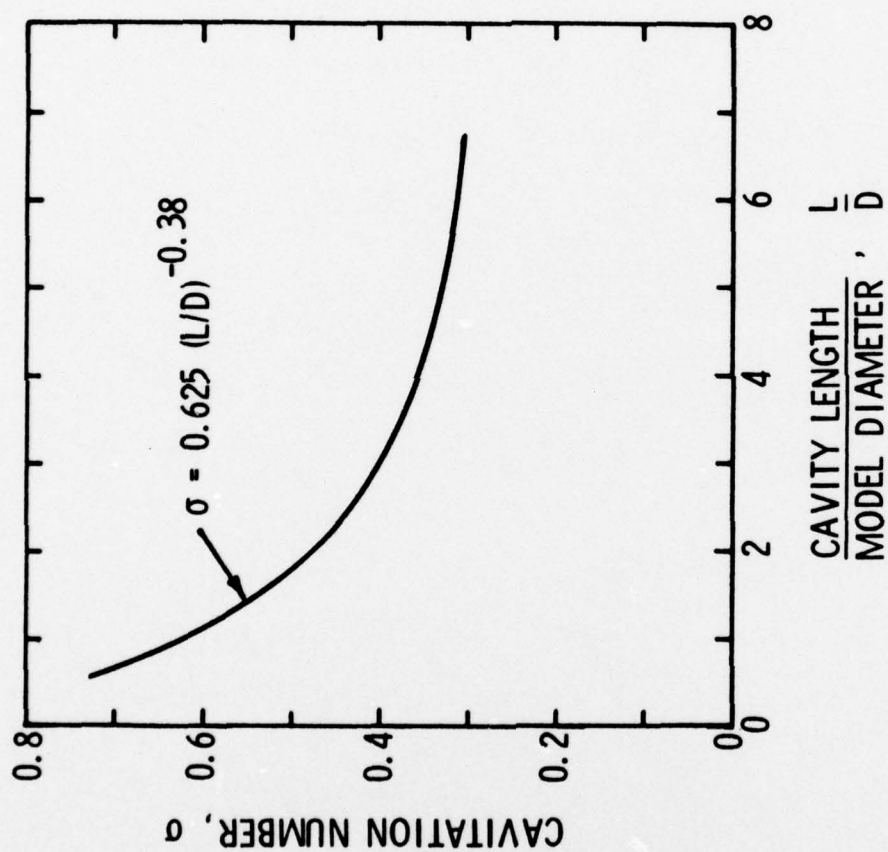


Figure 1 - Cavitation Number Versus Dimensionless Cavity Length for a 0.635 cm Diameter Zero-Caliber Ogive in a 3.8 cm Test Section (Weir, 1975)

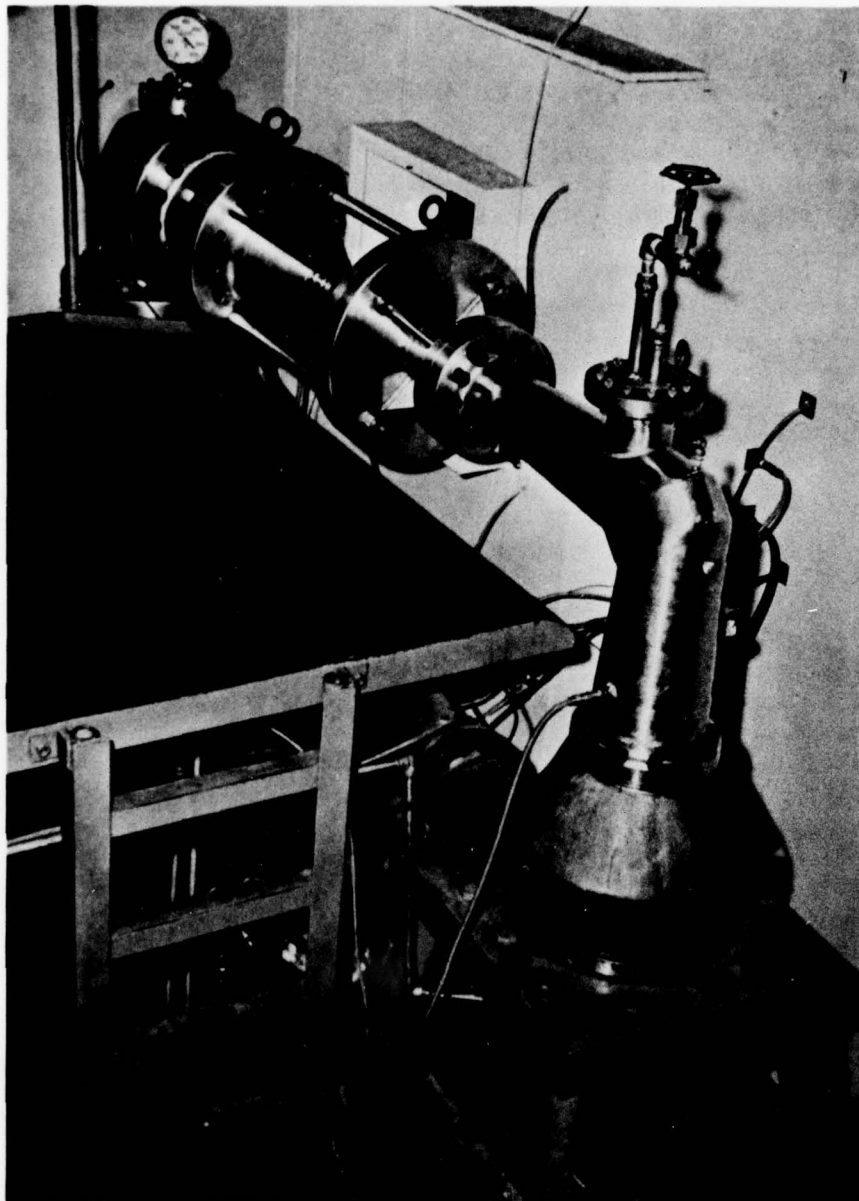


Figure 2 - Photograph of the 3.8 cm Ultra-High-Speed Cavitation Tunnel

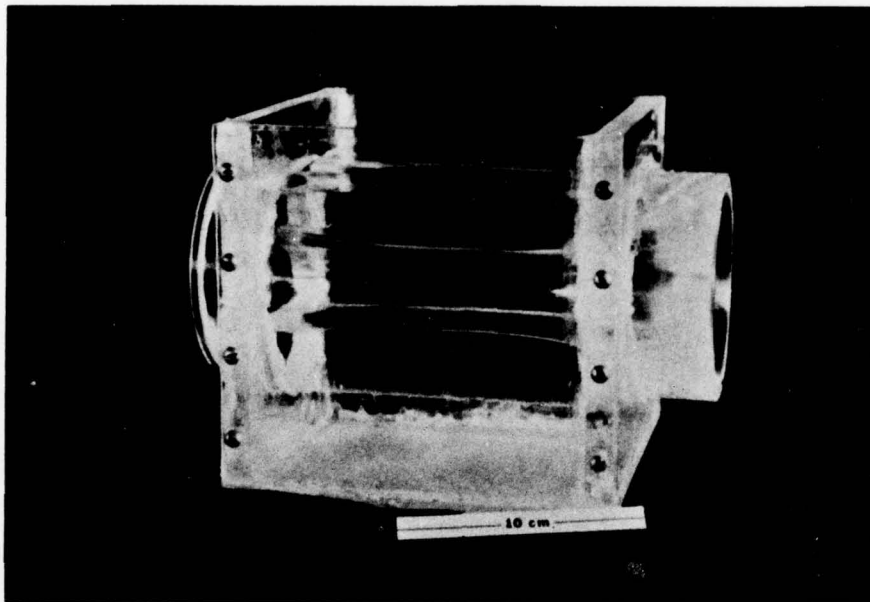


Figure 3 - Photograph of the Plexiglass Test Section for the 3.8 cm Cavitation Tunnel with the Photographic Test Box Used for High Speed Photography of Cavity Dynamics

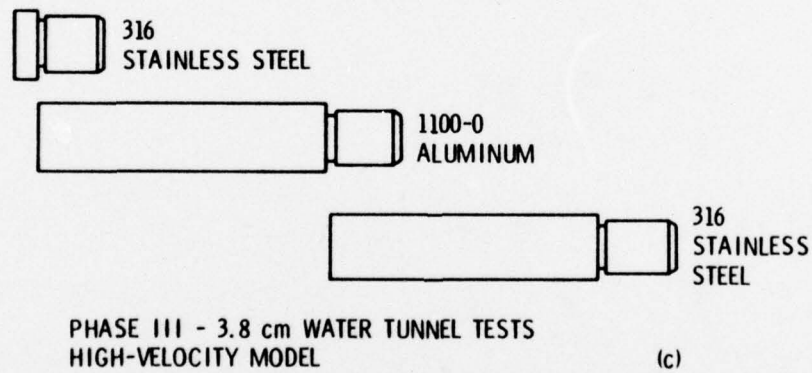
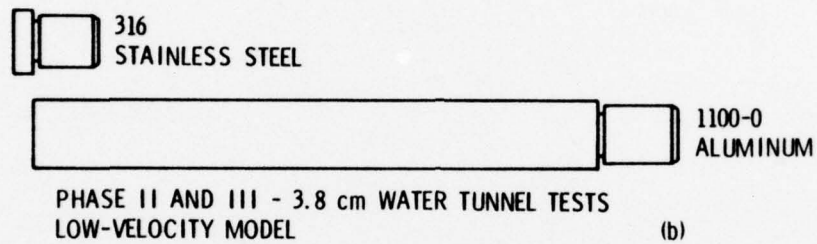
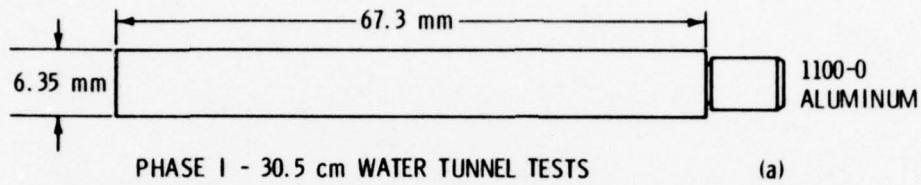


Figure 4 - Description of the Cavitation Damage Test Models

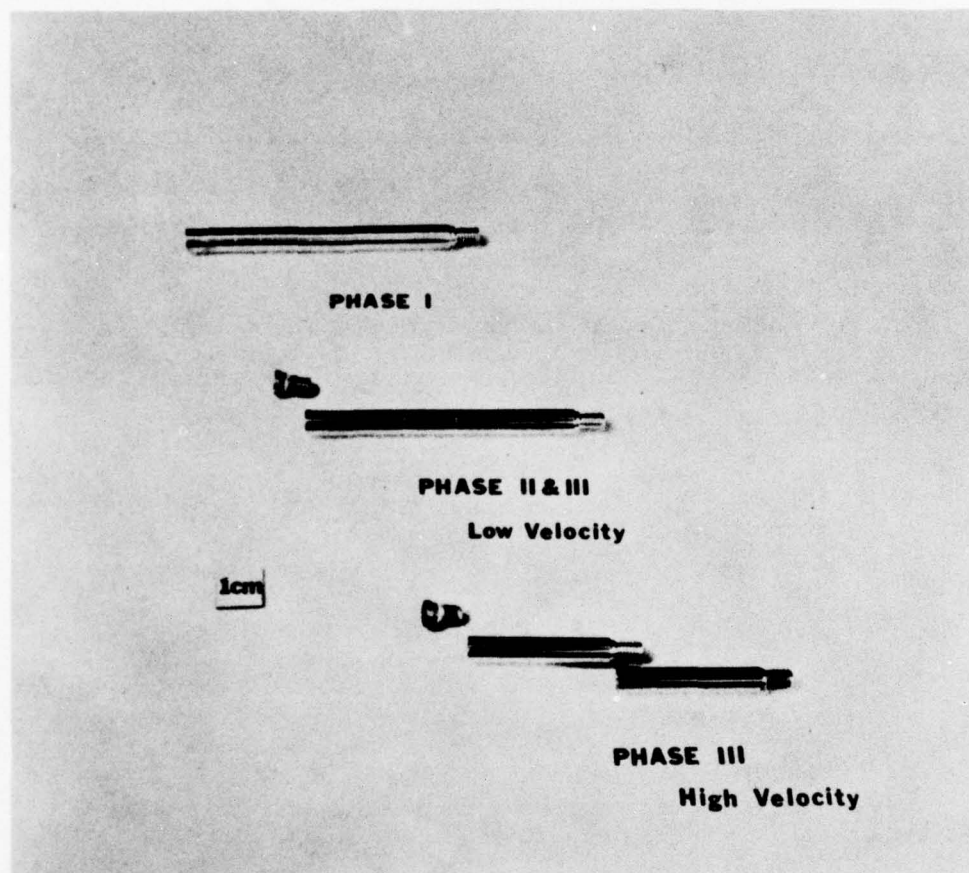


Figure 5 - Photograph of the Cavitation Damage Test Models
Prior to Testing

APPROXIMATE
CAVITY OUTLINE FOR
 $L/D = 2.0$

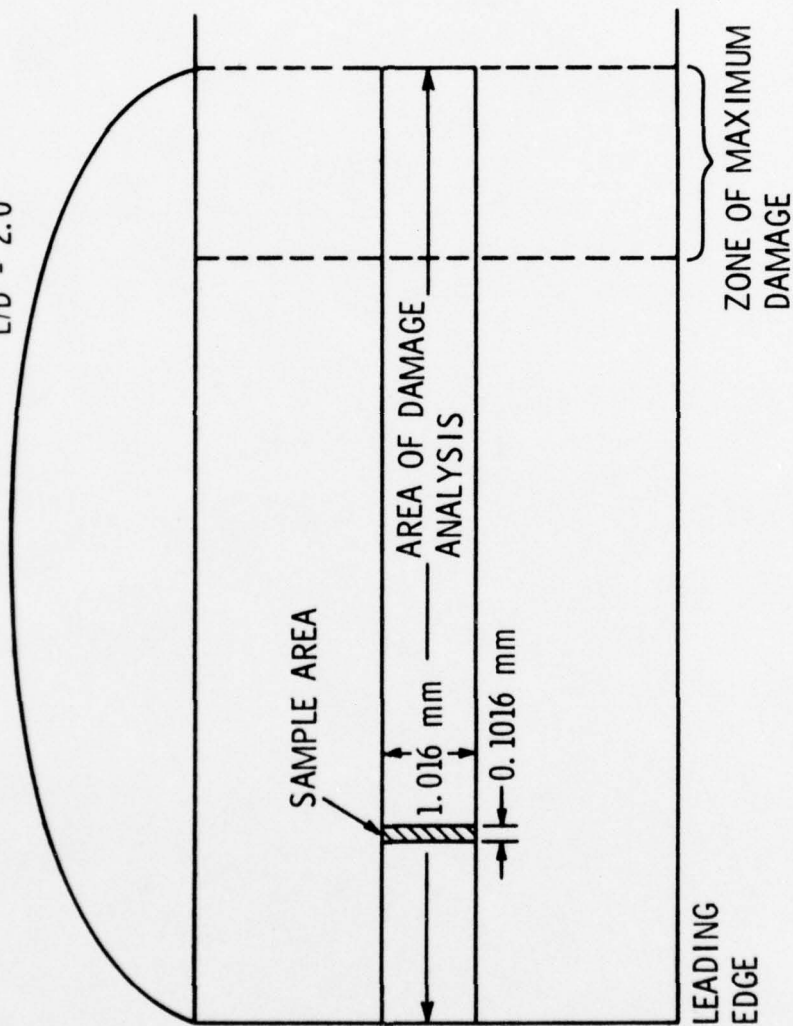


Figure 6 - Description of the Area of Damage Analysis for Phase I Test Models
(Damage Analysis for a Dimensionless Cavity Length of 2.0 Used as
an Example)

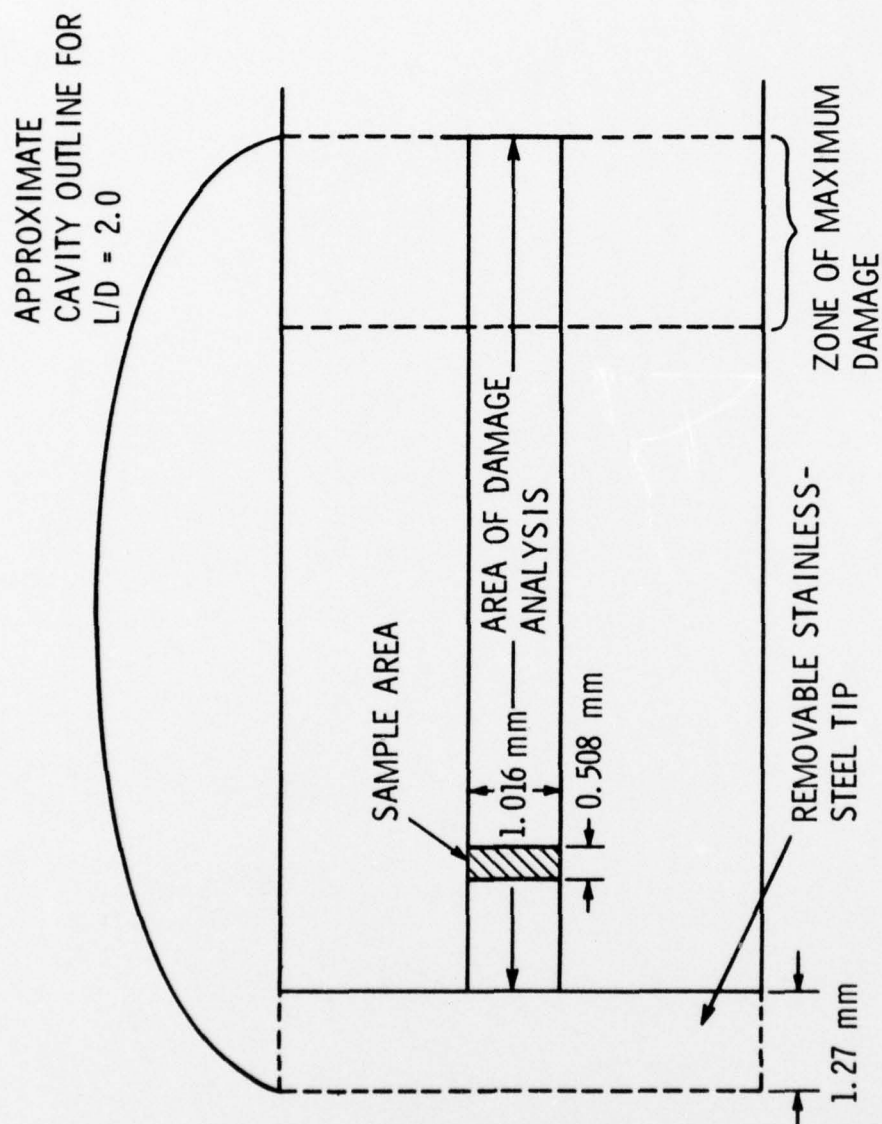


Figure 7 - Description of the Area of Damage Analysis for Phase II and III Test Models
(Damage Analysis for a Dimensionless Cavity Length of 2.0 Used as an Example)

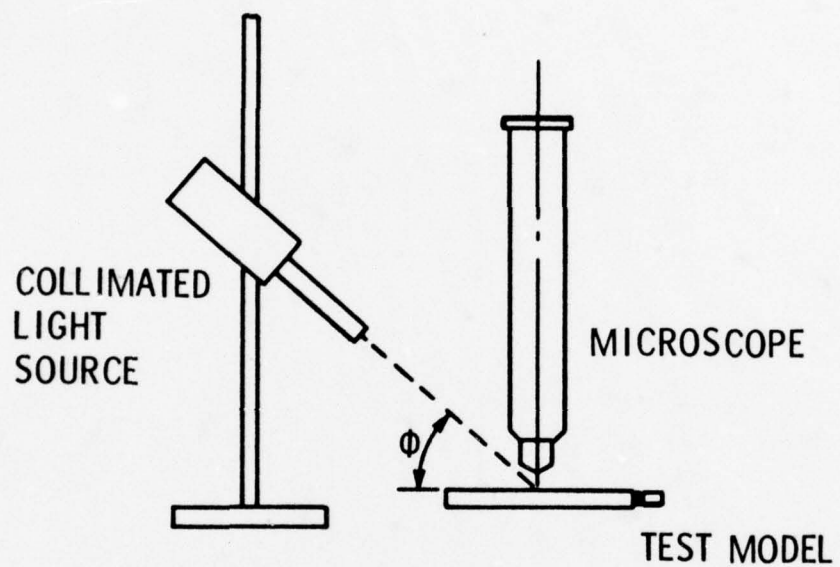
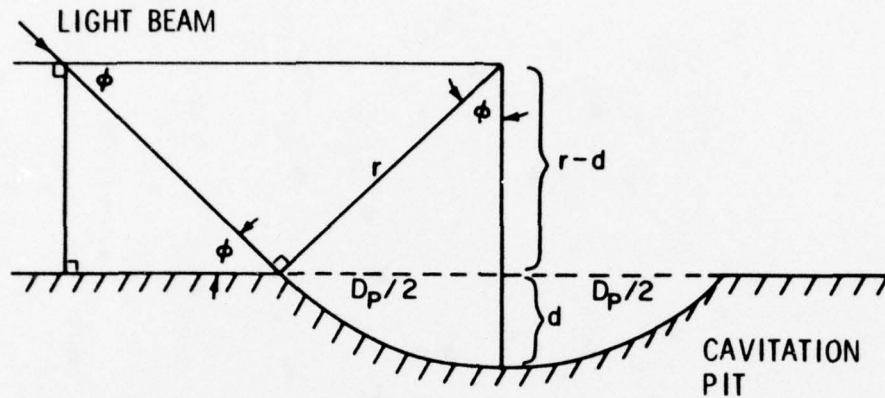


Figure 8 - Schematic Arrangement of Apparatus Used for Pit Volume Measurements



$$r = \frac{D_p / 2}{\sin \phi}$$

$$r - d = \frac{D_p \cot \phi}{2}$$

$$d = \frac{D_p / 2}{\sin \phi} - \frac{D_p \cot \phi}{2} = \frac{D_p / 2}{\sin \phi} (1 - \cos \phi)$$

$$V = \frac{\pi}{6} d \left[\frac{3 D_p^2}{4} + d^2 \right]$$

$$V = \frac{\pi}{6} \left[\frac{D_p}{2 \sin \phi} (1 - \cos \phi) \right] \left[\frac{3 D_p^2}{4} + \left(\frac{D_p}{2 \sin \phi} (1 - \cos \phi) \right)^2 \right]$$

Figure 9 - Definition Sketch and Equations for the Calculations of Pit Volumes

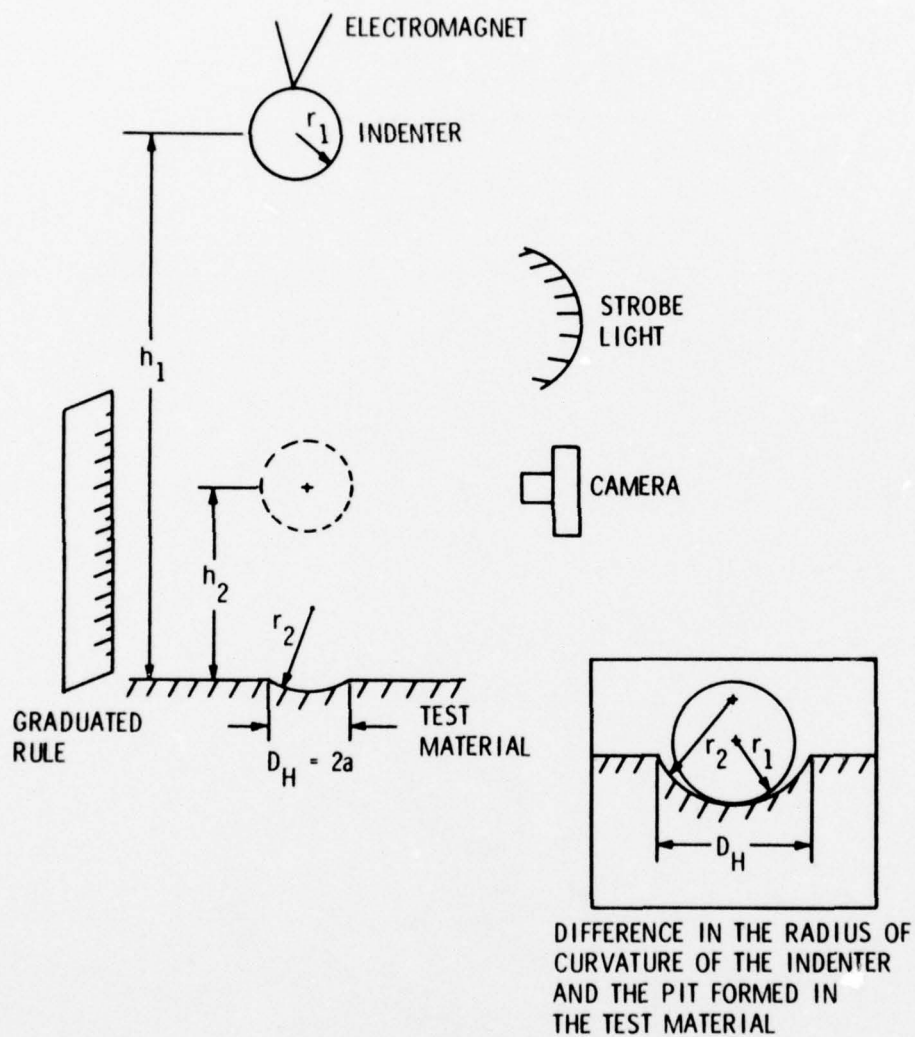


Figure 10 - Schematic Diagram of the Dynamic Hardness Test

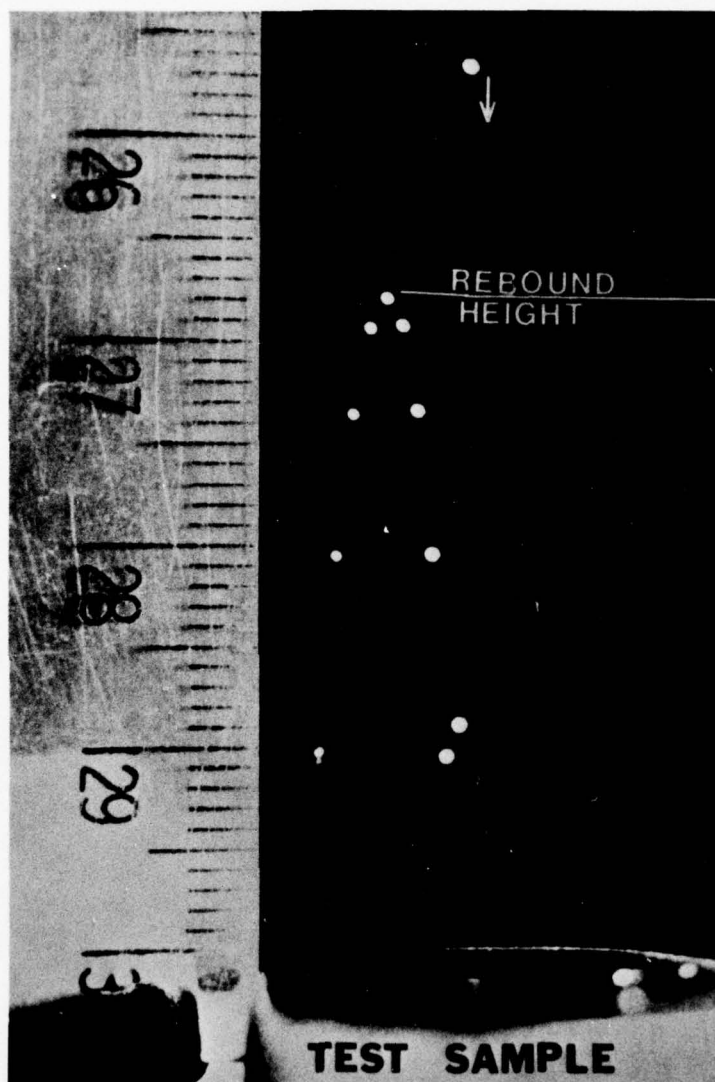


Figure 11 - Photograph of Indenter Rebound for a Dynamic Hardness Test (0.2 m Initial Drop Height, 1 mm Divisions on Right Side of Rule, Zero of Scale at 30 cm of Rule)

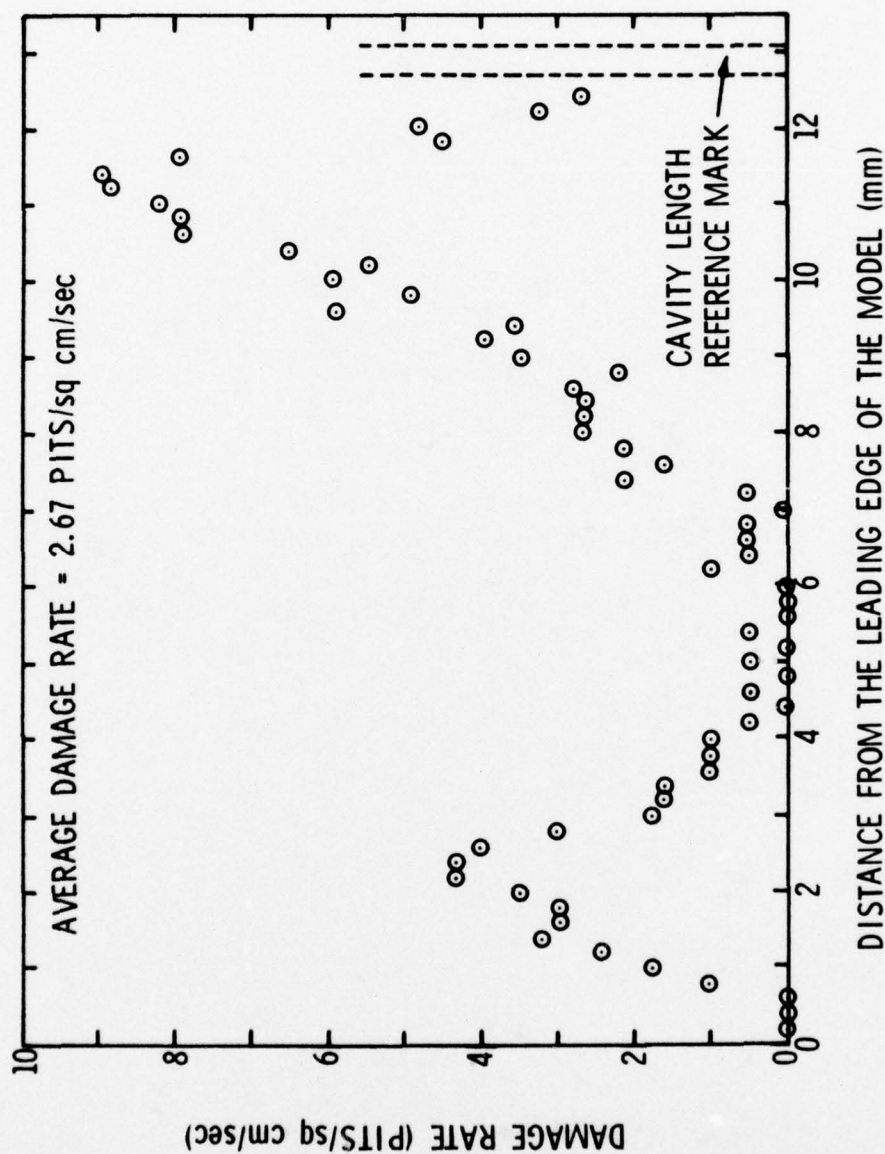


Figure 12 - Plot of the Damage Rate Distribution Along a Phase I Test Model (Model 1, $V_{\infty} = 21.3$ m/sec, $L/D=2$, and 30-Minute Test Duration)

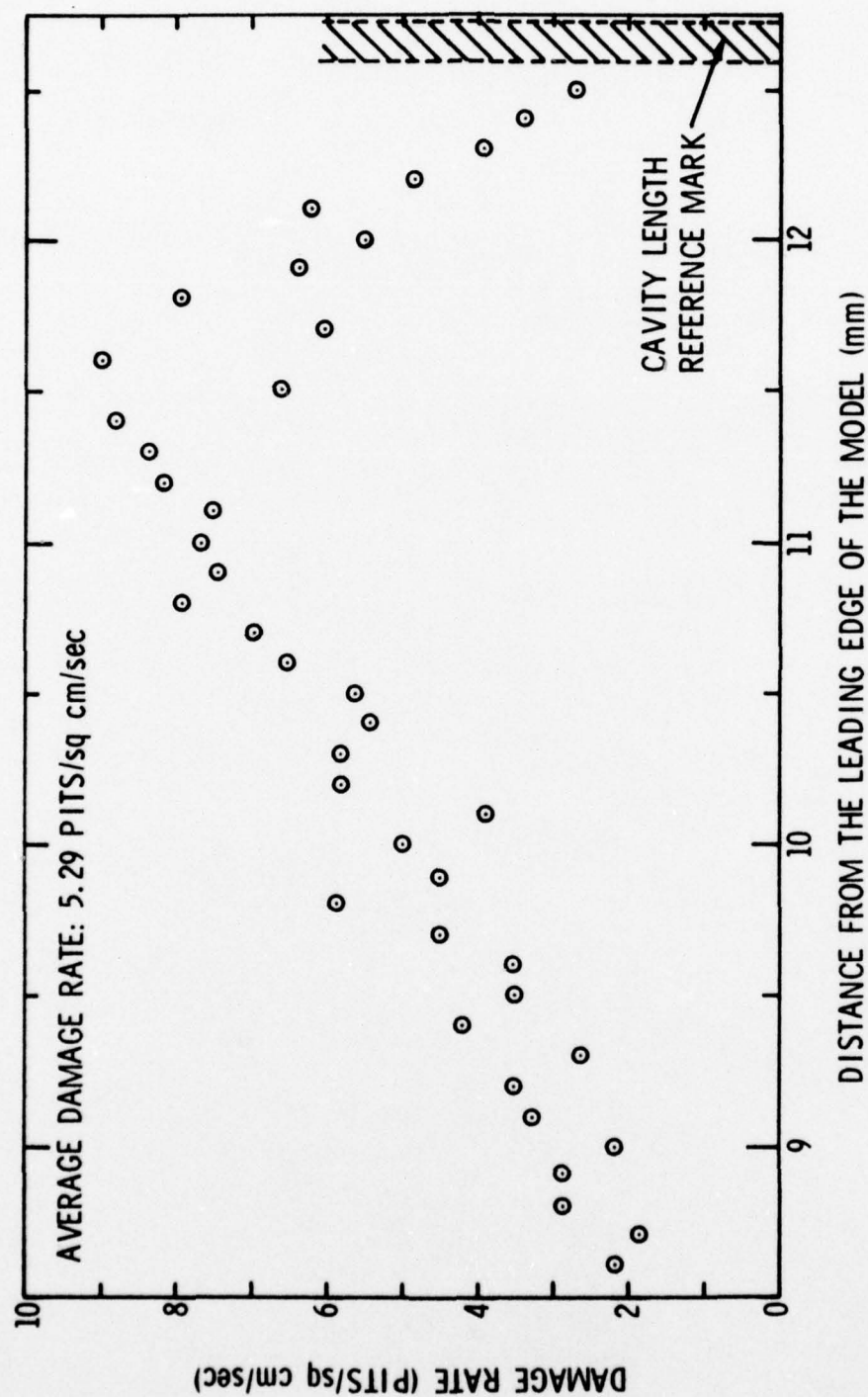


Figure 13 - Plot of the Damage Rate Distribution in the Maximum Damage Zone Along Model 1
($V_{\infty}=21.3$ m/sec, $L/D=2$, and 30-Minute Test Duration)

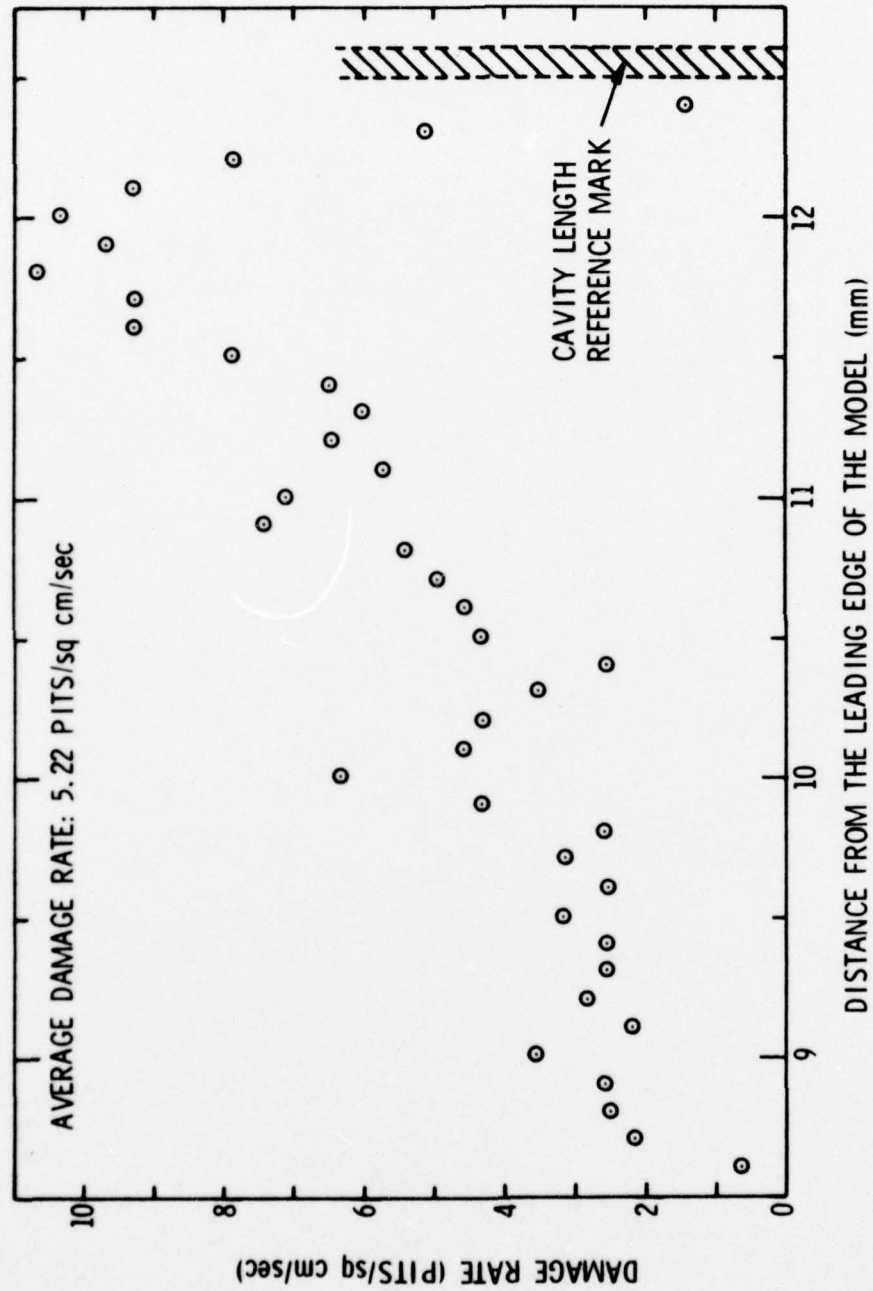


Figure 14 - Plot of the Damage Rate Distribution in the Maximum Damage Zone Along Model 5
($V_{\infty} = 21.3$ m/sec, $L/D=2$, and 15-Minute Test Duration)

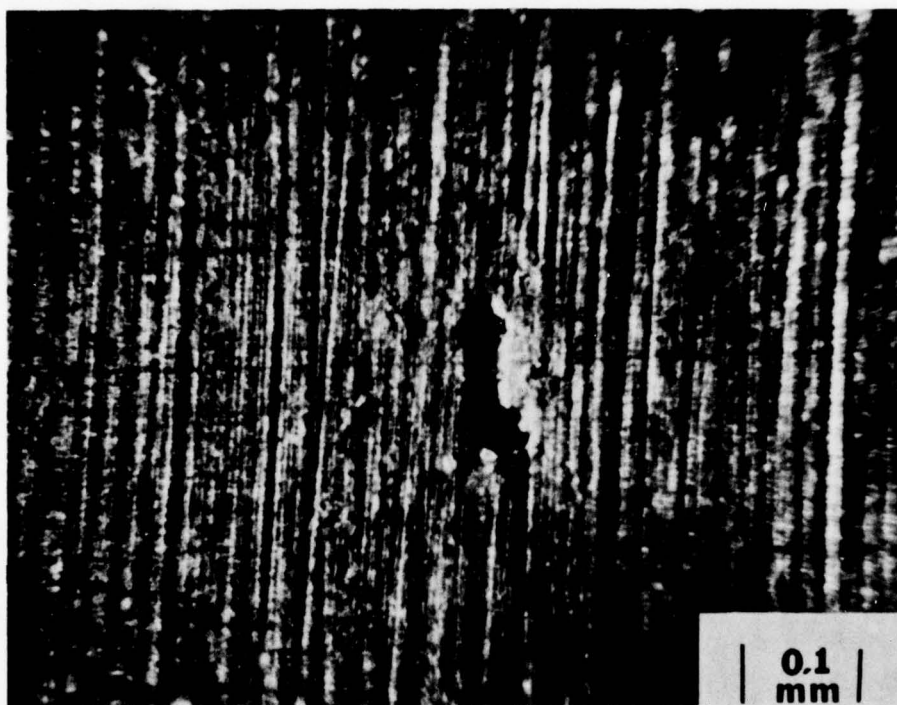


Figure 15 - Photomicrograph of a Large Pit in Which Material Has Been Removed from the Surface (Phase I Test Model)

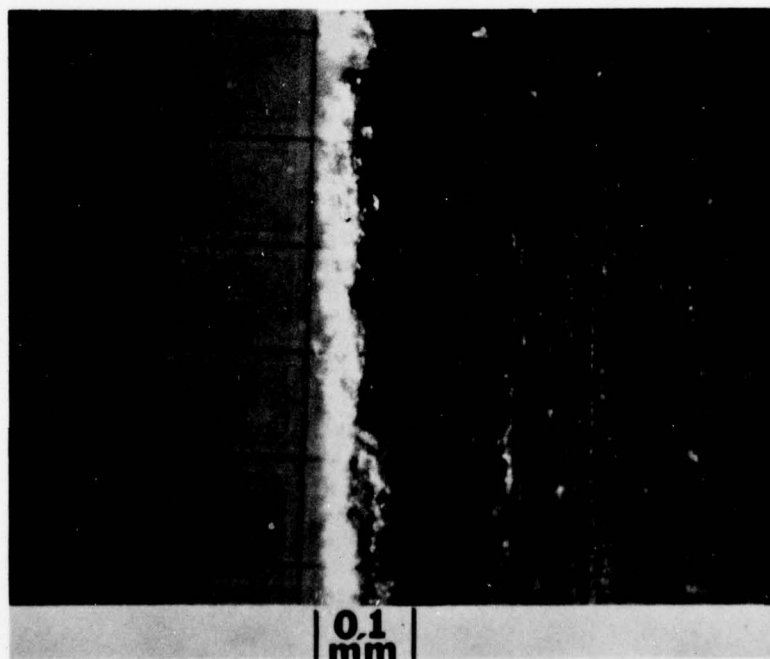
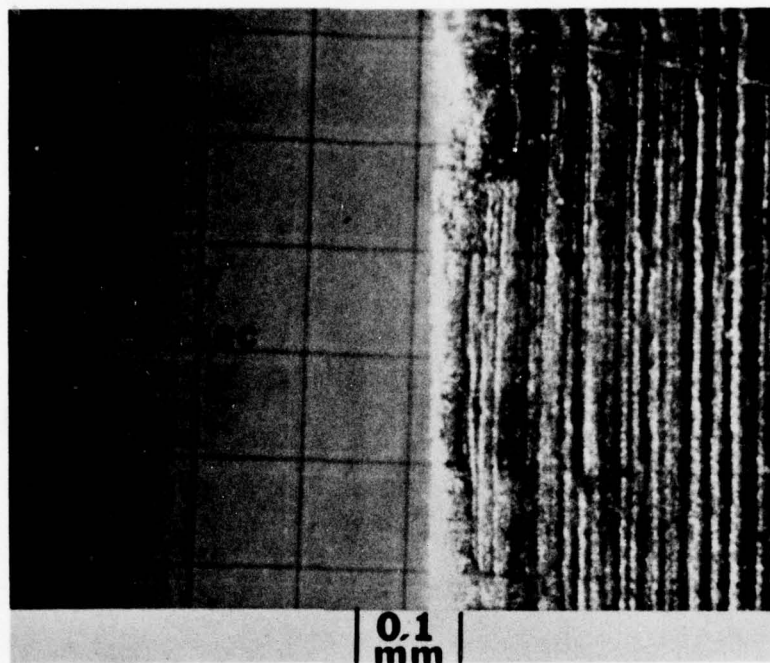


Figure 16 - Photomicrographs Showing the Effect of Velocity on the Deformation of the Leading Edge Contour for Phase I Models

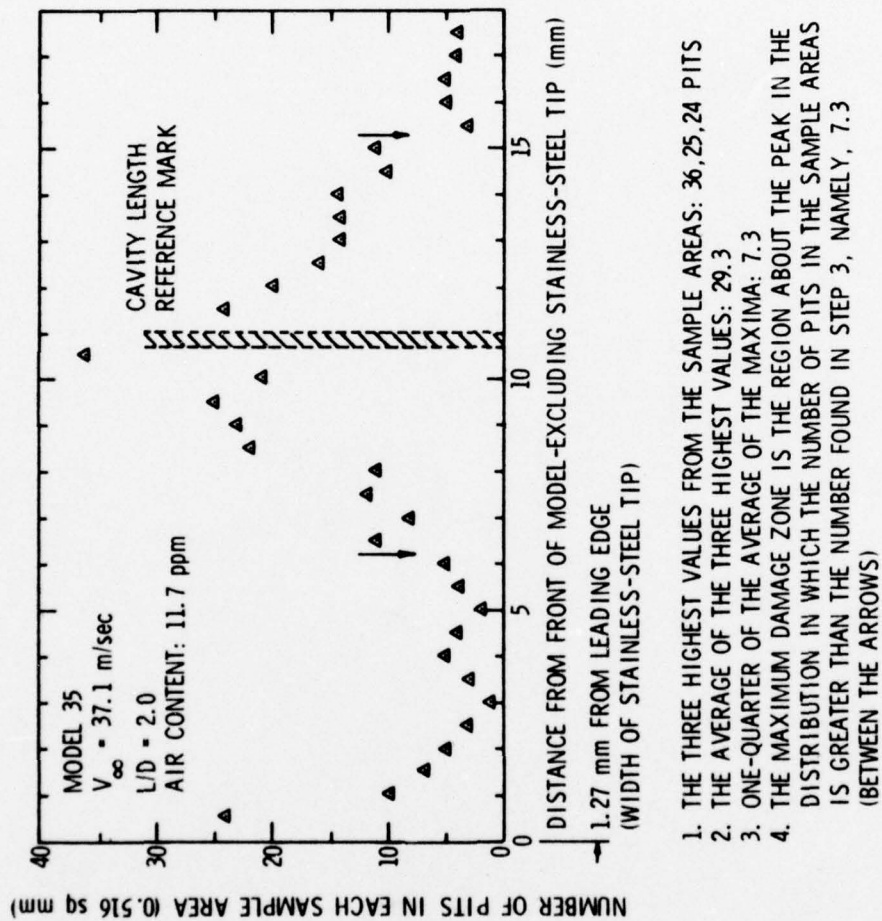


Figure 17 - Schematic Diagram of the Method for Calculation of the Extent of the Maximum Damage Zone for Phase II and III Models

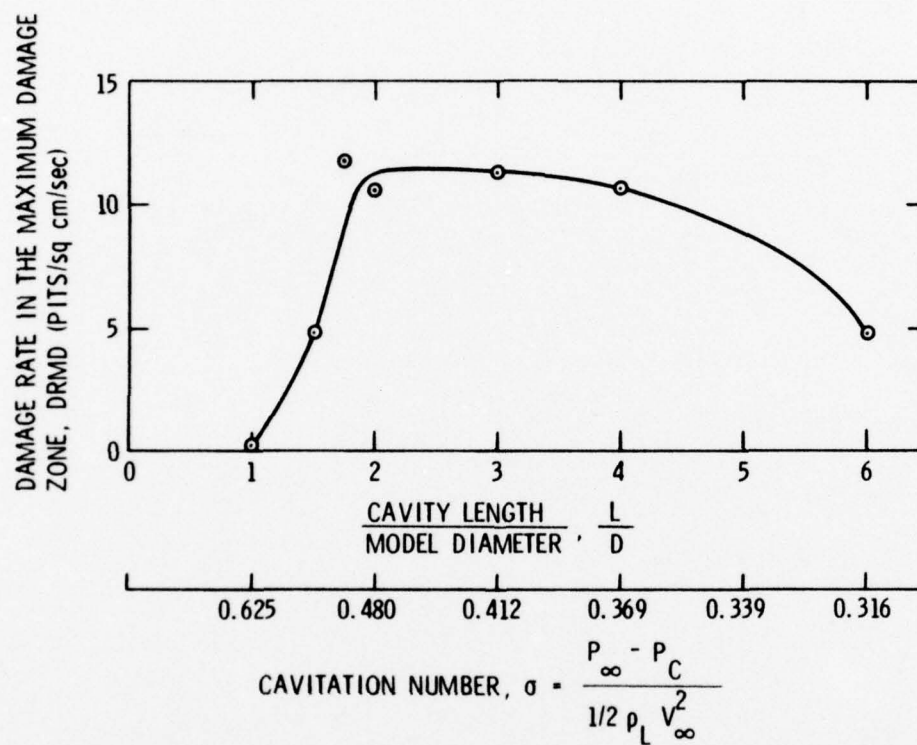


Figure 18 - Damage Rate in the Maximum Damage Zone (DRMD) Versus Dimensionless Cavity Length and Cavitation Number (Phase III Models, $V_{\infty}=38$ m/sec, and an Air Content of 10 ppm)

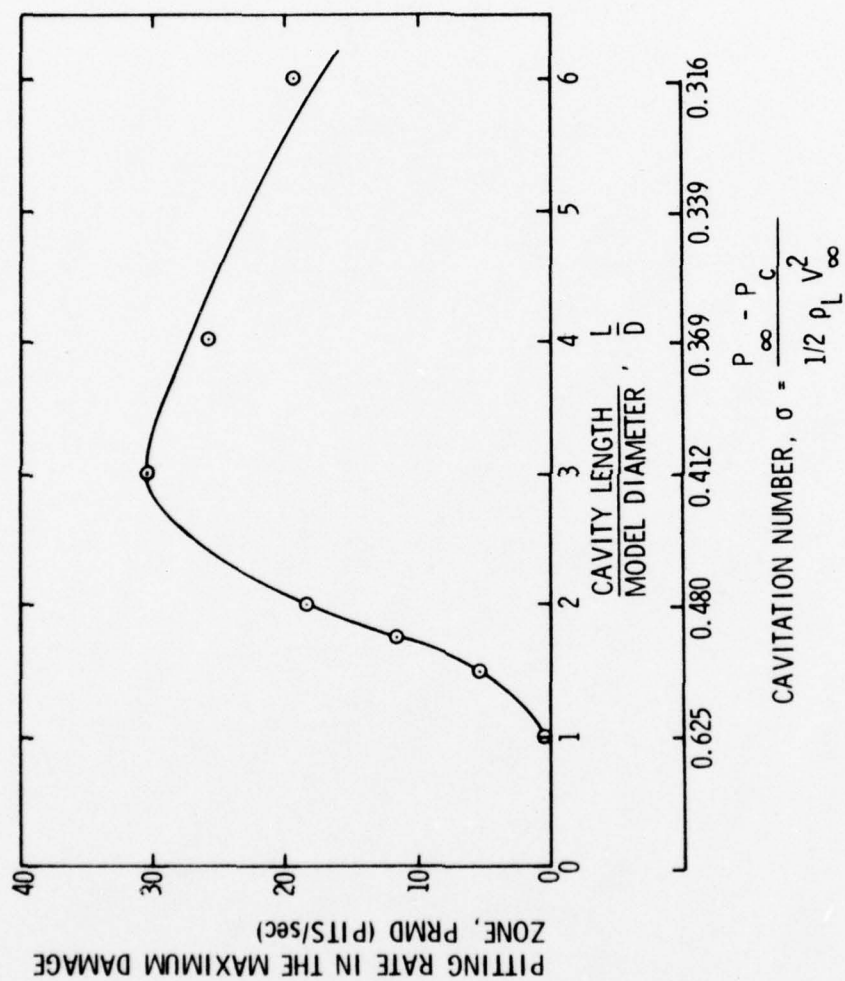


Figure 19 - Pitting Rate in the Maximum Damage Zone (PRMD) Versus Dimensionless Cavity Length and Cavitation Number (Phase III Models, $V_{\infty} = 38$ m/sec, and an Air Content of 10 ppm)

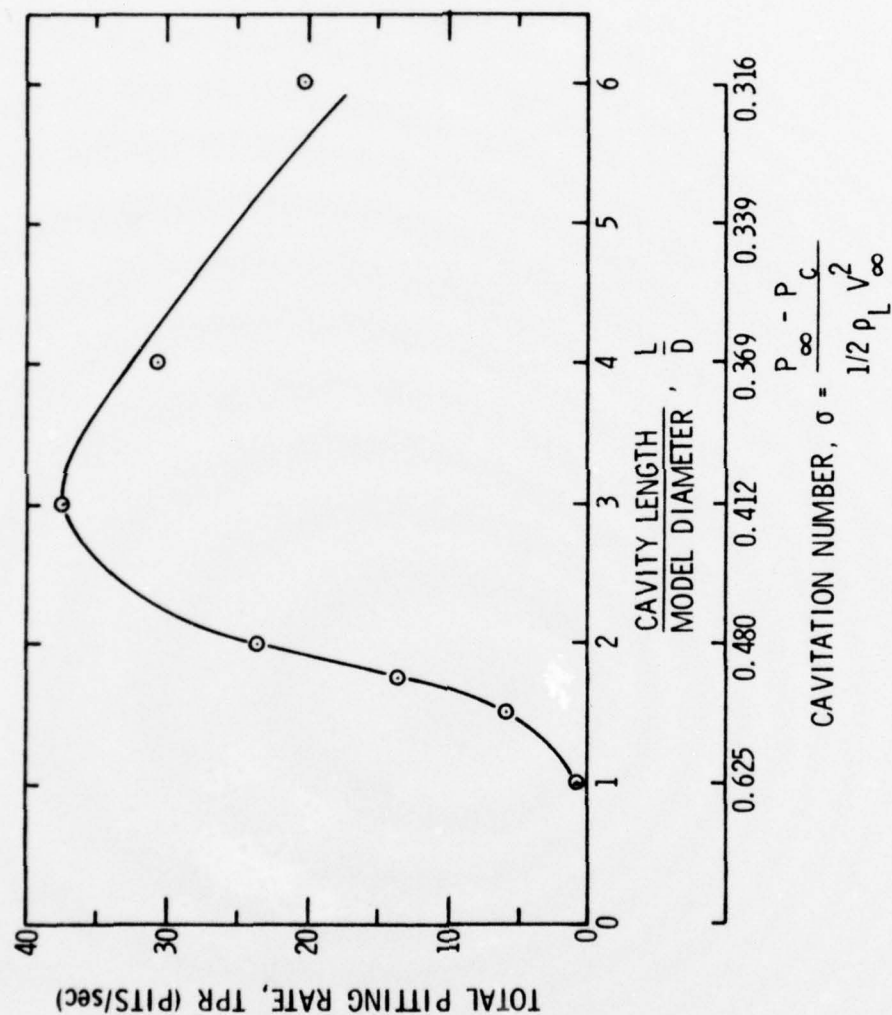


Figure 20 - Total Pitting Rate on the Model (TPR) Versus Dimensionless Cavity Length and Cavitation Number (Phase III Models, $V_{\infty} = 38$ m/sec, and an Air Content of 10 ppm)

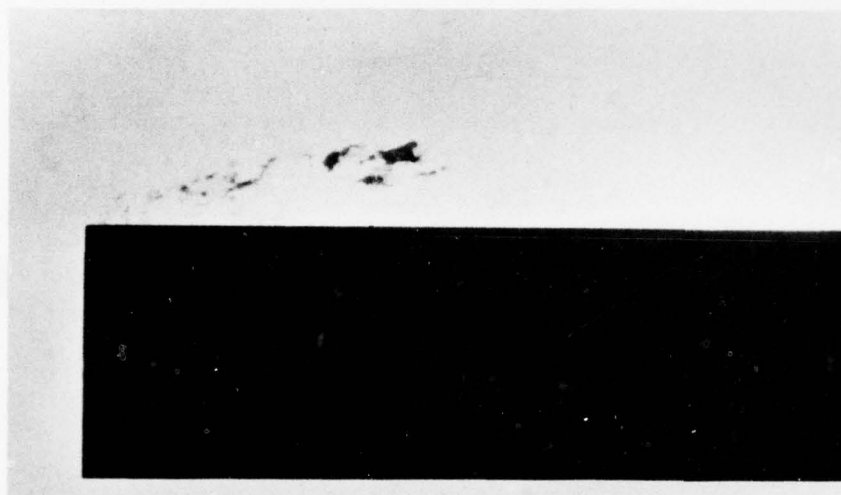


Figure 21 - Photograph of Cavity Collapse Away from the Model Surface for a Short Cavity Length (0.635 cm Diameter Zero-Caliber Ogive, 3 μ sec Flash Duration, and $V_{\infty} \approx 23$ m/sec)

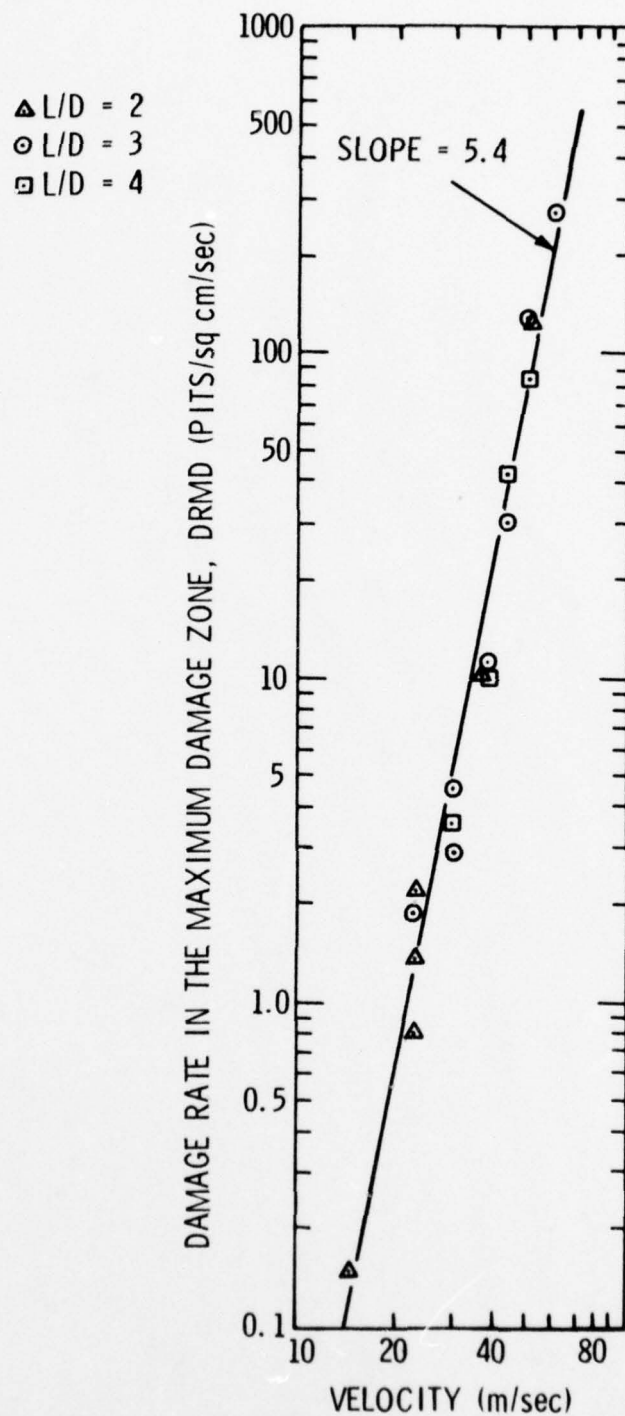


Figure 22 -- Damage Rate in the Maximum Damage Zone (DRMD) Versus Velocity for Phase III Models (Air Content - 10 ppm)

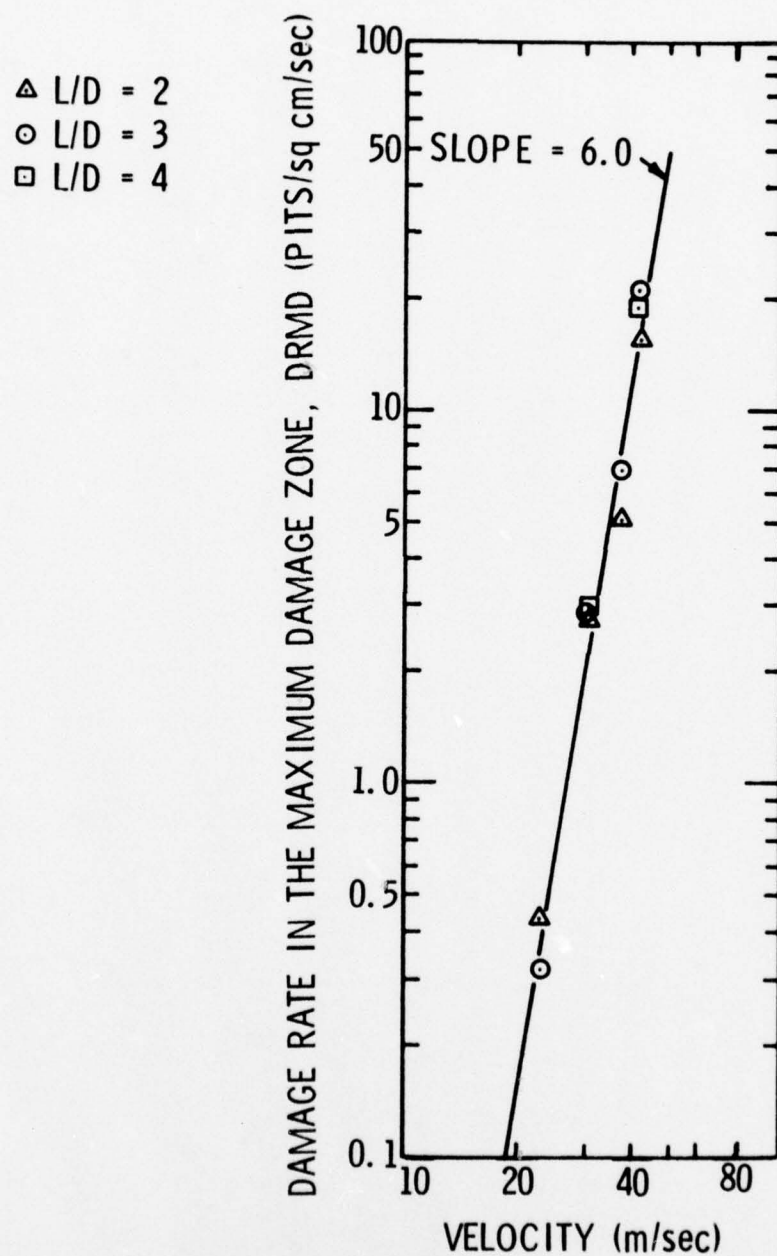


Figure 23 - Damage Rate in the Maximum Damage Zone (DRMD)
Versus Velocity for Phase II Models (Air
Content - 20 ppm)

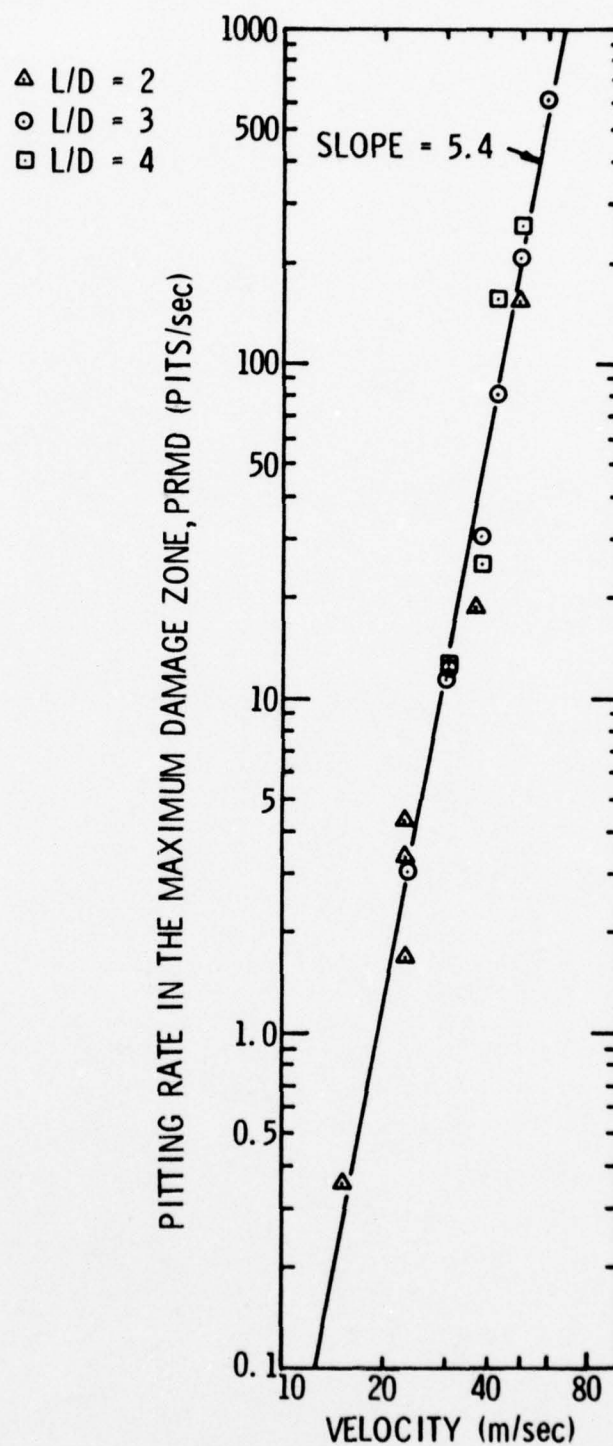


Figure 24 - Pitting Rate in the Maximum Damage Zone (PRMD) Versus Velocity for Phase III Models (Air Content - 10 ppm)

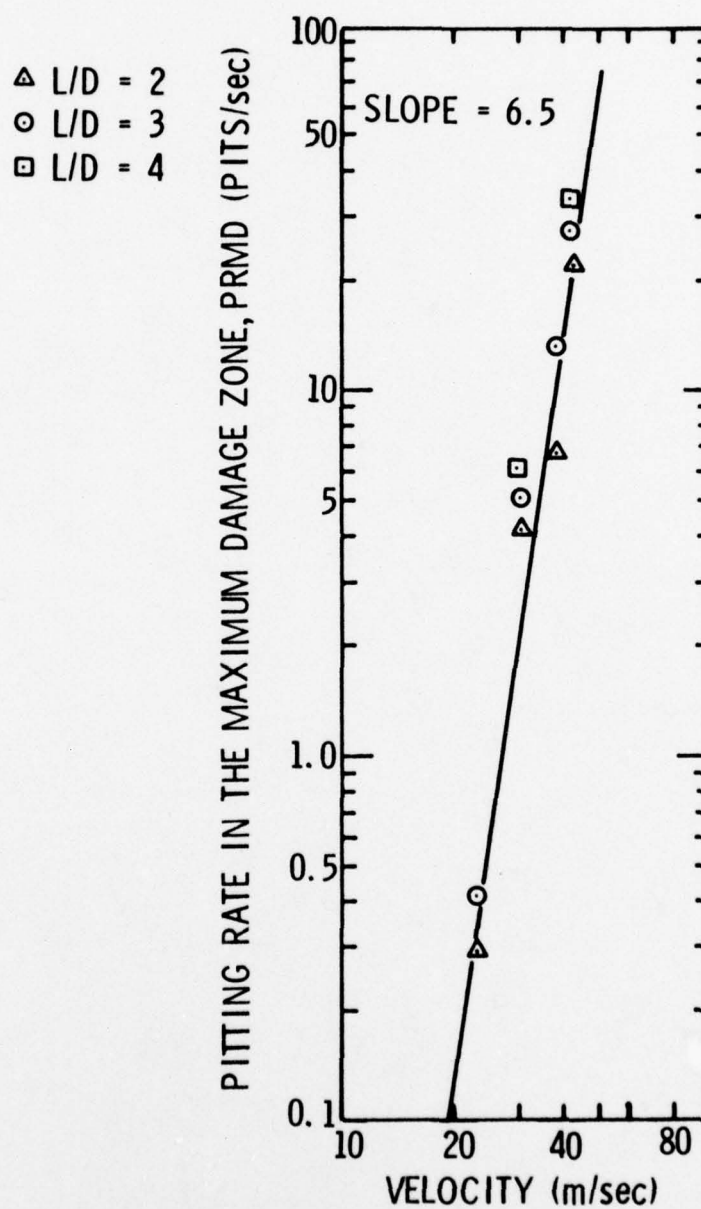


Figure 25 - Pitting Rate in the Maximum Damage Zone (PRMD)
Versus Velocity for Phase II Models (Air
Content - 20 ppm)

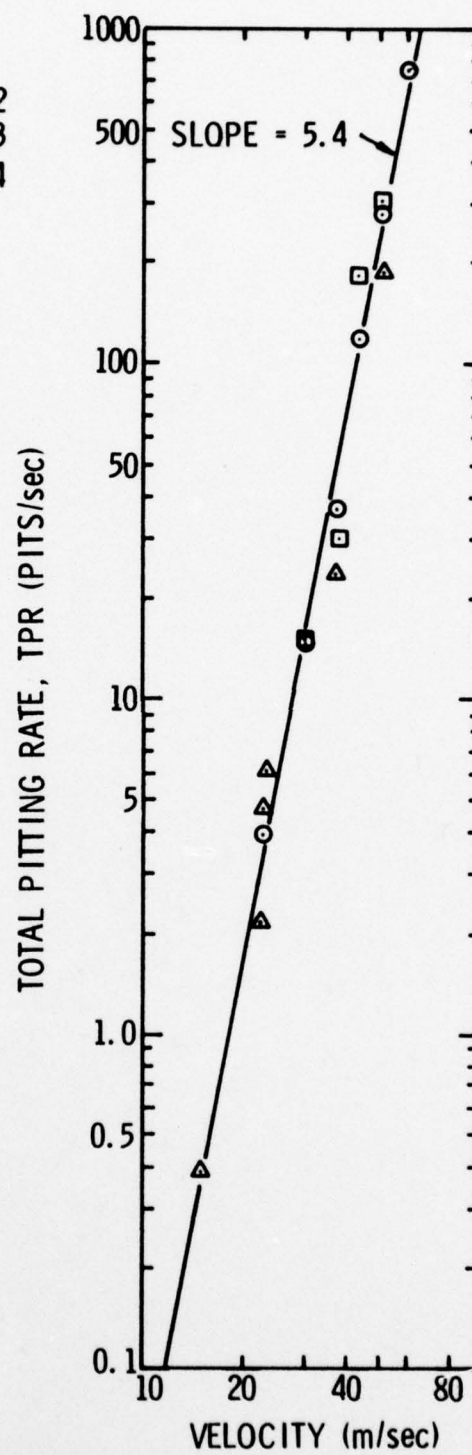


Figure 26 - Total Pitting Rate on the Model (TPR) Versus Velocity for Phase III Models (Air Content - 10 ppm)

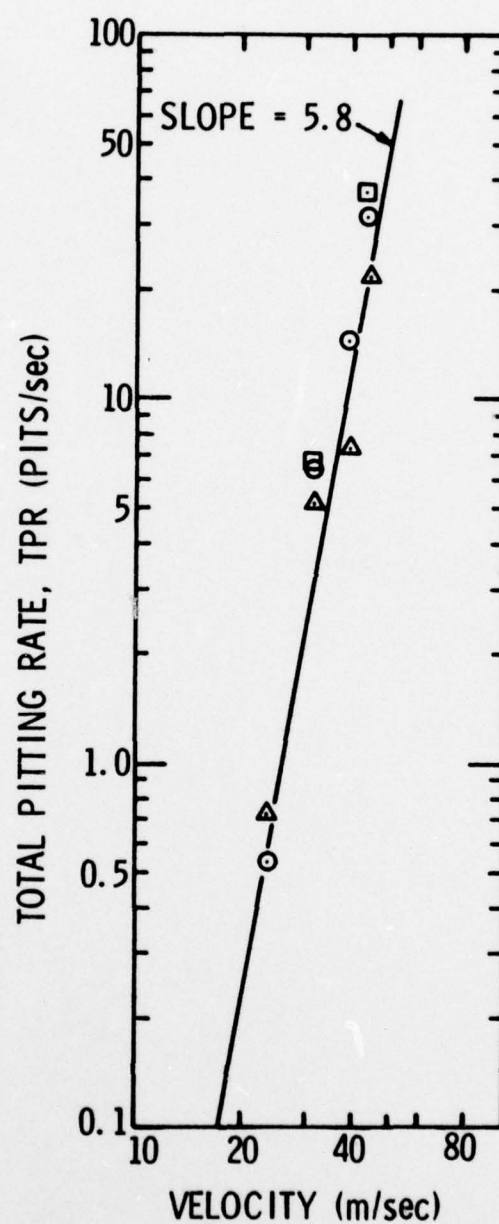


Figure 27 - Total Pitting Rate on the Model (TPR) Versus Velocity for Phase II Models (Air Content - 20 ppm)

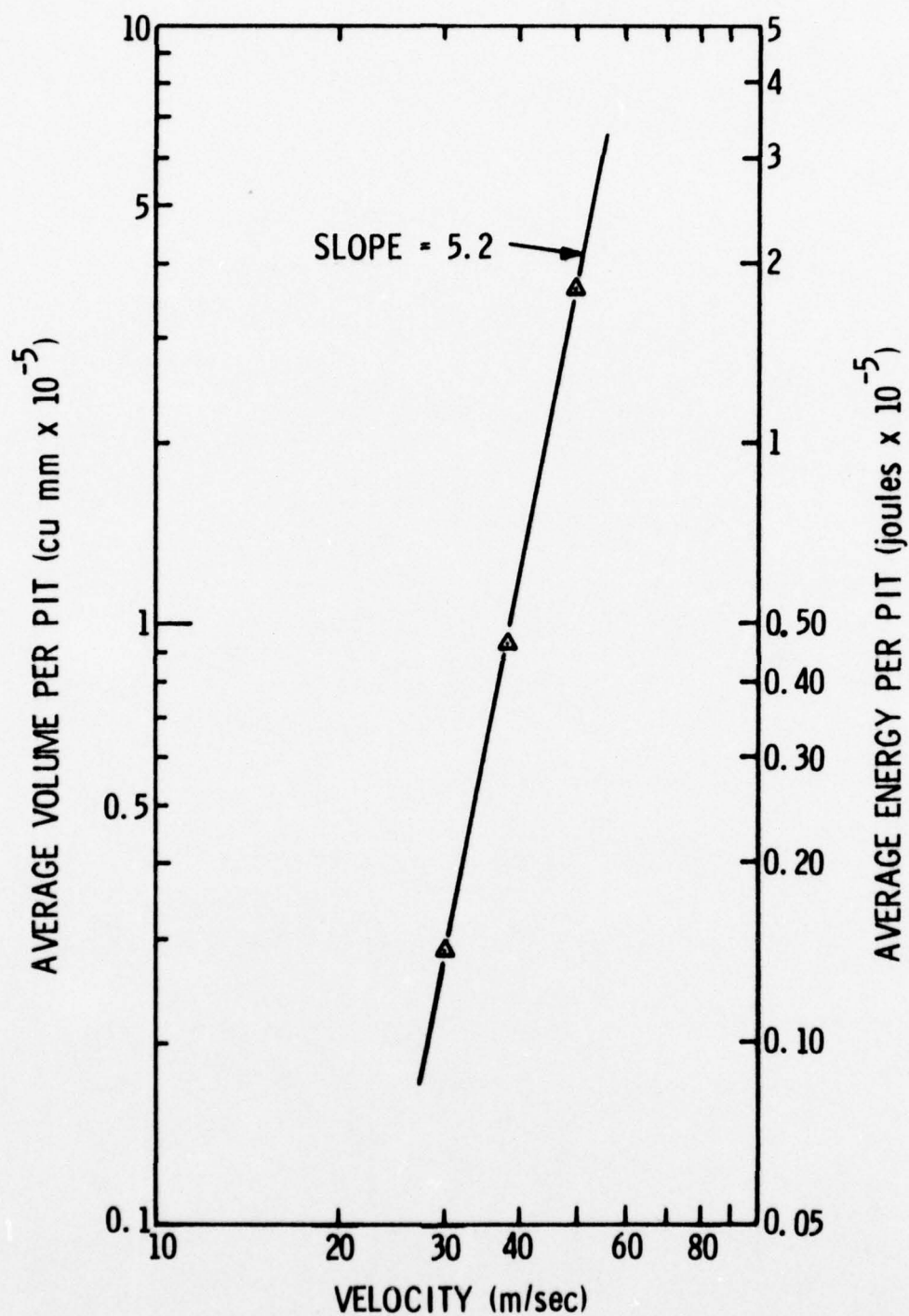


Figure 28 - Average Pit Volume (Average Energy Per Pit re A Dynamic Hardness of 0.5 J/mm^3) Versus Velocity ($L/D=3$ and an Air Content of 10 ppm)

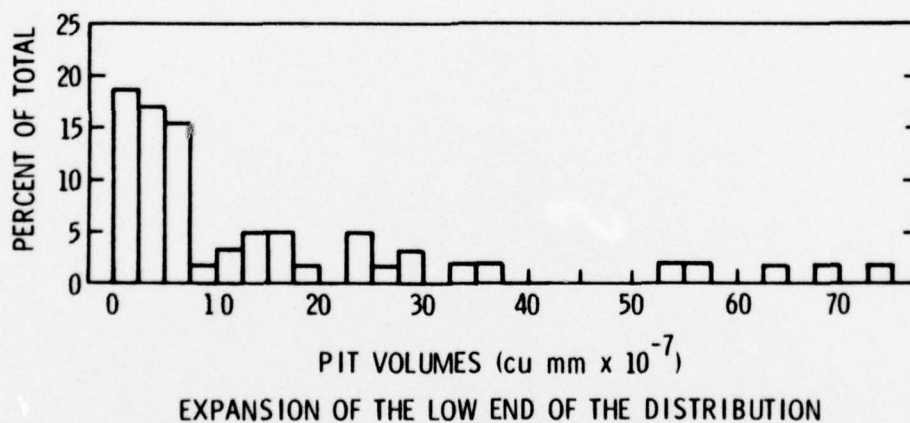
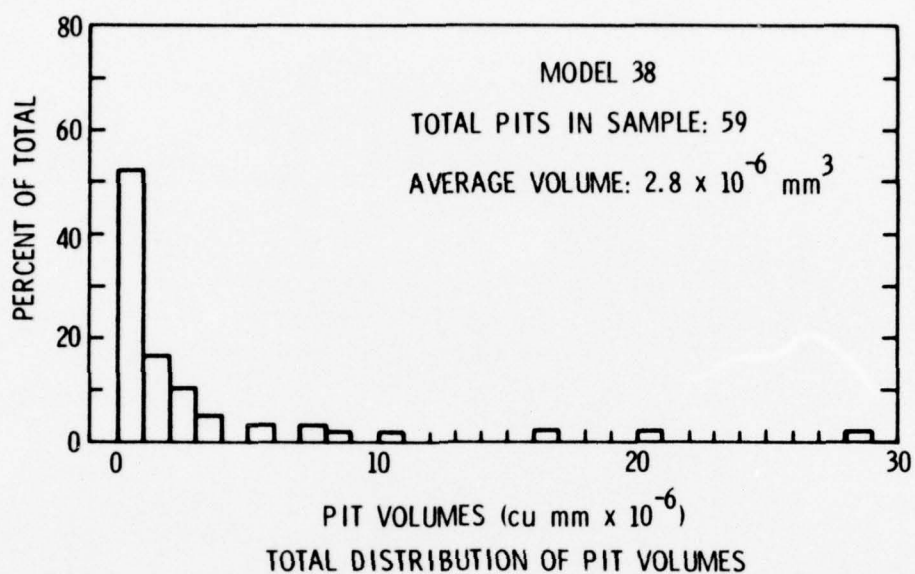


Figure 29 - Distribution of Pit Volumes for a Velocity of 30.1 m/sec and a Dimensionless Cavity Length of 3.0 (Air Content - 10 ppm)

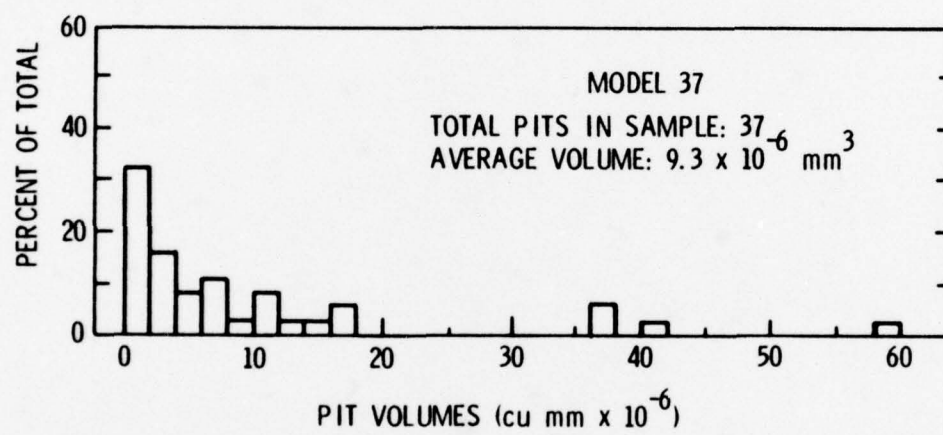


Figure 30 - Distribution of Pit Volumes for a Velocity of 38 m/sec and a Dimensionless Cavity Length of 3.0 (Air Content - 10 ppm)

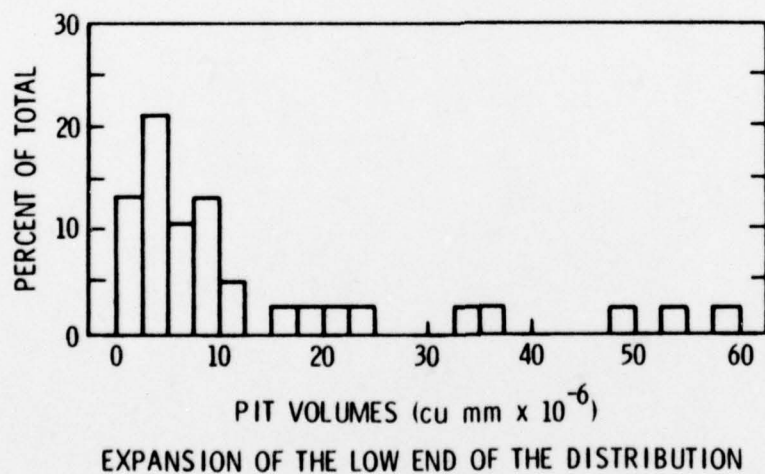
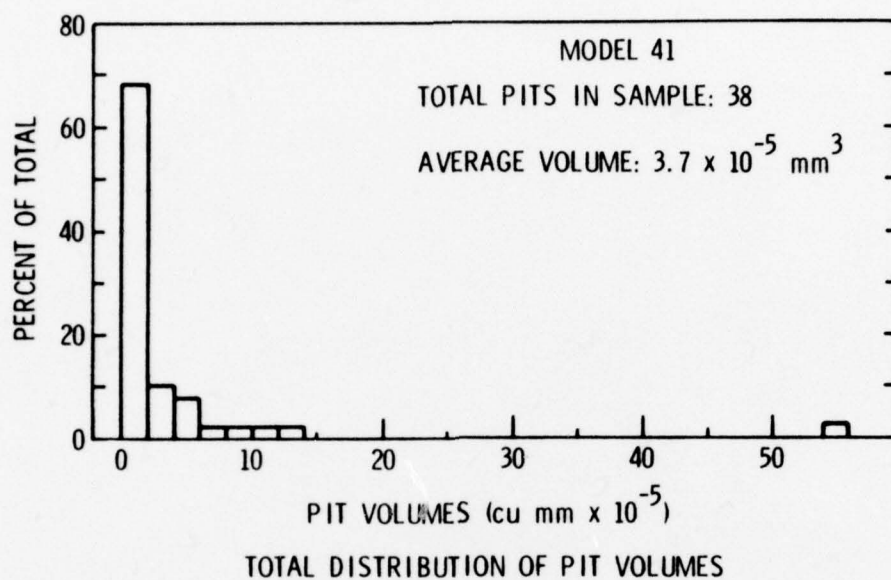


Figure 31 - Distribution of Pit Volumes for a Velocity of 49.3 m/sec and a Dimensionless Cavity Length of 3.0 (Air Content - 10 ppm)

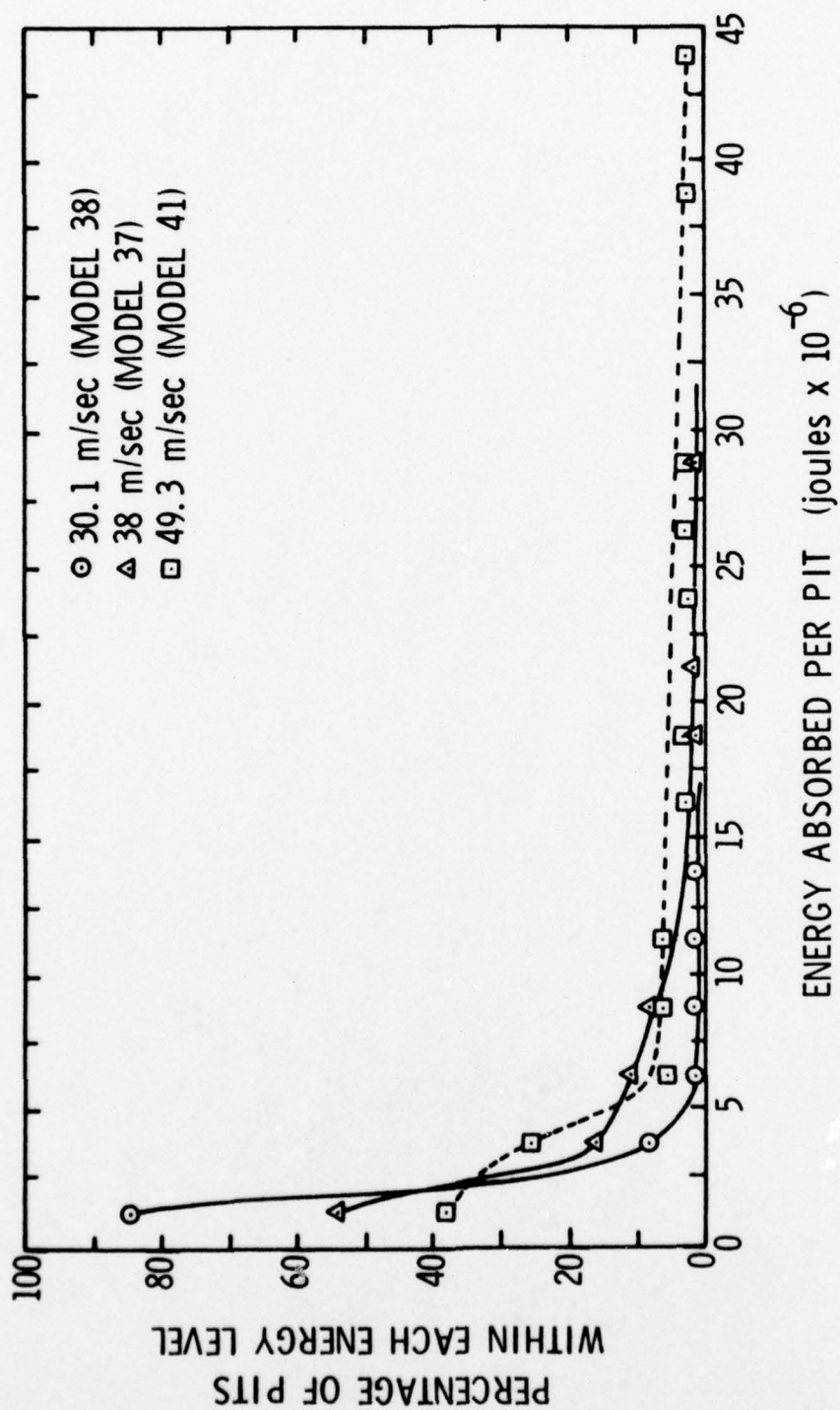


Figure 32 - Energy Probability Density Distribution for Test Velocities of 30.1, 38.0, and 49.3 m/sec (L/D=3 and an Air Content of 10 ppm)

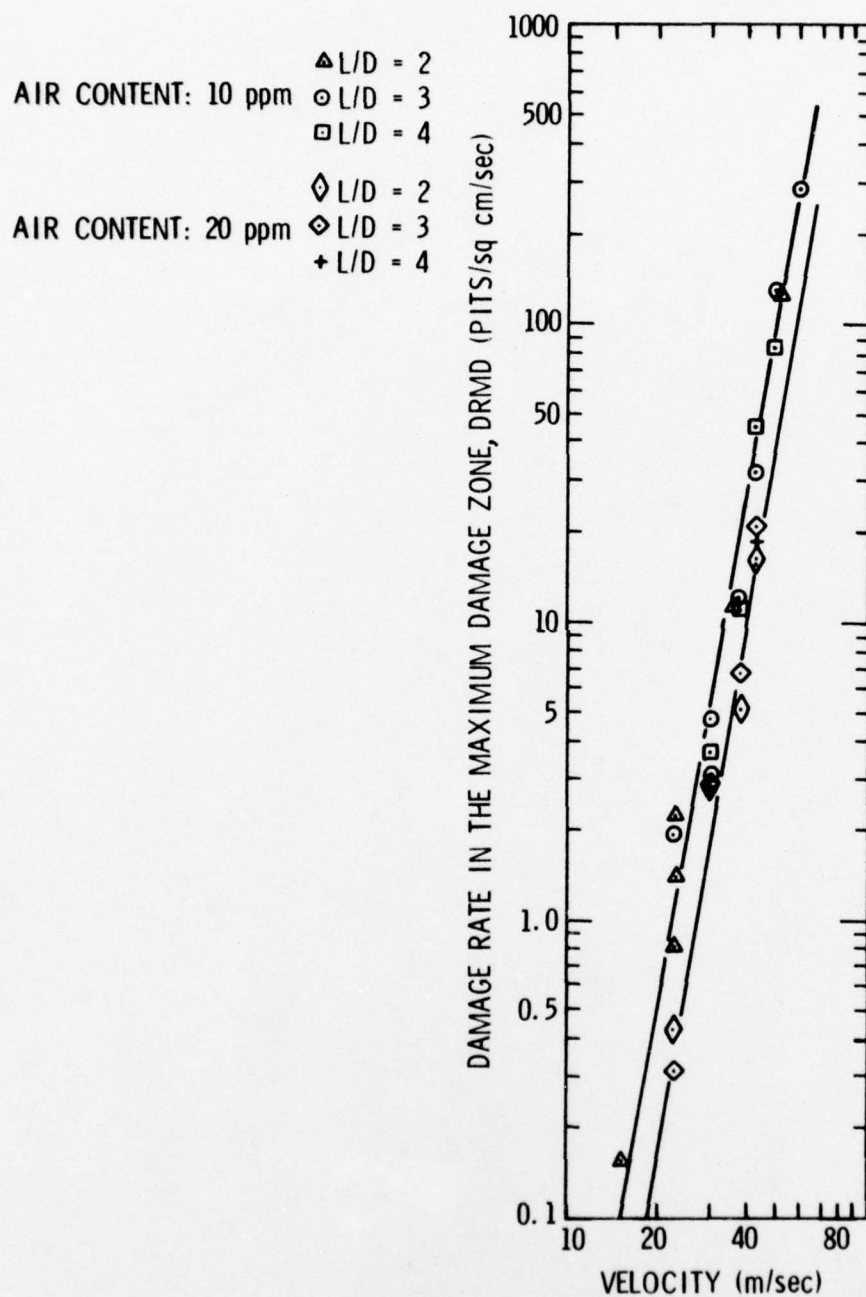


Figure 33 - Effect of Air Content on the Damage Rate in the Maximum Damage Zone

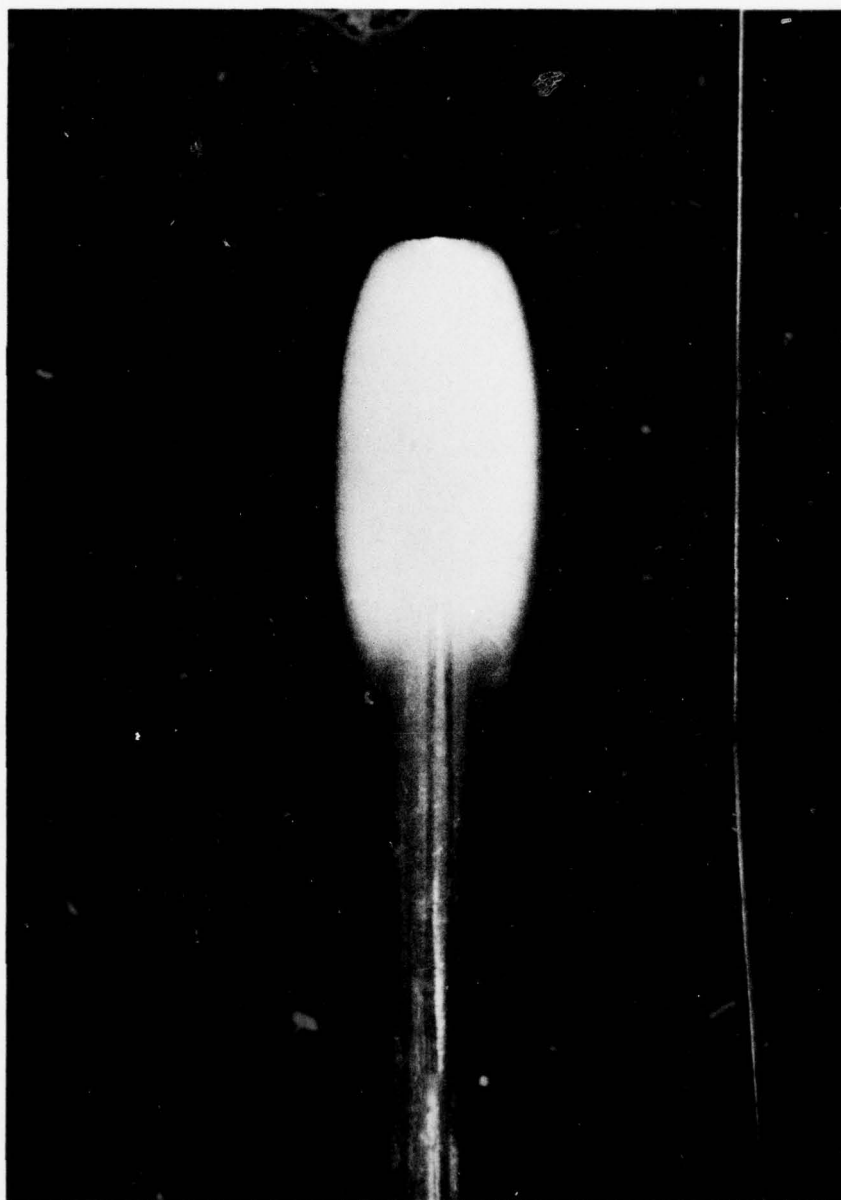


Figure 34 - Photograph of a Developed Cavity in Water as it Appears to the Eye (0.635 cm Diameter Zero-Caliber Ogive, $V_{\infty}=19.5$ m/sec, and $L/D=5$)

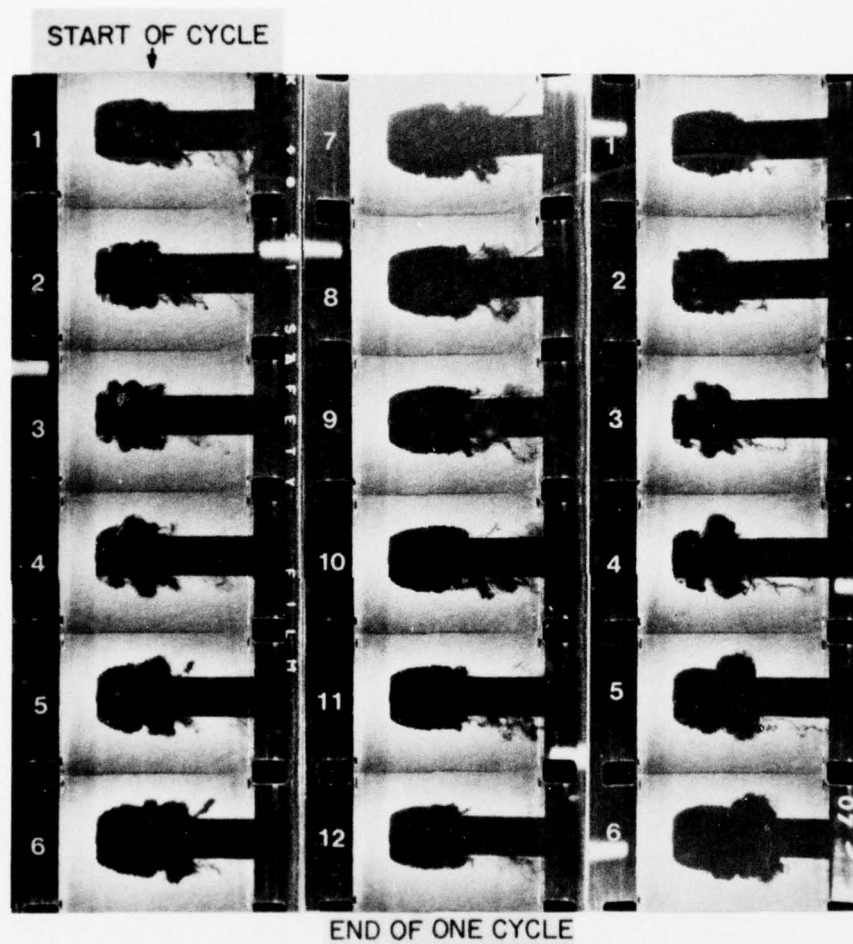
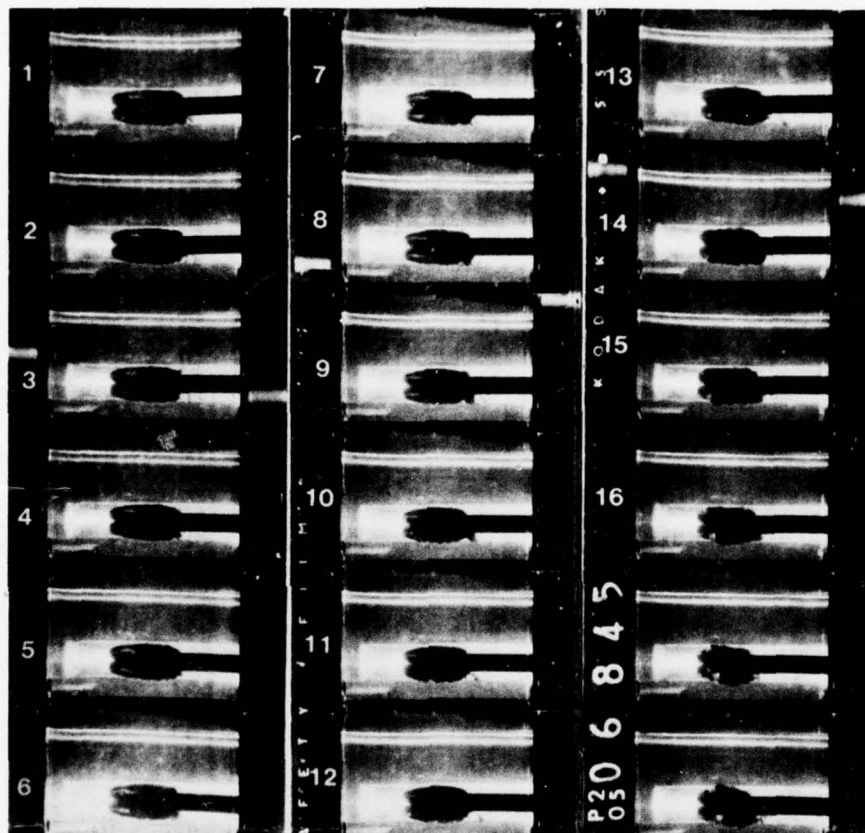


Figure 35 - High Speed Movie Sequence of a Complete Cycle of a Developed Cavity - 5000 Frames Per Second (0.635 cm Diameter Zero-Caliber Ogive, $V_{\infty}=25$ m/sec and $L/D=2.5$)



Figure 36 - High Speed Movie Segments Showing the Vortex Filaments Connecting the Sections of the Cavity After Breakoff (0.635 cm Diameter Zero-Caliber Ogive, $V_{\infty}=25$ m/sec, and $L/D=2.5$)



Jet Strikes Leading Edge of Cavity Between Frames 11 and 12

Figure 37 - High Speed Movie Sequence of the Reentrant Jet Moving Through the Cavity and Striking the Cavity Leading Edge (0.635 cm Diameter Zero-Caliber Ogive, $V_{\infty}=15$ m/sec, and $L/D=4$)

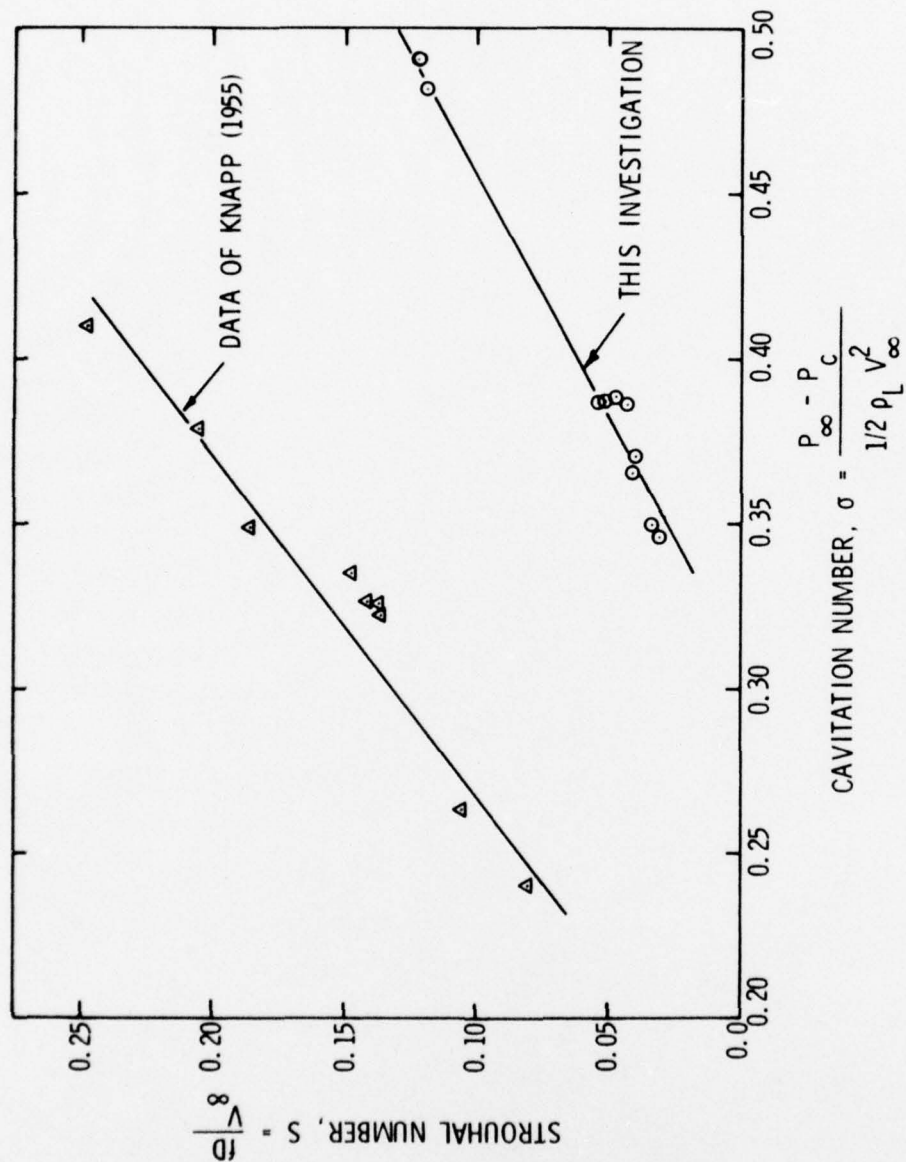


Figure 38 - Cavity Cycle Strouhal Number Versus Cavitation Number

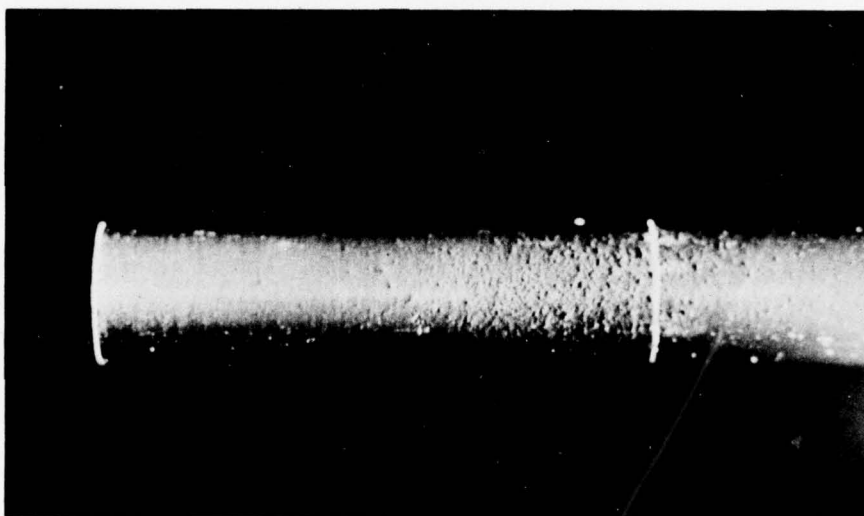


Figure 39 - Photograph of the Area of Cavitation Damage
Attack on a Test Model (0.635 cm Diameter
Zero-Caliber Ogive, Model 46, $V_{\infty}=50$ m/sec,
 $L/D=4$, Air Content - 8.5 ppm, and a 53-Second
Test Duration)

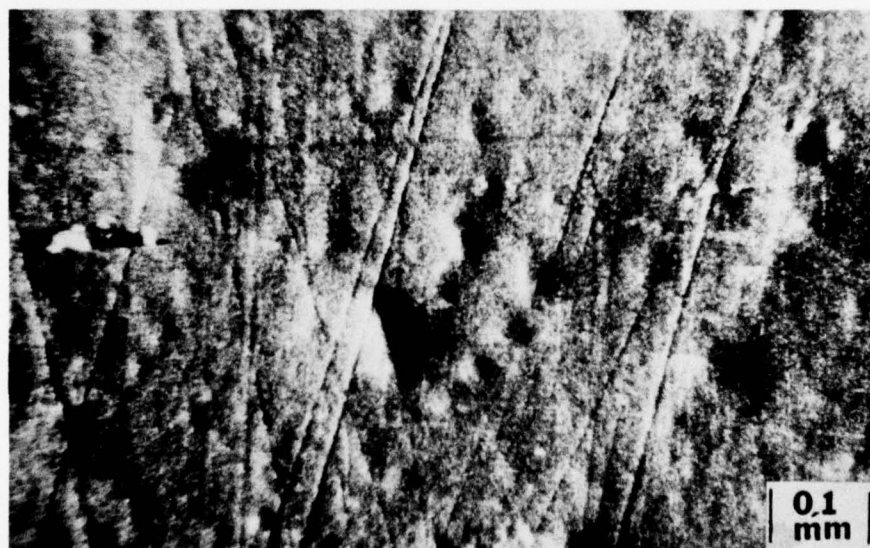
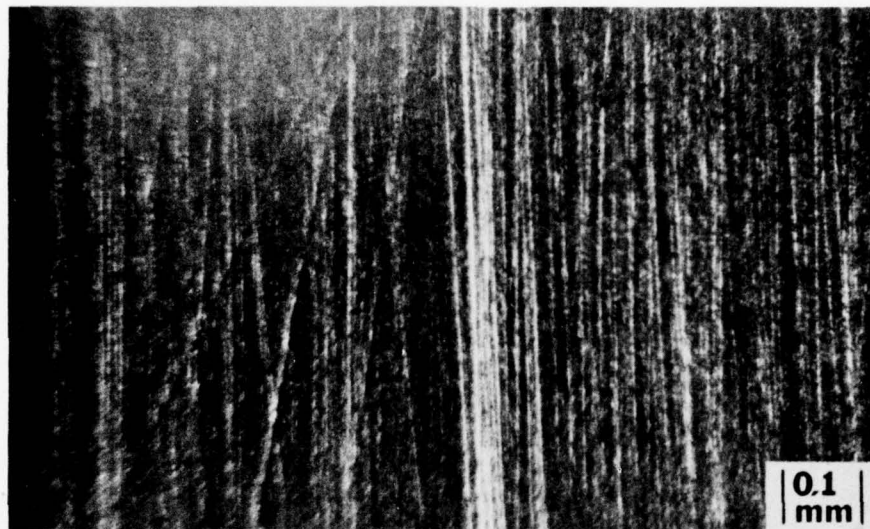


Figure 40 - Photomicrographs of Model Surfaces Before and After Cavitation Damage Testing

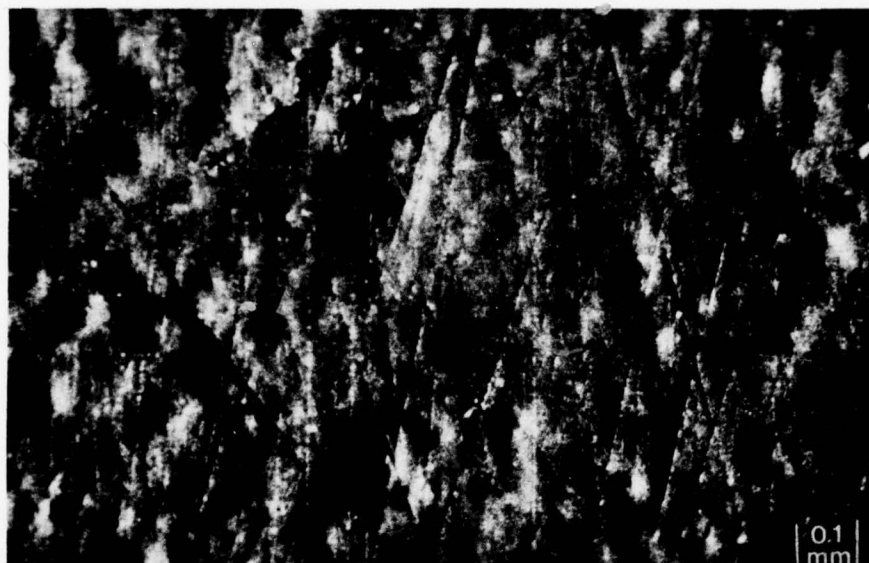


Figure 41 - Photomicrograph of the Approximate Pitting Density that Provides a Sufficient Sample for Analysis Without the Pits Overlapping

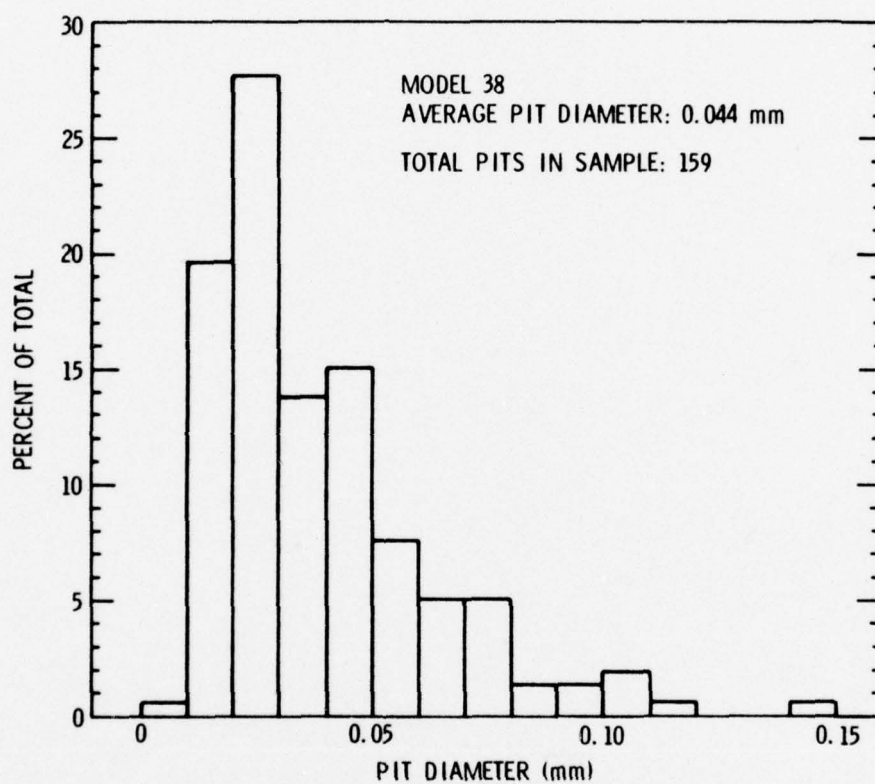


Figure 42 - Distribution of Pit Diameters for a Velocity of 30.1 m/sec and a Dimensionless Cavity Length of 3.0

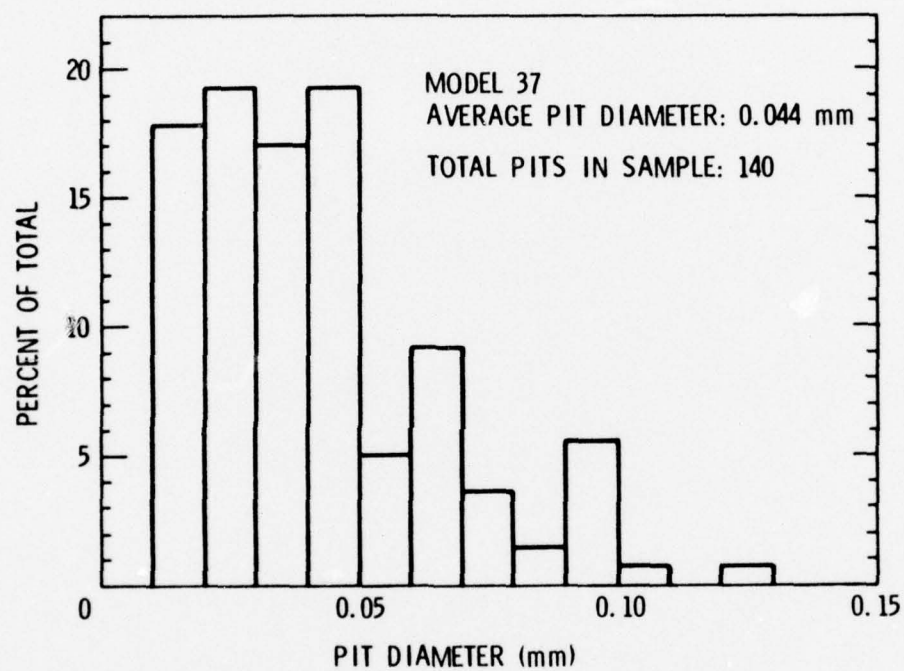


Figure 43 - Distribution of Pit Diameters for a Velocity of 38 m/sec and a Dimensionless Cavity Length of 3.0

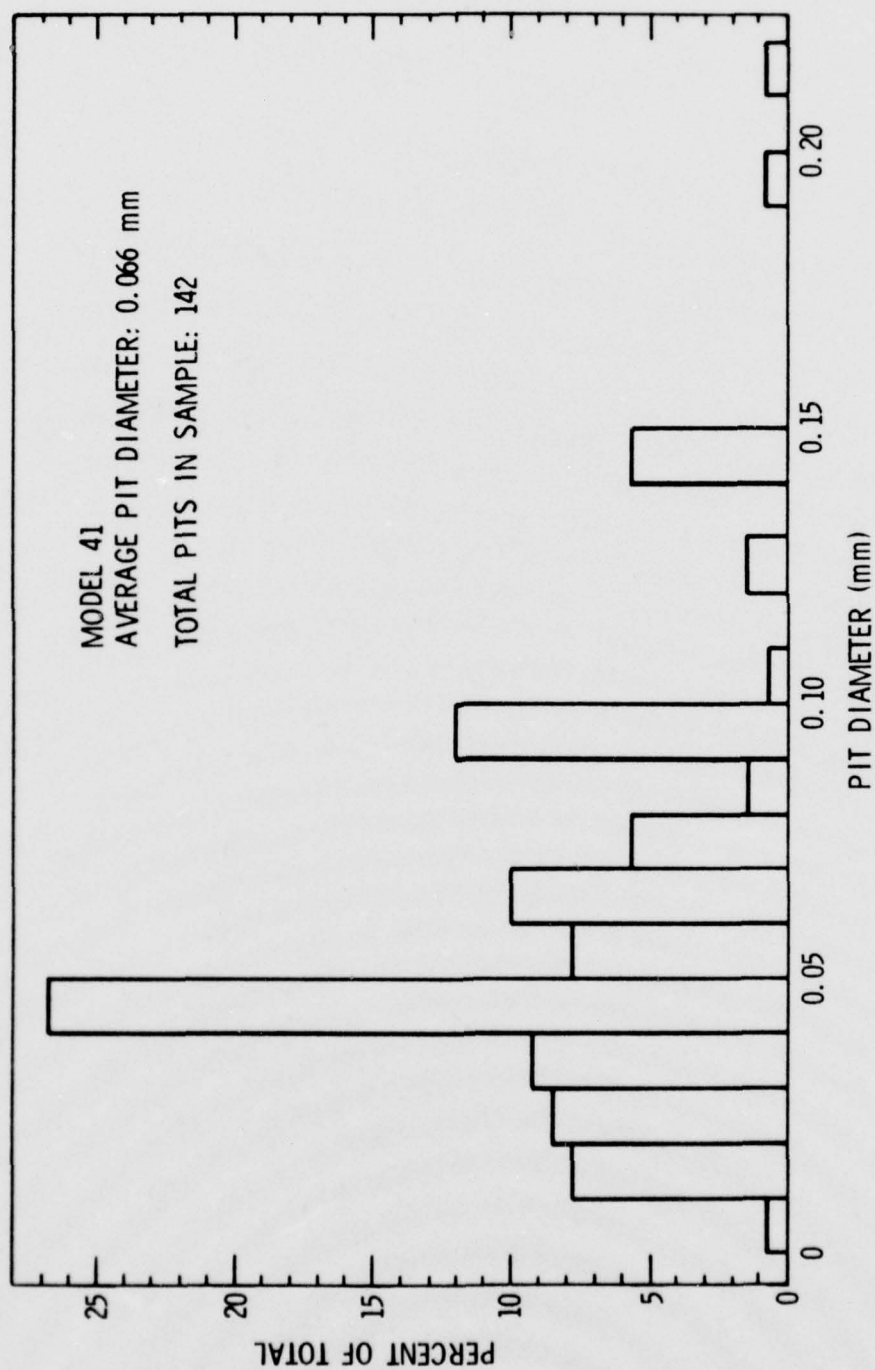


Figure 44 - Distribution of Pit Diameters for a Velocity of 49.3 m/sec and a Dimensionless Cavity Length of 3.0



Figure 45 - SEM Micrograph of a Deep Indentation Caused by Cavitation and the Machine Tool Marks Showing No Material Removal from the Surface (Model 46, $V_{\infty}=50$ m/sec, $L/D=4$, Air Content - 8.5 ppm)

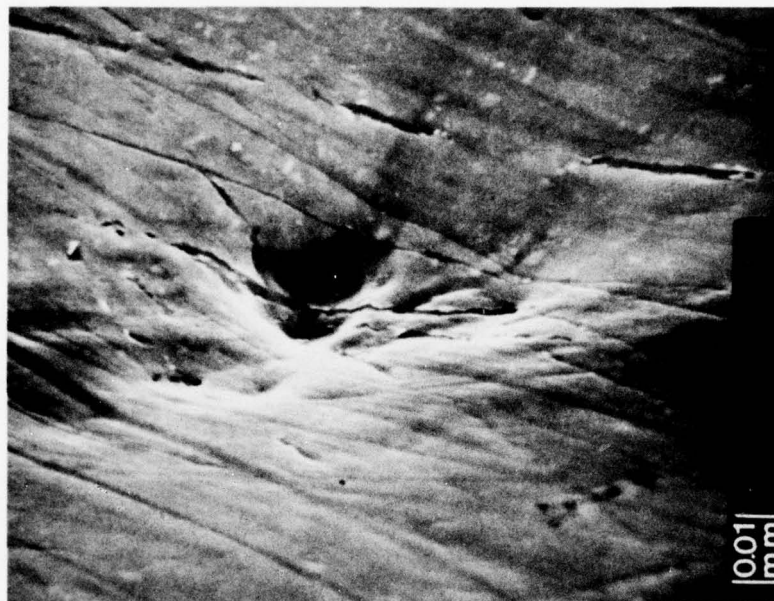


Figure 46 - SEM Micrographs of a Deep Cavitation Pit and Possible Strain Cracking at the Bottom of the Pit (Model 43, $V_{\infty}=43.4$ m/sec, $L/D=4$, Air Content - 9.84 ppm, and a 1.5-Minute Test Duration)



Figure 47 - Photograph of an Overall View of Spotting Corrosion of a Test Model (0.635 cm Diameter Zero-Caliber Ogive, Model 20, $V_{\infty}=23$ m/sec, $L/D=3$, Air Content - 20 ppm, and a 60-Minute Test Duration)

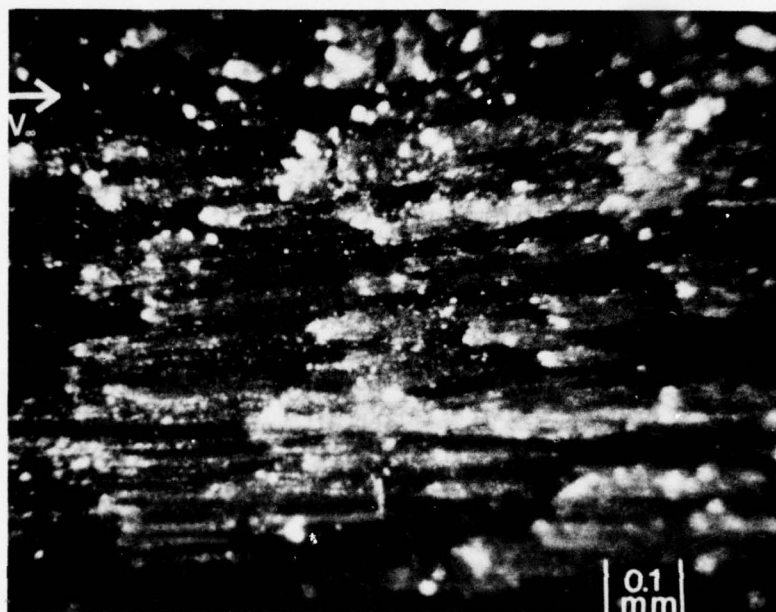


Figure 48 - Photomicrograph of Spotting Corrosion of a Test Model (Model 20, $V_{\infty}=23$ m/sec, $L/D=3$, Air Content - 20 ppm, and a 60-Minute Test Duration)

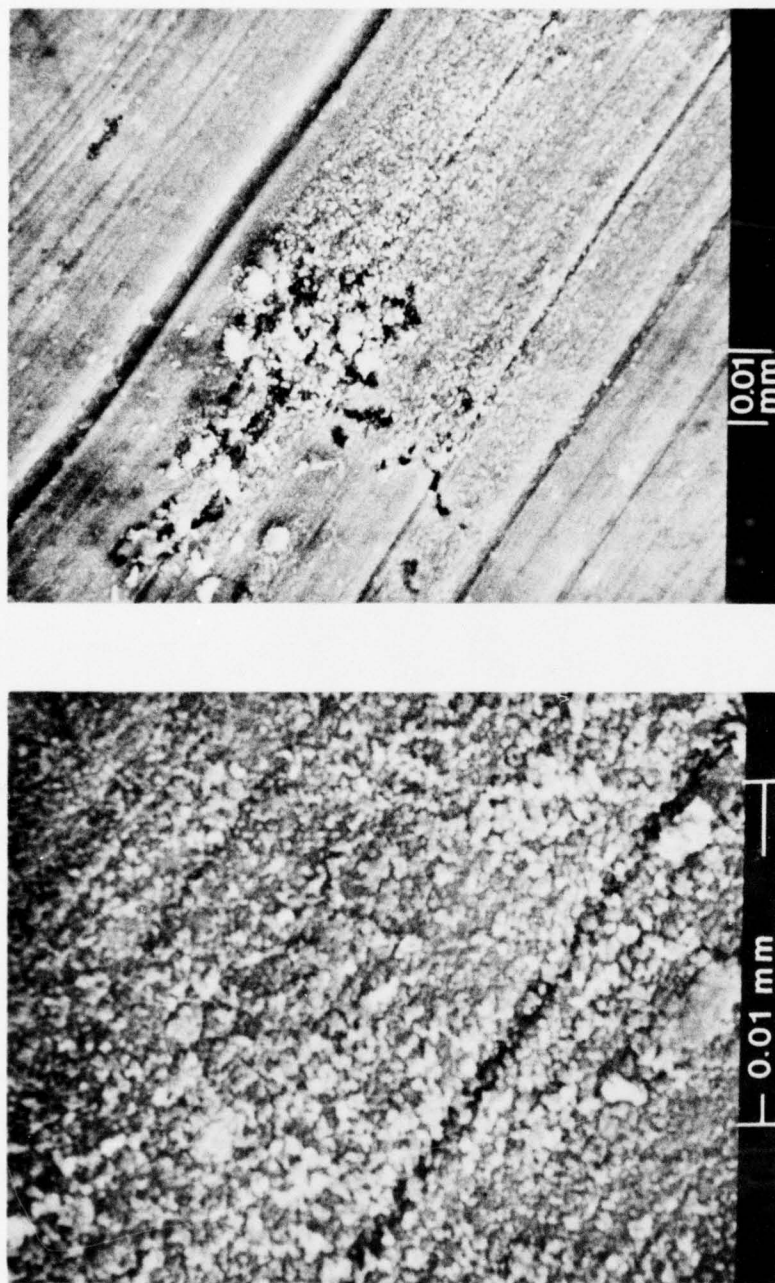


Figure 49 - SEM Micrographs of Spotting Corrosion Showing the Deep Irregular Shaped Pit and the Corrosion Products Cemented to the Model Surface (Model 20, $V_{\infty}=23$ m/sec, $L/D=3$, Air Content - 20 ppm, and a 60-Minute Test Duration)

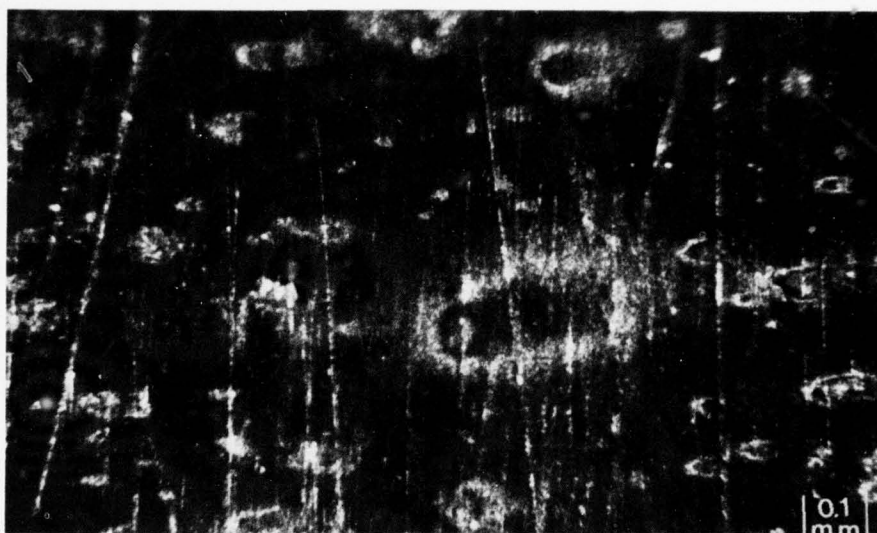


Figure 50 - Photomicrograph of Corrosion Pits Illuminated with Polarized Light (Model 45, $V_{\infty}=30.5$ m/sec, $L/D=4$, Air Content - 8.4 ppm, and a 20-Minute Test Duration)

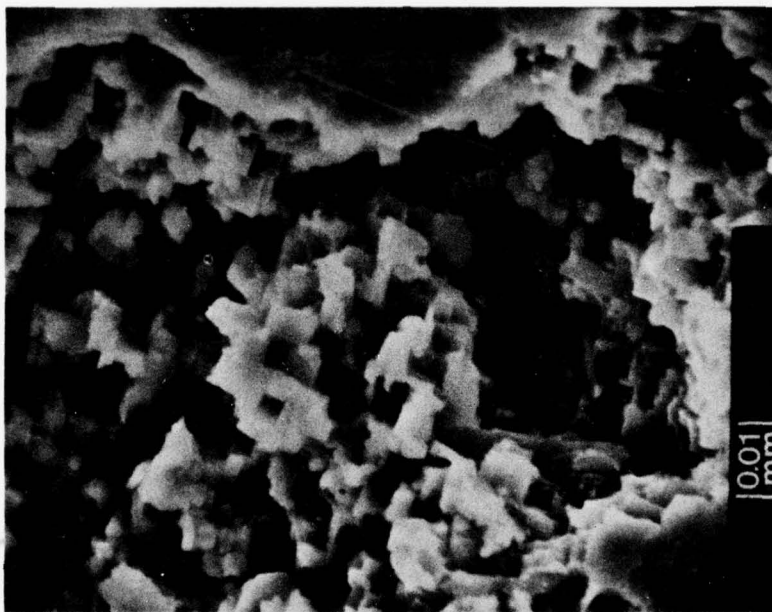


Figure 51 - SEM Micrograph of the Corrosion Attack Along the Cubic Structure of Aluminum (Model 37, $V_{\infty}=38$ m/sec, $L/D=3$, Air Content - 9.5 ppm and a 6-Minute Test Duration

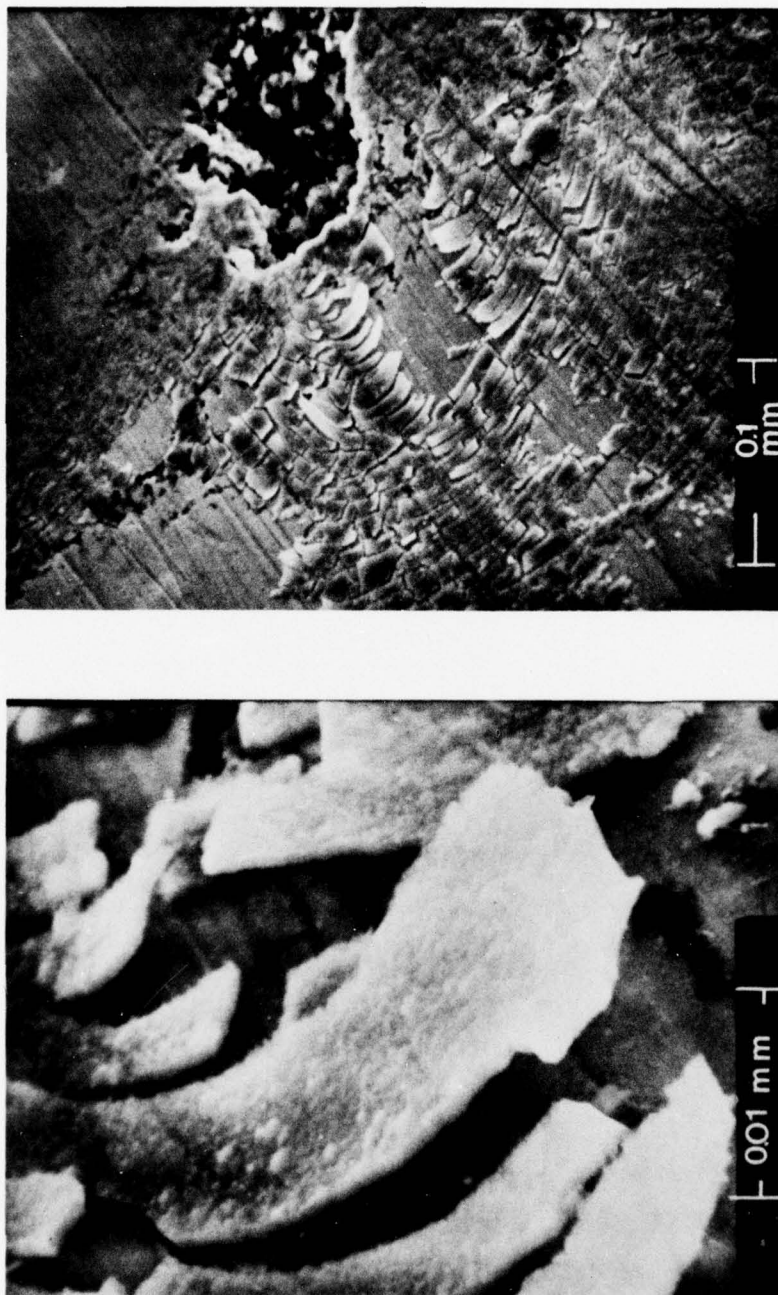


Figure 52 - SEM Micrographs of a Large Corrosion Pit and Detail of the Layer Deposited About the Pit (Model 34, $V_{\infty}=23$ m/sec, $L/D=2$, Air Content - 7.63 ppm, and a 30-Minute Test Duration)

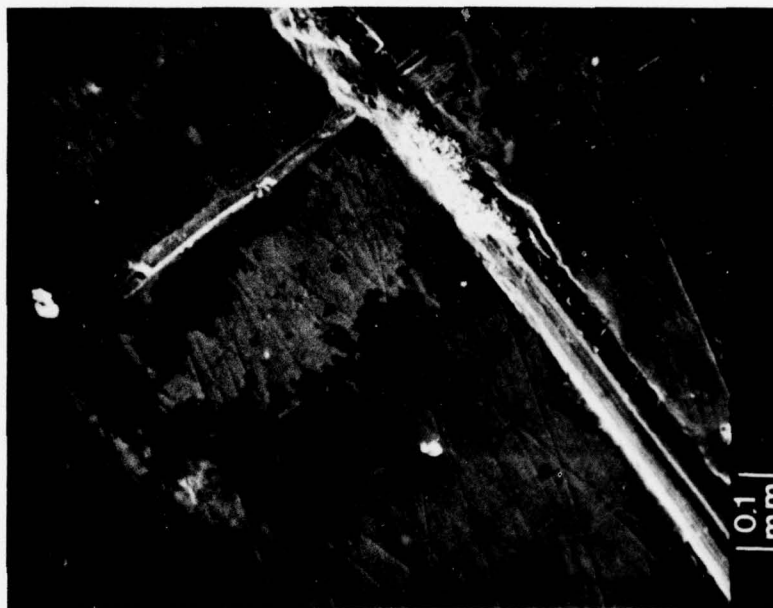


Figure 53 - SEM Micrograph of Corrosion Damage at the Cavity Reference Mark (Model 46, $V_{\infty}=50$ m/sec, $L/D=4$, Air Content - 8.5 ppm, and a 53-Second Test Duration)

- ▲ KNAPP (1955)
- SATO, ET AL. (1973)
- HACKWORTH AND ARNDT (1974)
- + THIS INVESTIGATION

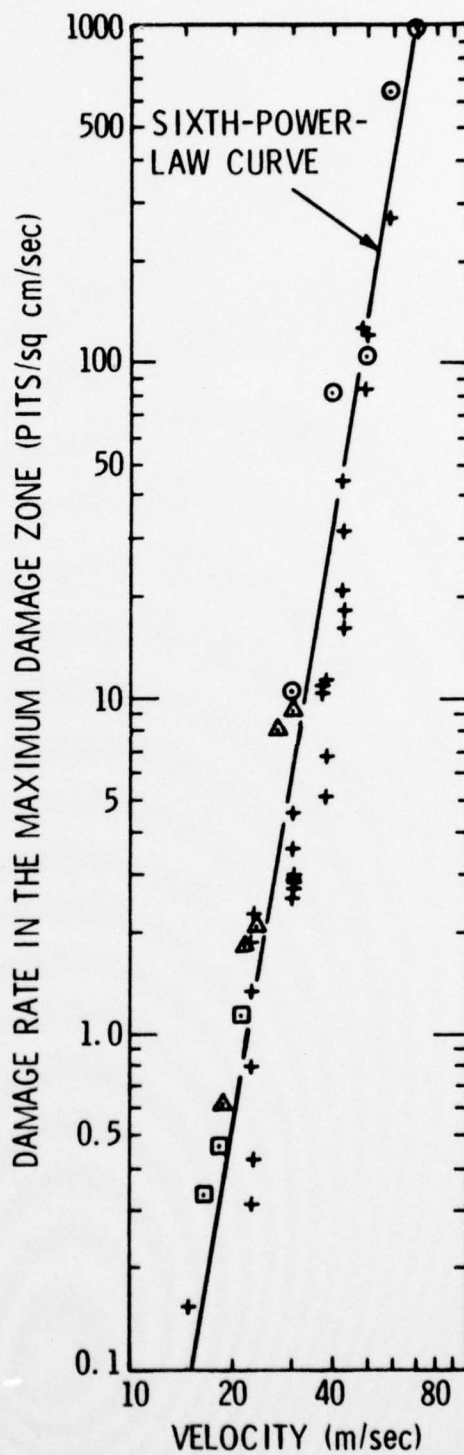


Figure 54 - Damage Rate in the Maximum Damage Zone Versus Velocity for Investigations of Cavitation Damage in Which There is No Weight Loss

- △ KNAPP (1955)
- SATO, ET AL. (1973)
(AIR CONTENT: 8.9 ppm)
- HACKWORTH AND
ARNDT (1974)
(AIR CONTENT: 8.0 ppm)
- + THIS INVESTIGATION
(AIR CONTENT: 8-20 ppm)

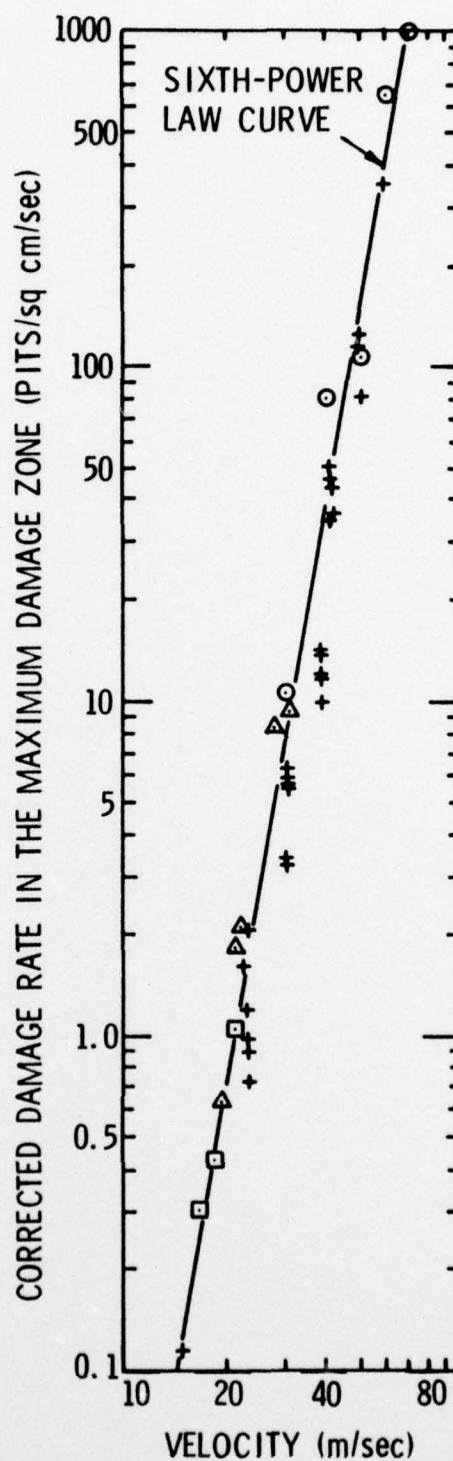


Figure 55 - Damage Rate in the Maximum Damage Zone Versus Velocity for Investigations of Cavitation Damage in Which There is No Weight Loss - Corrected for Air Content

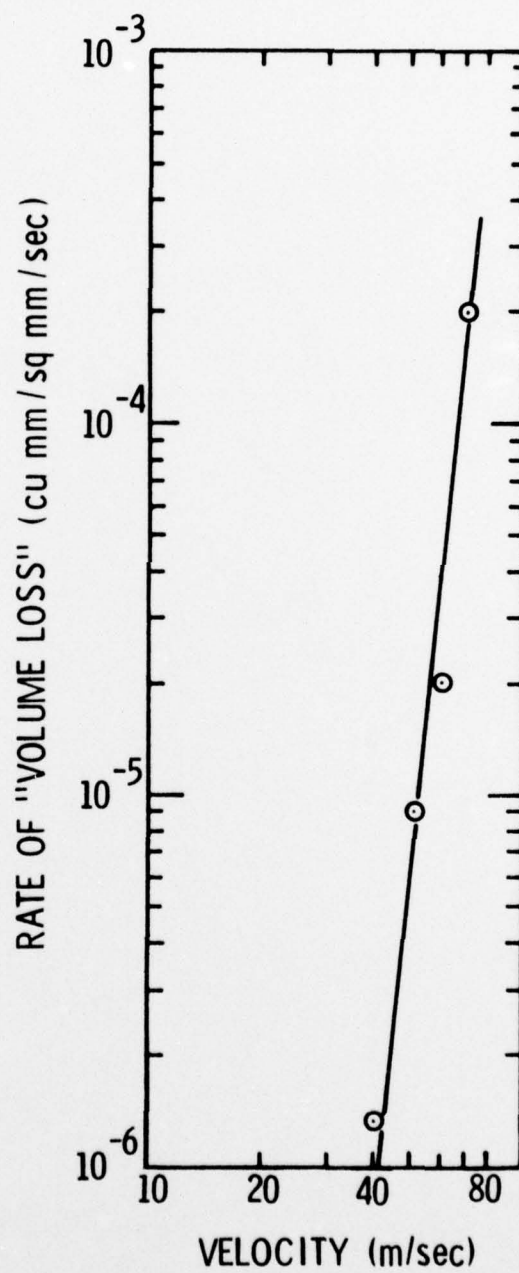


Figure 56 - Rate of "Volume Loss" per Unit Area Versus Velocity (Sato et al., 1973)

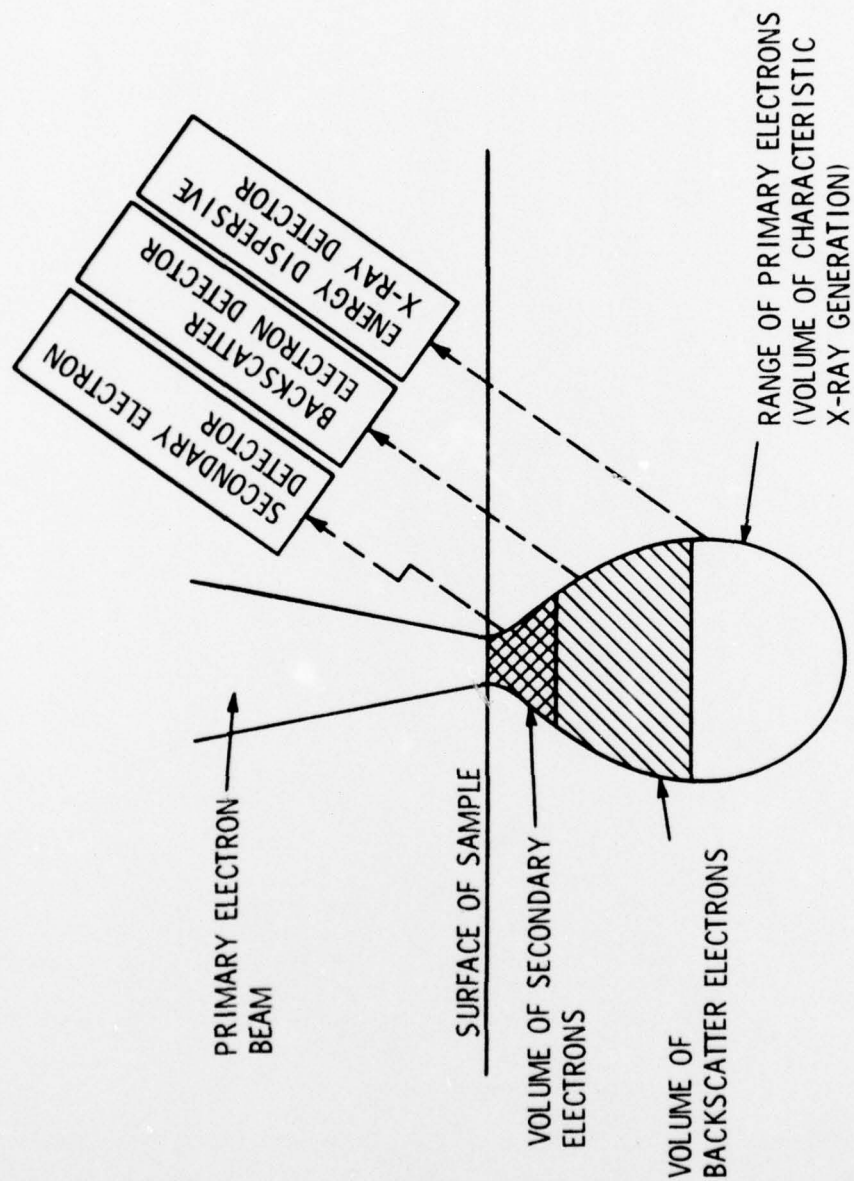
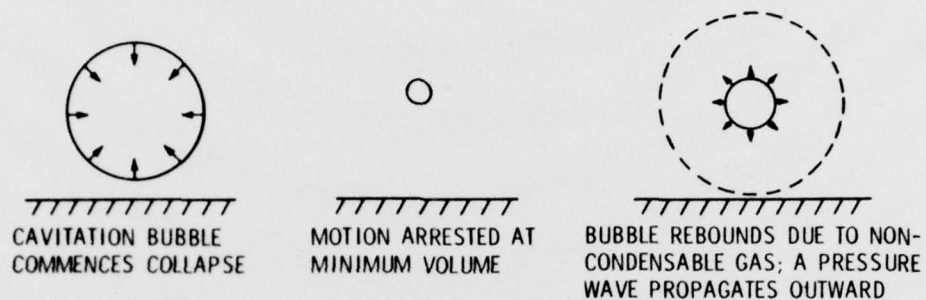
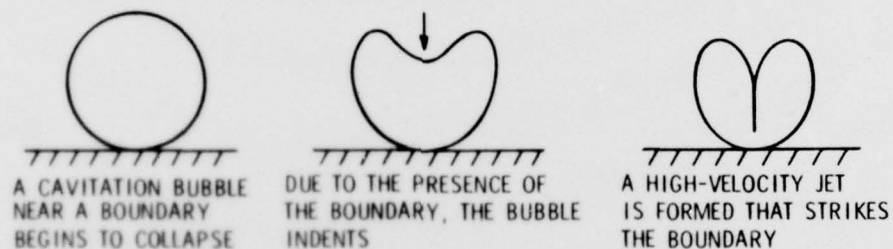


Figure 57 - Schematic Diagram of Imaging Mechanisms of the Scanning Electron Microscope

1. SPHERICAL COLLAPSE AND REBOUND - HICKLING AND PLESSET (1964)



2. NONSYMMETRICAL COLLAPSE - NAUDE AND ELLIS (1961)



3. FINAL TOROIDAL COLLAPSE - SHUTLER AND MESLER (1964)

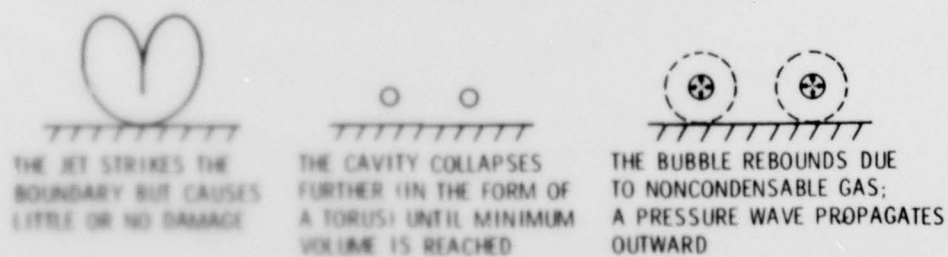
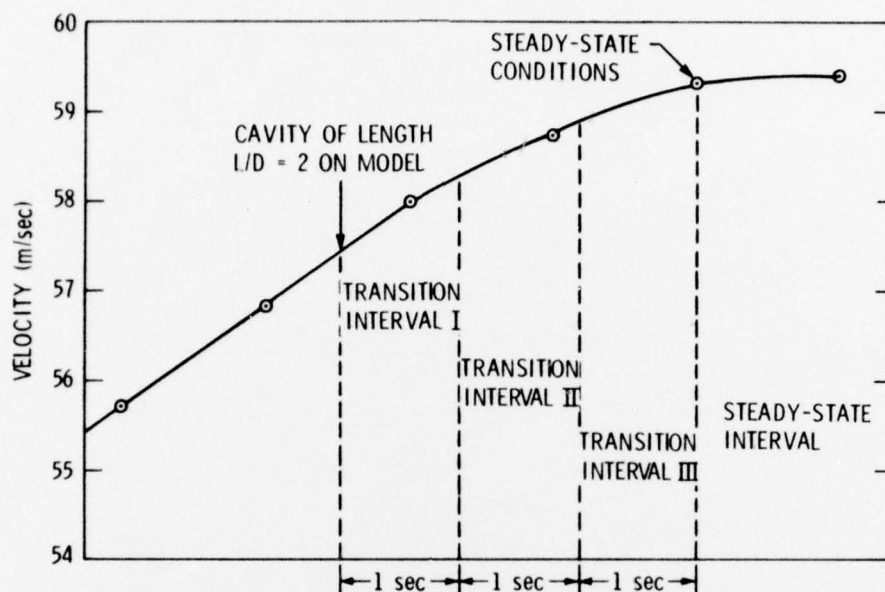


Figure 58 - Proposed Mechanical Mechanisms of Damage



CORRECTION OF THE PITTING DENSITY FOR A VELOCITY OF 59.3 m/sec AND L/D = 3 (MODEL 83)

INTERVAL	AVERAGE VELOCITY (m/sec)	ESTIMATED DAMAGE RATE (PITS/sq cm/sec)	LENGTH OF INTERVAL (sec)	PITTING DENSITY (PITS/sq cm)
I	57.9	240	1.0	240
II	58.55	257	1.0	257
III	59.1	270	1.0	270
STEADY STATE	59.3	280	5.0	1400
				TOTAL: 2167

$$\frac{\text{PITTING DENSITY FROM TRANSITION INTERVALS}}{\text{TOTAL PITTING DENSITY}} = \frac{767}{2167} = 0.354$$

35.4% OF THE PITS WERE FORMED IN THE TRANSITION PERIOD FOR THESE TEST CONDITIONS

Figure 59 - Tunnel Velocity as a Function of Time for the Velocity Transition Period - with Sample Calculations for the Correction of the Pitting Density for High Velocity Tests (59.3 m/sec Test)

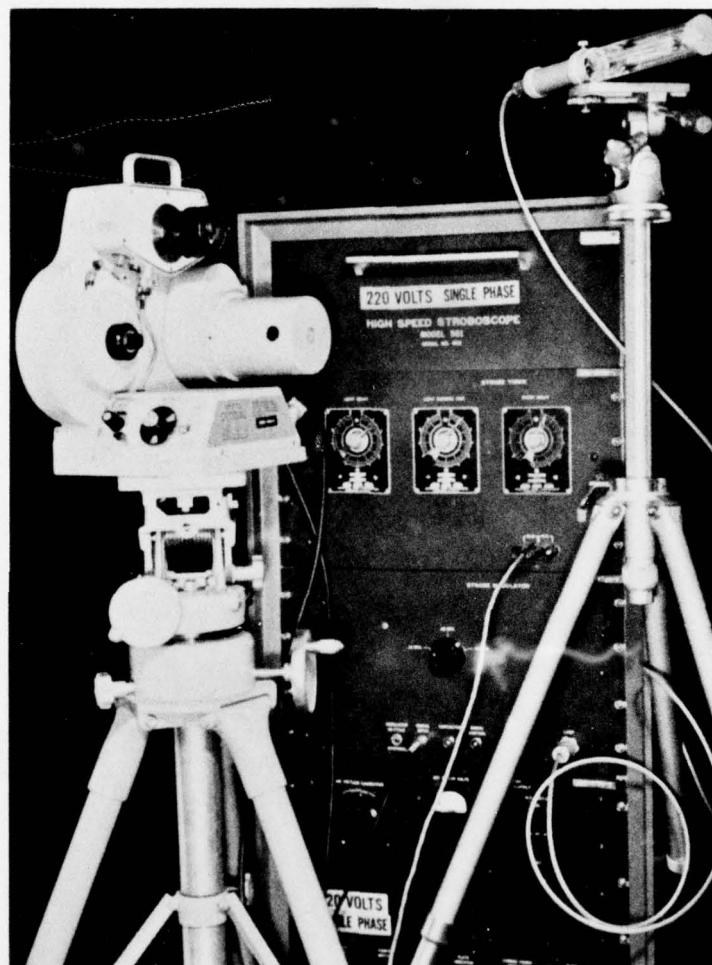


Figure 60 - Photograph of High Speed Photographic Apparatus - Redlake Hycam Camera and EG & G High Speed Strobe Unit (Circular Reflector Shown)

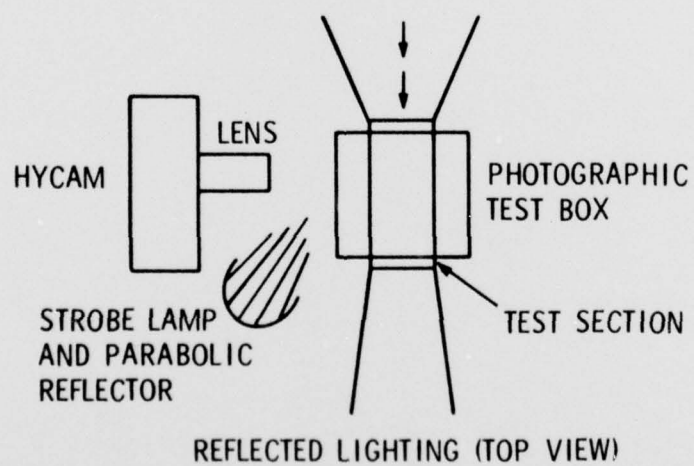
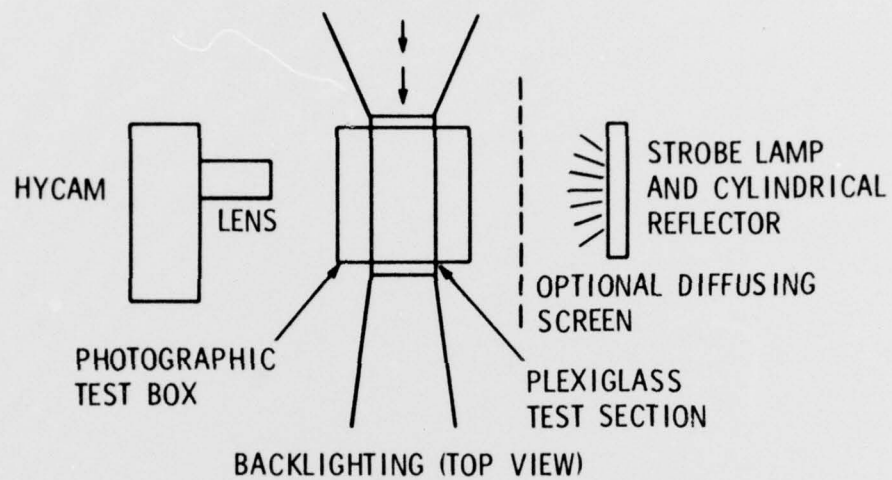


Figure 61 - Schematic Arrangement of High Speed Photographic Apparatus

DISTRIBUTION LIST for ARL TM 76-51 by D. R. Stinebring (dated February 17, 1976)

Commander
Naval Sea Systems Command
Department of the Navy
Washington, DC 20362
Attn: Library
Code NSEA-09G32
(Copy Nos. 1 and 2)

Naval Sea Systems Command
Attn: Code NSEA-0342
(Copy Nos. 3 and 4)

Defense Documentation Center
5010 Duke Street
Cameron Street
Alexandria, VA 22314
(Copy Nos. 5 - 16)

Naval Sea Systems Command
Department of the Navy
Washington, DC 20362
Attn: T. E. Peirce
Code NSEA-0351
(Copy No. 17)

Naval Sea Systems Command
Attn: A. R. Paladino
Code NSEA-0372
(Copy No. 18)

Commanding Officer
Naval Underwater Systems Center
Newport, RI 02840
Attn: Library
Code LA15
(Copy No. 19)

Commanding Officer
Naval Ocean Systems Center
San Diego, CA 92152
Attn: Library
(Copy No. 20)

Naval Ocean Systems Center
Attn: J. W. Hoyt
Code 2501
(Copy No. 21)

Commander
Naval Surface Weapon Center
Silver Spring, MD 20910
Attn: Library
(Copy No. 22)

Naval Surface Weapon Center
Attn: J. L. Baldwin
Code WA-42
(Copy No. 23)

Commanding Officer & Director
David W. Taylor Naval Ship R&D Center
Department of the Navy
Bethesda, MD 20084
Attn: W. B. Morgan
Code 154
(Copy No. 24)

David W. Taylor Naval Ship R&D Center
Attn: Technical Information Lib.
Code 522.1
(Copy No. 25)

David W. Taylor Naval Ship R&D Center
Attn: J. McCarthy
Code 1552
(Copy No. 26)

David W. Taylor Naval Ship R&D Center
Attn: F. B. Peterson
Code 1550
(Copy No. 27)

David W. Taylor Naval Ship R&D Center
Attn: M. Sevik
Code 19
(Copy No. 28)

Dr. Vijay H. Arakeri
Department of Mechanical Engineering
Indian Institute of Bangalore Tech.
INDIA
(Copy No. 29)

Dr. Allan J. Acosta
Prof. of Mechanical Engineering
Div. of Engineering and Applied Science
California Institute of Technology
Pasadena, CA 91125
(Copy No. 30)

Dr. Milton S. Plesset
California Institute of Technology
311 Thomas Building
1201 East California
Pasadena, CA 91125
(Copy No. 31)

DISTRIBUTION LIST for ARL TM 76-51 by D. R. Stinebring (dated February 17, 1977) (con't)

Dr. Christopher Brennen
Professor Division of Engineering
and Applied Physics
California Institute of Technology
Pasadena, CA 91125
(Copy No. 32)

Dr. T. Y. Wu
Division of Engineering
California Institute of Technology
Pasadena, CA 91109
(Copy No. 33)

Mr. Werner R. Britsch
Lewis Research Center
National Research Center
National Aeronautics and
Space Administration
Mail Stop 5-9
21000 Brookpark Road
Cleveland, OH 44135
(Copy No. 34)

Hydronautics, Inc.
Pindell School Road
Laurel, MD 20810
Attn: Library
(Copy No. 35)

Mr. L. Gross
R-P and VE
Marshall Space Flight Center
Huntsville, Alabama 35812
(Copy No. 36)

Mr. A. F. Lehman
P. O. Box 27
Centerport, N.Y. 11721
(Copy No. 37)

Mr. Robert Waid
Lockheed Missile & Space Company
Orgn. 57-24, Bldg. 150
Post Office Box 504
Sunnyvale, CA 94088
(Copy No. 38)

Dr. J. William Holl
The Pennsylvania State University
APPLIED RESEARCH LABORATORY
Post Office Box 30
State College, PA 16801
(Copy No. 39 - 44)

Mr. Michael L. Gillet
The Pennsylvania State University
APPLIED RESEARCH LABORATORY
(Copy No. 45)

Mr. D. R. Stinebring
The Pennsylvania State University
APPLIED RESEARCH LABORATORY
(Copy No. 46 - 50)

Mr. J. A. Carroll
The Pennsylvania State University
APPLIED RESEARCH LABORATORY
(Copy No. 51)

Dr. R. E. Henderson
The Pennsylvania State University
APPLIED RESEARCH LABORATORY
(Copy No. 52)

Mr. A. L. Treaster
The Pennsylvania State University
APPLIED RESEARCH LABORATORY
(Copy No. 53)

Garfield Thomas Water Tunnel Library
The Pennsylvania State University
APPLIED RESEARCH LABORATORY
(Copy No. 54)

Dr. Albert T. Ellis
University of California
Department of Applied Mechanics
La Jolla, CA 92038
(Copy No. 55)

Dr. F. G. Hammitt
Professor of Mechanical Engineering
The University of Michigan
Ann Arbor, Michigan 48105
(Copy No. 56)

Iowa Institute of Hydraulic Research
State University of Iowa
Iowa City, Iowa 52240
Attn: Director
(Copy No. 57)

DISTRIBUTION LIST for ARL TM 76-51 by D. R. Stinebring (dated February 17, 1977) (con't)

Prof. Edward Silberman
St. Anthony Falls Hydraulic Laboratory
Institute of Technology
University of Minnesota
Mississippi River at 3rd Avenue, S.E.
Minneapolis, Minnesota 55414
(Copy No. 58)

Dr. John F. Ripken
St. Anthony Falls Hydraulic Laboratory
University of Minnesota
Mississippi River at 3rd Avenue, S.E.
Minneapolis, Minnesota 55414
(Copy No. 59)

Dr. J. M. Robertson
125 Talbot Laboratory
University of Illinois
Urbana, Illinois 61801
(Copy No. 60)

Dr. A. Thiruvengadam
Mechanical Engineering Department
The Catholic University of America
Washington, DC 20017
(Copy No. 61)

Dr. D. R. F. Harleman
Hydrodynamics Laboratory
Massachusetts Institute of Technology
Cambridge, Massachusetts 02139
(Copy No. 62)

Dr. P. Leehey
Department of Naval Architecture
Massachusetts Institute of Technology
Cambridge, Massachusetts 02139
(Copy No. 63)

Dr. C. D. Lovstad
The Norwegian Ship Model
Experiment Tank
Trondheim, Norway
(Copy No. 64)

Dr. Hans Lindgren
Statens Skeppsprovingsanstalt
Box 24001
Goteborg 24
Sweden
(Copy No. 65)

Dr. C. Johnsson
Statens Skeppsprovingsanstalt
Box 24001
Goteborg 24
Sweden
(Copy No. 66)

Dr. J. H. J. van der Meulen
Nederlandsch Scheepsbouwkundig
Proefstation
Haagsteeg 2
Post Box 28
Wageningen
Holland
(Copy No. 67)

Dr. I. S. Pearsall
Department of Scientific and
Industrial Research
National Engineering Laboratory
East Kilbride
Glasgow, Scotland
(Copy No. 68)

Dr. John W. English
National Physical Laboratory
Teddington, Middlesex
England
(Copy No. 69)

Dr. J. Foxwell
Admiralty Research Laboratory
Teddington, Middlesex
England
(Copy No. 70)

Prof. J. Bonnin
Electricite de France
Direction Des Etudes et Recherches
6 Quai Watier 78400 Chatou
France
(Copy No. 71)

Prof. J. C. W. Raabe
Direktor des Instituts fur Hydr.
Maschinen und Anlagen
Technischen Hochschule
Munchen
Arcisstrasse 21, 8 Munchen 2
Germany
(Copy No. 72)

DISTRIBUTION LIST for ARL TM 76-51 by D. R. Stinebring (dated February 17, 1977) (con't)

Institute of High Speed Mechanics
Tohoku University
Sendai
Japan
Attn: Library
(Copy No. 73)

Dr. Claus Kruppa
Institut fur Schiffstechnik
Technische Universitat Berlin
Salzufer 17-19
1 Berlin 10 (Charlottenburg)
West Germany
(Copy No. 74)

Prof. S. P. Hutton
Department of Mechanical Engineering
The University
Southampton, SO9, 5 NH
England
(Copy No. 75)

Mr. Jesse Hord
Cryogenic Engineering Laboratory
U. S. Department of Commerce
National Bureau of Standards
Boulder Laboratories
Boulder, Colorado
(Copy No. 76)

Mr. A. Vosper
Admiralty Experiment Works
Haslar Goaport Hants PO12 2AC
England
(Copy No. 77)

Mr. Max Aucher
Bassin D'Essais des Carenes
8 Boulevard Victor
Paris (15) France
(Copy No. 78)

Dr. A. P. Keller
Lehrstuhl fur Wasserbau und
Wasserwirtschaft
Versuchsanstalt fur Wasserbau
Technische Universitat Munchen
Oskar v. Miller-Institut
D 811 Obernach
Post Walchensee
West Germany
(Copy No. 79)

Oxford University
Oxford, England
Attn: Library
(Copy No. 80)

Cambridge University
Cambridge, England
Attn: Library
(Copy No. 81)

Rocketdyne Library
6633 Canoga Avenue
Canoga Park, CA 91303
(Copy No. 82)

Aerojet Library
Post Office Box 15847
Sacramento, CA 95813
(Copy No. 83)

Dr. Rothe
Department 596-115
Rocketdyne Division
North American Aviation
6633 Canoga Avenue
Canoga Park, CA 91303
(Copy No. 84)

Dr. Jackobsen
Rocketdyne Division
North American Aviation
6633 Canoga Avenue
Canoga Park, CA 91303
(Copy No. 85)

Dr. Robert Y. Ting
Code 6170
Naval Research Laboratory
Washington, DC 20375
(Copy No. 86)

Mr. Russell Slanover
Mechanical Engineering Department
State University of New York at
Stony Brook
Stony Brook, N.Y.
(Copy No. 87)

Prof. Walter S. Bradfield
Mechanical Engineering Department
State University of New York at
Stony Brook
Stony Brook, N.Y.
(Copy No. 88)

DISTRIBUTION LIST for ARL TM 76-51 by D. R. Stinebring (dated February 17, 1977) (con't)

Mr. Frank J. Heymann
A2S Technology Development
Westinghouse Electric Corp.
Lester Branch P.O. Box 9175
Philadelphia, PA 19113
(Copy No. 89)

Instifut für Hydroakustik
8012 Ottobrunn bei München
Waldparkstraße 41
Federal Republic of Germany
Attn: Director
(Copy No. 96)

Mr. F. Danel
Code V
Zirst-Chemin de Malacher
38240 Meylan, France
(Copy No. 90)

Dr. Roger E. A. Arndt
St. Anthony Falls Hydraulic Laboratory
Mississippi River at 3rd Avenue, S.E.
Minneapolis, Minnesota 55414
(Copy No. 97)

GD Mehta
Hydronautics, Inc.
Laurel, MD 20810
(Copy No. 91)

Mr. Takao Sasajima
Resistance and Propulsion
Research Laboratory
Nagasaki Tech. Inst.
Mitsubishi Heavy Ind., Ltd.
1-1 Akunoura-Machi
Nagasaki 950-91
Japan
(Copy No. 92)

Dr. Peter van Oosanen
Netherlands Ship Model Basin
Haagsteen 2
Post Box 28
Wageningen, Netherlands
(Copy No. 93)

Dr. Ralph Cooper
Office of Naval Research
Department of the Navy
800 N. Quincy Street
Arlington, VA 22217
(Copy No. 94)

Dr. Paul Cooper
Engineering Specialish
TRW Accessories Division
2448 Euclid Heights Blvd.
Cleveland, OH 44106
(Copy No. 95)

AD-A049 766

PENNSYLVANIA STATE UNIV UNIVERSITY PARK APPLIED RESE--ETC F/G 20/4
SCALING OF CAVITATION DAMAGE.(U)

FEB 76 D R STINEBRING

N00017-73-C-1418

UNCLASSIFIED

TM-76-51

NL

3 OF 3
ADA
049766

SUPPLEMENTARY

INFORMATION

END
DATE
FILMED

12-78

DDC

SUPPLEMENTARY

INFORMATION

AD-A049766

THE PENNSYLVANIA STATE UNIVERSITY
INSTITUTE FOR SCIENCE AND ENGINEERING
APPLIED RESEARCH LABORATORY

ADDRESS REPLY TO:
APPLIED RESEARCH LABORATORY
P. O. Box 30
STATE COLLEGE, PENNSYLVANIA 16801

16 May 1978

To: DISTRIBUTION LIST

Please replace the attached pages in your copy(ies) of ARL Technical Memorandum, TM 76-51, "Scaling of Cavitation Damage," by D. R. Stinebring. The date on the title page and the Form 1473 has been corrected and changed to 17 February 1976.

Very truly yours,

Blaine R. Parkin

Blaine R. Parkin
Director
Garfield Thomas Water Tunnel

BRP:mac

Attachments

UNCLASSIFIED

SCALING OF CAVITATION DAMAGE

Stinebring, D. R.

Technical Memorandum
File No. TM 76-51
17 February 1976
Contract No. N00017-73-C-1418

Copy No. 5

The Pennsylvania State University
APPLIED RESEARCH LABORATORY
Post Office Box 30
State College, PA 16801

Approved for Public Release
Unlimited Distribution

NAVY DEPARTMENT

NAVAL SEA SYSTEMS COMMAND

UNCLASSIFIED

UNCLASSIFIED

SECURITY CLASSIFICATION OF THIS PAGE (When Data Entered)

REPORT DOCUMENTATION PAGE		READ INSTRUCTIONS BEFORE COMPLETING FORM
1. REPORT NUMBER TM 76-51	2. GOVT ACCESSION NO.	3. RECIPIENT'S CATALOG NUMBER
4. TITLE (and Subtitle) Scaling of Cavitation Damage		5. TYPE OF REPORT & PERIOD COVERED Technical Memorandum
		6. PERFORMING ORG. REPORT NUMBER
7. AUTHOR(s) David R. Stinebring		8. CONTRACT OR GRANT NUMBER(s) N00017-73-C-1418
9. PERFORMING ORGANIZATION NAME AND ADDRESS Applied Research Laboratory P.O. Box 30 State College, PA 16801		10. PROGRAM ELEMENT, PROJECT, TASK AREA & WORK UNIT NUMBERS
11. CONTROLLING OFFICE NAME AND ADDRESS Naval Sea Systems Command Washington, DC 20362		12. REPORT DATE 17 February 1976
		13. NUMBER OF PAGES
14. MONITORING AGENCY NAME & ADDRESS (if different from Controlling Office)		15. SECURITY CLASS. (of this report) UNCLASSIFIED
		15a. DECLASSIFICATION/DOWNGRADING SCHEDULE
15. DISTRIBUTION STATEMENT (of this Report) Approved for public release. Distribution unlimited. Per NAVSEA - 24 March 1976		
17. DISTRIBUTION STATEMENT (of the abstract entered in Block 20, if different from Report)		
18. SUPPLEMENTARY NOTES Master of Science Thesis in Aerospace Engineering, August 1976.		
19. KEY WORDS (Continue on reverse side if necessary and identify by block number) cavitation, erosion, cavitation damage, corrosion		
20. ABSTRACT (Continue on reverse side if necessary and identify by block number) This investigation has focused on the initial stages of cavitation erosion using a ductile material in a flowing system employing water as the working fluid. The test models were 0.635 cm diameter zero-caliber ogives made of pure annealed aluminum. The aluminum was selected as a material which would be suitable for recording the intensity of cavitation bubble collapse. The damage in the initial stages was in the form of small indentations in the model surface. The greatest damage was within an area corresponding to the cavity closure point on the model. The pits were round depressions		

DD FORM 1 JAN 73 1473 EDITION OF 1 NOV 65 IS OBSOLETE

UNCLASSIFIED

SECURITY CLASSIFICATION OF THIS PAGE (When Data Entered)

UNCLASSIFIED

SECURITY CLASSIFICATION OF THIS PAGE(When Data Entered)

usually under 0.1 mm in diameter with the majority less than 0.05 mm across. During the formation of these pits, it appears that no material was removed from the surface. Using the pure annealed aluminum test probe, a sufficient damage sample could be generated in a relatively short period of time.

It was observed that the velocity had a marked effect upon the rate of damage production. For a range of velocities from 14.9 to 59.3 m/sec, the damage and pitting rates increased by approximately the sixth power of velocity. This result is in agreement with the observations of R. T. Knapp which were first reported in 1955. The velocity also affected the sizes of the individual damage pits. The average volume of the pits increased by the fifth power of velocity. Since the volume of each pit is a measure of the energy required to form the pit, the average collapse energy absorbed increases by the fifth power of velocity. A relationship between the pit volume and the absorbed collapse energy was obtained by performing a dynamic hardness test on the model material. If the pitting rate increases by the sixth power of velocity, and the average collapse energy absorbed per pit increases by the fifth power, then the rate of total damage energy absorbed by the model increases by the eleventh power. A plot of the distribution of absorbed collapse energies was also generated for three flow conditions.

It was observed that the cavity length and air content also affected the damage rates. There was almost no damage to the models for very short cavity lengths. The damage rate increased with cavity length, reached a peak, and then slowly decreased for longer cavities. This tendency has been observed by other investigators. For a doubling of the air content from 10 to 20 ppm, the rate of damage production was reduced by nearly fifty percent.

From high-speed movies of the cavity behavior, it was observed that the cavity regularly breaks off from the model surface. This is due to a reentrant jet moving through the cavity and striking the cavity leading edge. On many of the models, pitting was observed near the leading edge. It is felt that this could be a result of the reentrant jet behavior. When the jet strikes the cavity wall, it creates a short-term pressure rise, causing local cavitation bubbles to collapse. If the collapsing bubbles are near the model surface, damage to the model could occur.

The effect of cavitation upon the rate of corrosion of aluminum was not fully explored. General observations showed a strong relationship between the cavitation and corrosion, with cavitation tending to increase the corrosion rate. For observations of the corrosion damage and cavitation pitting, the scanning electron microscope proved to be a most useful tool. Clear views of the damage were obtained with the large depth of field possible at high magnifications.

In general, the results of this investigation compared favorably with the results of other investigations. The sixth power damage rate law and the actual damage rates involved showed good agreement with three other investigations. The interesting feature of this comparison is the fact that even though the size and shape of the models used in each of the four investigations were significantly different, the observed damage rates were approximately equal at the same velocity.

UNCLASSIFIED

SECURITY CLASSIFICATION OF THIS PAGE(When Data Entered)